SUBMITTED BY HARRY GREEN, TO THE UNIVERSITY OF
EXETER AS A THESIS FOR THE DEGREE OF DOCTOR OF
PHILOSOPHY IN MATHEMATICS

Mathematical Modelling of Cardiac Rhythms in Health and Disease

Author:

Harry David GREEN

Supervisor:

Prof. John TERRY

Second supervisor:

Dr. Ozgur AKMAN

I certify that all material in this thesis which is not my own work has been identified and that no material has previously been submitted and approved for the award of a degree by this or any other University.

Signature: *H. Green*

Submitted September 2017

Abstract

Cardiac disease is the most common cause of death among the adult population worldwide and atrial fibrillation (AF) is the most common cardiac arrhythmia. The state of the art in AF treatment involves creating lesions of heart tissue through radiofrequency ablation. In this thesis, mathematical modelling techniques are developed to design decision support tools that could help a cardiologist determine the best location to ablate in clinic. Firstly, parameter optimisation methods are explored to adapt a model designed for the ventricles to the atria, and a novel technique is introduced to characterise pathways through parameter space from a healthy state to a diseased state using a multi-objective genetic algorithm. Next, I reproduce clinical signals recorded during AF ablation through the use of a phenomenological model of the cardiac action potential on a cylinder and show how this model can enable us to recover information lost in clinic to improve clinical decision. This is followed by introducing a more simplistic approach to the same problem, by characterising the electrical activity on the recording by a sine wave. Finally, the effectiveness of these two approaches is compared in the clinical setting by testing both as decision support tools. The emphasis of the approaches throughout the thesis is on developing techniques with clinical applicability. We demonstrate that lost information in clinic can affect the decision made by an experienced clinician, and that the mathematical modelling approaches developed in the thesis can significantly reduce the impact that this information loss can have on clinical decision making.

Acknowledgements

Firstly, I'd like to express my thanks to my supervisor, John Terry, for the continuous support throughout the PhD, for the technical advice, for keeping my direction clinically focused, for proof reading, and for tenacity in dealing with reviewers and editors. Working with John has been insightful, inspirational and influential, and has directed my research interests towards a translational focus while supporting my interest in teaching. I'd also like to thank my second supervisor, Ozgur Akman, for valuable support with parameter optimisation techniques and numerical methods.

This research would not have been possible without the collaborators on the project, most notably Glyn Thomas from Bristol Heart Institute, for data collection and insight. From many trips to the operating theatre and observing atrial ablation being performed I learned a great deal about cardiac arrhythmia and the challenges faced in clinic. Additionally, I'd like to thank Remi Dubois and Yves Coudiere of the University Hospital of Bordeaux for data, insightful discussions regarding modelling and support with using clinical software.

I'd also like to thank Lauric Ferrat for valuable advice on statistical techniques throughout the project, Victoria Hammond for help with commercialisation ventures, and Marc Goodfellow, Vadim Biktashev and Jan Sieber for discussions about the research. I've also benefited greatly from the teaching experience I've obtained during the PhD, and would like to thank Barrie Cooper for supporting my work as a teaching consultant.

Author's Declarations

I declare that the work in this thesis was carried out in accordance with the requirements of the University's Regulations and Code of Practice for Research Degree Programmes and that it has not been submitted for any other academic award. Except where indicated by specific reference in the text, the work is the candidates own work. Work done in collaboration with, or with the assistance of, others, is indicated as such (summarised in a footnote on the first page of every chapter). Any views expressed in the thesis are those of the author.

Contents

List of Acronyms

AP - Action Potential

APD - Action Potential Duration

AF - Atrial Fibrillation

AT - Atrial Tachycardia

AVRNT - Atrioventricular Nodal Re-entrant Tachycardia

AVN - Atrioventricular Node

BCL - Basic Cycle Length

BOCF - Bueno-Orovio Cherry Fenton

BPM - Beats per Minute

CPVI - Circumferential Pulmonary Vein Isolation

CFAE - Complex Fractionated Atrial Electrogram

CV - Conduction Velocity

DI - Diastolic Interval

ECG - Electrocardiogram

GA - Genetic Algorithm

NLEO - Nonlinear Energy Operator

NMSS - Nelder-Mead Simplex Search

NSGA-II - Non-dominated Sorting Genetic Algorithm II

ODE - Ordinary Differential Equation

PDE - Partial Differential Equation

PSO - Particle Swarm Optimisation

PV - Pulmonary Vein

PVI - Pulmonary Vein Isolation

RFA - RadioFrequency Ablation

RMS - Root Mean Squared

SAN - Sinoatrial Node

TNNP - Ten Tusscher-Noble-Noble Panfilov

VT - Ventricular Tachycardia

List of Tables

List of Figures

Chapter 1

Introduction

1.1 Thesis Aims

In this thesis I focus on the development and application of mathematical modelling techniques towards real-time decision support tools for guiding cardiologists treating cardiac conditions. This chapter introduces the basic theory of how the cardiac conduction system functions in health and disease, then briefly addresses why mathematical models can be useful in the study of heart disease and development of associated tools. The literature review in chapter 2 will expand on this background theory in more detail. The chapter concludes with an outline of the thesis.

1.2 Introduction to Theory of Cardiac Conduction and Modelling

1.2.1 Electrical Conduction in Normal Heart Rhythm

The human heart consists of four chambers: the atria, responsible for collecting blood from the lungs (left atrium) and rest of the body (right atrium), and the ventricles, responsible for pumping blood to the lungs (right ventricle) and the rest of the body (left ventricle). This pumping action is performed by a sharp but coordinated contraction of the cardiac muscle cells. A weak or uncoordinated contraction pattern in the heart muscle will cause a reduced cardiac output. The coordination and power of the contraction is regulated by an electrical signal in the form of a travelling electrical pulse called an action potential (AP).

The electrocardiogram (ECG) is an aggregation of activity of single cells, used in

clinic to record the electrical activity of the heart. The ECG can be recorded from the skin (body surface ECG), which will record activity across entire heart, primarily used for diagnosis and monitoring of overall heart rate. Intracardiac ECGs are recorded from inside the heart, and record activity across a small patch of heart tissue, used for determination of the optimal location to apply treatment.

In terms of electrophysiology, cardiac cells can largely be categorised into two groups: cardiac pacemaker cells and cardiomyocytes (non-pacemaker cells). Healthy pacemaker cells are able to fire action potentials autonomously at a regular rate, although this rate can be driven by the intracellular Voltage fluctuations of neighbouring cells. Non-pacemaker cells will maintain a constant resting potential until neighbouring cells fire an AP. The electrical conductivity of the cardiac tissue allows this action potential to propagate from one non-pacemaker cell to the next.

The main electrical conductance pathway in the heart begins in a node of pacemaker cells called the sinoatrial node (SAN), located high in the right atrium. The SAN is the most important part of the heart for maintaining a regular heartbeat at between 60 and 100 beats per minute (BPM), although this can be influenced by external factors such as the need for quicker blood flow during exercise, and internal factors such as disease.

The AP from the SAN spreads out over the tissue of the atrial myocardium, causing it to contract. This process generates the P Wave on the body surface ECG (see Figure 1.1). The myocardial tissue is made up of non-pacemaker cells, and under normal circumstances will not contract without a signal from the SAN. The atrial contraction passes collected blood from the atria into the ventricles. The right atrium will pump deoxygenated blood, collected from across the body, into the right ventricle, while the left atrium pumps oxygenated blood from the lungs, collected through the pulmonary veins, into the left ventricle. Blood flow is illustrated in panel a of Figure 1.2.

The travelling excitation wave then passes through the second node of pacemaker cells, the atrioventricular node (AVN). The AVN will naturally pulse at a frequency of 40 BPM but will phase lock to the rate of the atria under normal conditions [1, 2]. The purpose of the AVN is to delay the propagation of the action potential, allowing the ventricles to fill up with blood from the atria, and to regulate electrical signal down towards them, as in a healthy, anatomically normal heart, the AVN is the only electrically conductive pathway from the atria to the ventricles. Electrical flow is illustrated in panel b of Figure 1.2.
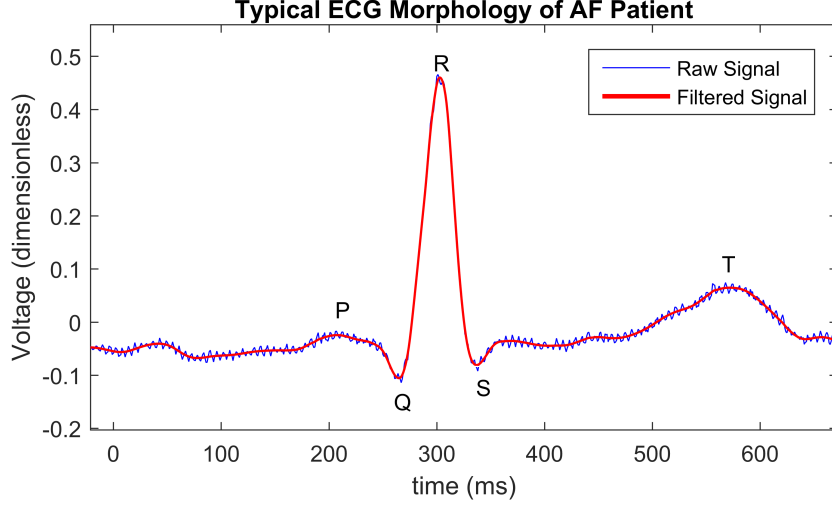
Figure 1.1: **Typical ECG Morphology of AF Patient.** A body surface ECG recording from an Atrial Fibrillation patient at Bristol Heart Institute with annotations showing the P wave (contraction of the atrium) QRS complex (contraction of the ventricles) and T wave (recovery of ventricles). The main difference between this morphology and that of a healthy patient is the lack of a well-defined P wave.

From the AVN, the wave travels along fibres called the His bundle that eventually split into the left and right bundle branches. From there, the wave spreads across the surface of the ventricles via the Purkinje fibres. The contraction of the ventricles is stronger than that of the atria, and this process causes the highest amplitude spike on a typical ECG signal (the QRS complex). The contraction of the left ventricle pumps the deoxygenated blood to the lungs for reoxygenation, while the right ventricle pumps oxygenated blood around the body. The recovery of the ventricles causes the T wave. The recovery of the atria is not visible on the ECG as it is obscured by the larger amplitude QRS complex. Figure 1.1 displays an ECG recording from a patient with the PQRST morphologies annotated. The signal is filtered with a wavelet denoising algorithm to filter out the residual noise in the signal.

1.2.2 Electrophysiology of Cardiomyocytes

The AP that propagates across the atrial and ventricular tissue is a short (roughly 200-300ms [3]) travelling pulse, generated by ion channels maintaining a current by the regulation of the flow of calcium (Ca), potassium (K) and sodium (Na) in and out of the cell [4]. The cardiac AP is commonly defined in 5 key phases [5], beginning with phase 4. These are typically defined with phase 4 first, as phase 4 both begins and ends the AP, as shown on in Figure 1.3.

(a) Blood Flow in the Heart   (b) Electrical Flow on the Heart
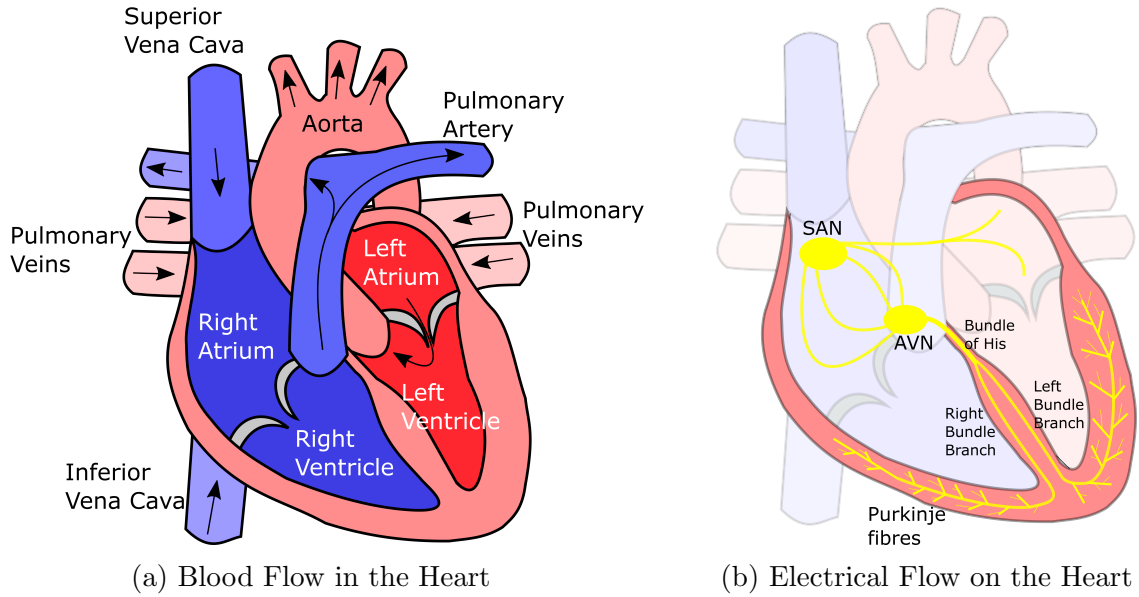
Figure 1.2: **Blood and Electrical Flow in the Heart.** (a) Diagram showing blood flow through the four heart chambers. Arrows represent direction of flow. Blue regions contain de-oxygenated blood, which flows in through the vena cava and out through the pulmonary artery to the lungs and red regions contain oxygenated blood, which flow in from the lungs via the pulmonary veins and out through the aorta. (b) Diagram showing electrical flow along the cardiac muscle fibres. The electrical signal travels from the Sinoatrial Node (SAN) across the atria, causing a contraction, pumping blood into the ventricles. The signal is delayed as it travels through the Atrioventricular Node (AVN) before propagating on to the ventricles, pumping blood to the lungs and rest of the body.

Phase 4 is the resting potential, typically between -80 and -90 mV for both atrial and ventricular cardiomyocytes [6], caused by the ionic concentration differential across the membrane, mostly inwards flowing K^+ ions via the I_{K1} channel. Once the cell is given an electrical stimulus, either externally during experiment, directly from the SAN, or from a neighbouring cardiomyocyte, phase 0 is activated: a sharp depolarisation during which the intracellular potential rapidly increases to between 20 and 50 mV (depending on cell type and location) by the activation of a rapid inwards Na^+ current (I_{Na}). The maximum gradient reached during phase 0 is called the upstroke velocity. However, if the stimulus does not bring the membrane Voltage above a firing threshold, the cell will not fire an AP.

Following the peak, the Voltage slightly declines in phase 1, before the longest active phase of the AP, the plateau phase (phase 2), where a high Voltage is maintained by a balance of inwards flowing Ca^{2+} (I_{Ca-L}) and outwards flowing K^+ (I_{KS}) currents. Phase 3 slowly causes the I_{Ca-L} to close and an additional outwards K^+ channel (I_{KR}) to open, causing a repolarisation of the cell and a return to the resting potential (phase 4). All 5
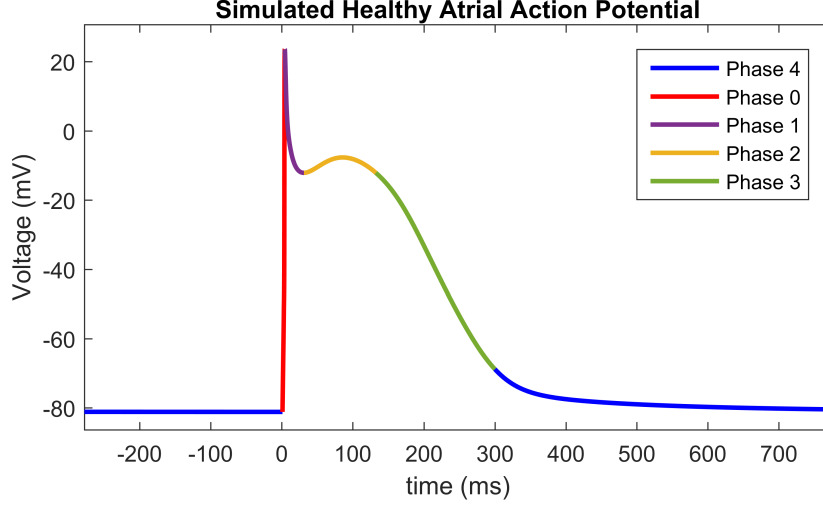
Figure 1.3: **Simulated Healthy Action Potential.** A healthy atrial action potential showing the four main phases into which the action potential is typically characterised. Action potential is simulated from the Courtemanche model, a biologically detailed mathematical model [4].

phases of a healthy human atrial AP, simulated by a mathematical model, are shown in Figure 1.3.

Following an action potential, the cell is in a diastolic interval (DI) or recovery phase. During this phase, the ionic concentrations are restored by the rectifier channels while the Voltage remains at the resting potential. The first part of the DI is a refractory period, during which the cell cannot fire an action potential regardless of the stimulus strength. Following the refractory period, the subsequent AP will have a much shorter plateau and a shorter Action Potential Duration (APD) in general. The typical measure for this is the APD 90, defined as the period of time for which the action potential is above 90% repolarisation.

This definition is equivalent to the duration at which the voltage is above 0.1 if the AP voltage is scaled to be from 0 to 1. The APD is an important aspect of cardiac electrophysiology, as this has profound implications on the time at which the cell will be able to fire again, influencing all subsequent APs that pass through the cell.

APD properties can be investigated in both experimentation and model simulation by an S1-S2 protocol, in which the cell is given two stimuli at a certain time period apart (this time period is known as the basic cycle length (BCL)). At a long enough BCL for the cell to completely recover, APD_1 will equal APD_2. For shorter BCL, the second APD

will be shorter. This is known as restitution.

The APD restitution curve is a curve that shows how the APD of a single cell (typically the APD90) varies under S1 - S2 stimulation with different BCLs. The steepness of the APD restitution curve is often a predictor of how susceptible the heart is to an arrhythmia. On the x axis is either the basic cycle length (time between stimuli) or the diastolic interval (BCL-APD_1), while on the y axis is typically APD_2. As the period between stimuli decreases, the recovery time, and thus the next APD, are shorter.

Eventually, for a short enough BCL, S2 will fail to fire an AP, and the curve ends. When investigating these regions of the APD restitution curve, it is common to run multiple stimuli to either detect 2:1 firing behaviour (where one AP is fired for every 2 stimuli) or alternans [7]. Alternans (2:2) behaviour can occur close to the threshold BCL value between 2:1 and 1:1 firing behaviour, and occurs when a short DI triggers a short APD, which in turn triggers a long DI, and a long APD. The cycle can continue indefinitely, producing alternately long and short APDs (stable alternans) or can be unstable and tend towards 1:1 firing [8].

1.2.3   Cardiac Wave Propagation and Arrhythmia

The transfer of the AP from one cell to the next across an excitable medium is termed propagation. The propagation pattern (a travelling front that moves across the heart) is responsible for maintaining a regular contraction pattern from the SAN to the ventricles. Physiologically, this AP transfer is facilitated by gap junctions which allow ions to transfer between cells [9], but the purposes of this thesis, detailed descriptions of the underlying biophysics of this process are not relevant.

Propagation is simplest in a one-dimensional string or cable of heart tissue. In the human heart, this type of propagation is seen in the His-Purkinje complex. Under normal circumstances a stimulus given to one end of the cable will cause the first cell to fire an AP that will propagate to the other end, however, there are a number of factors that can disrupt this propagation. The speed of this propagation is the Conduction Velocity (CV). If the cell is forced too quickly (short BCL), the shorter recovery period leads to a reduced CV. At an even shorter BCL, either A) the stimulus may fail to exceed the firing threshold or B) the AP generated is too weak to exceed the firing threshold for all future cells, causing propagation to fail.

In two-dimensional tissue, a greater range of propagation patterns can be seen. Given

17

a rectangular sheet of heart tissue, a stimulus applied in the middle will create a circular or elliptical front that spreads out from the focus (target wave). AP propagation in a real heart is often anisotropic, i.e. the CV has a prominent direction, causing an elliptical shape in the emerging activation front. Many modelling works ignore this, and so simulated target waves are often circular. If one side of the sheet is stimulated at the same time, the resulting propagation front is a straight line (plane wave). Temporarily assuming that the heart tissue has no depth, the front created by the SAN is a target wave, and propagation patterns in the atria in a regular, healthy heart are target and plane waves.

Many types of arrhythmia can be explained by considering the two-dimensional propagation case. Propagation fronts can be disrupted by either an anatomical obstacle (e.g. physical scar tissue blocking the AP) or a functional obstacle (e.g the collision of wavefronts from two separate sources). Under these circumstances, it is possible for an activation front to travel in a circular pattern and return back to where it came from. This phenomenon is called a re-entrant wave, or spiral wave after the spiralling wavefronts created. During a spiral wave, the overall frequency of the heart rate is determined by how quickly the spiral can cycle (determined itself by the CV and restitution properties), rather than the BCL of the pacemaker. This often causes a heart rate that is regular but much quicker than sinus rhythm. Stable spiral waves are associated with atrial or ventricular tachycardia. The most dangerous cardiac arrhythmias occur when these spiral waves break up into smaller spirals, causing spatiotemporal chaos. In this state, seen during atrial or ventricular fibrillation, there is no order or coordination to the wavefronts at all. For this reason, atrial and ventricular fibrillation are a serious and immediate medical concern.

Cardiac arrhythmias are often diagnosed by the examination of the body surface ECG. For example, if there is no clearly defined P wave and a wavering baseline, the clinical cardiologist can infer that there is something wrong with the atria. A large delay between the P and the R wave can imply a blockage in the SAN. However, the body surface ECG is often insufficient to determine any information on a smaller scale.

In the case of atrial fibrillation, spiral waves are often caused by an ectopic (unwanted) wavefront originating from the Pulmonary Veins (PVs) instead of from the SAN (see Figure 1.2). Various clinical techniques have been developed that either target the elimination of the spiral wave itself through anti-arrhythmic drugs or block the origin of the ectopic signal by formation of lesions around the source. These lesions are most

commonly created by ablating tissue by application of radiofrequency energy, guided by intracardiac ECGs recorded around the vein ostium to monitor activity around the PV. A combination of the body surface ECG and intracardiac ECGs can help determine the activation time of localised regions in comparison to the rest of the heart. The primary goal of this thesis is to develop decision support tools that could help a cardiologist identify the optimal ablation location using intracardiac ECGs .

1.2.4 Modelling

Since cardiologists are using variation in the electrical signals recorded from the heart over time to make decisions about regions of the heart to ablate, mathematical modelling is a potentially suitable tool to provide additional relevant information.

We do this by studying the cardiac conduction system from a mathematical modelling perspective. Mathematical models are useful for both their explanatory and predictive power. Exploring how the parameters of a realistic mathematical model influence the solution can provide hypotheses for experimental testing and is easier than running experiments on physical cells. Investigation of a model also allows the varying of parameters that are impossible to control in reality, and ethical limitations are not a factor, allowing for a greater range of investigations into a beating heart.

Mathematical models also have the potential to be used to make predictions about the electrophysiology of the heart, which has obvious applications in deciding on the best methods of treatment [10], effects of drugs [11], and also in predicting heart attacks to guide an artificial pacemaker [12]. Inverse problems (working from the output back to the underlying input parameters) can also be used in diagnosis at no distress to the patient. One of the most simple methods for this is the clustering of ECGs into categories by fitting Hermite polynomials [13].

The most commonly investigated mathematical models of non-pacemaker cells are reaction-diffusion equations where the reaction term focuses on modelling the ionic currents behind the generation of the AP, and the diffusion term approximates the effect of gap junctions, allowing the simulated AP to spread across a series of coupled cells. The complexity of such models ranges from the simple two dimensional FitzHugh-Nagumo model [14] to much larger and more detailed more complex biophysical models, of which there are numerous reviews [15]. Models are typically solved either on a flat sheet of tissue using finite difference methods or on an anatomically accurate mesh using finite element methods.

In addition to reaction-diffusion equations of cardiomyocytes, models exist for the pacemaker nodes (SAN and AVN), typically taking the form of oscillators that resemble the van der Pol oscillator [16], i.e. capable of self-oscillating, and will phase lock to the rate of the fastest oscillator when coupled. Models for the body surface ECG signal range from phenomenological models whose solutions resemble the correct form [17] to biophysical models that model the conductance of both the heart and the entire torso, most importantly the ribs [18].

In this thesis, the main aim of the study is to develop techniques using mathematical modelling approaches that have the potential to be used clinically in the operating theatre during the treatment of Atrial Fibrillation (AF). For this reason, I am most concerned with phenomenological reaction-diffusion models of non-pacemaker cells which can model the atrial AP and related signal phenomenology in close to real time on a sufficiently realistic domain.

1.3 Thesis Outline

In chapter two, I review the relevant literature, starting with a review of recent AF research, covering prevalence and prognosis, what we believe today about the mechanisms behind the generation and sustenance of AF, and the efficacy of the current state-of-the-art in medical treatment, including clinical intervention (notably pulmonary vein isolation) and pharmacological treatments. We then review the advances in cardiac mathematical modelling, first covering initial attempts to model the heart and their modern day relevance, then the benefits and limitations of the hugely complex and detailed biophysical models prominent in the literature today. Finally, I introduce the key alternative phenomenological approaches to modelling of the cardiac AP that were developed to mimic the key properties of the biophysical models. Throughout the literature review, I present simulations showing the key properties and solutions of the models I discuss through the simulation of APs, restitution curves and two-dimensional simulations of heart tissue demonstrating the behaviour of cardiac rhythms in health and disease.

The third chapter discusses methods to optimise the parameters of a cardiac model. We discuss the classic hill-climbing methods often used as a first approach, and then contrast these with a genetic algorithm based method. Multi-objective parameter fits are explored as I characterise the pathways through parameter space from health to disease, and attempt to optimise multiple features of the cardiac model simultaneously.

Chapter four presents research on the development and use of phenomenological models in the use of a theoretical therapeutic decision support system to direct the application of radiofrequency ablation during pulmonary vein isolation. We first build a mathematical model of a clinical signal frequently recorded during this procedure, a model of which has not been produced before, using the parameters obtained for the cardiac model in chapter three. We use this to explore the potential of using the model to enhance the reliability of electrocardiogram recording in the operating theatre when some signals are not properly recorded. The model and associated decision support algorithms are validated using clinical data collected from Bristol Heart Institute.

Chapter five explores a different approach to the same problem: can the key features of the clinical signals of relevance to atrial fibrillation be accurately modelled without recourse to simulation of the underlying electrophysiology? A method is presented in which the activation pattern on the relevant catheter is accurately reproduced using an analytic function rather than a differential equation, validated with the same data as chapter four.

We follow on from this work in chapter six by testing the capacities of the methodologies presented in chapters four and five in a clinical setting. Signals recorded from patients undergoing AF ablation are modified to simulate information loss commonly occurring in clinic. This lost information is then reconstructed by the techniques presented in chapters 4 and 5. The validity of these techniques is compared in the context of guiding clinical decision-making by presenting a cardiologist experienced in atrial ablation with the original, modified and reconstructed signals. The cardiologist's choice of ablation target can then be compared to assess which of these two methods are most effective to minimise the impact of the information loss on clinical decision-making.

Chapter 2

Literature Review

2.1 Introduction

In this chapter I review the relevant background research to the thesis. In section 2, the biomedical background is discussed, beginning with a brief review of the classic and modern research on the underlying mechanisms of the generation and sustenance of AF. The biological section concludes with a review of clinical techniques, including pharmacological agents but focusing on radiofrequency ablation techniques to isolate the pulmonary veins.

The remainder of the review focuses on mathematical modelling techniques, beginning with a section presenting the numerical methods used to simulate cardiac arrhythmia. Secondly, the first attempts to model the cardiac action potential with a differential equation are discussed. These classical models have been superseded by modern models which provide more realistic description of the physiology, but provide useful historical context with which to place modern approaches. Next I focus on biophysical models, aiming to capture as much detail of the underlying physiology as possible. This invariably leads to large systems of differential equations and a long simulation time. We discuss the most prominent examples in the modern literature. Finally, modern phenomenological models are discussed. This type of model aims to reproduce the general behaviour of either the more complex biophysical models or data, but with much less biological and mathematical detail (such models are useful for situations in which simulations must be performed quickly). We explore three prominent examples (Fenton-Karma, Mitchell-Schaeffer and Bueno-Orovio Cherry Fenton) and present 2D simulations of cardiac arrhythmia using these models. For visualisation of travelling waves on a 2D domain, links are provided to video files.

2.2 Atrial Fibrillation and Radiofrequency Ablation Therapy

2.2.1 Prevalence and Prognosis

The heart is prone to a wide variety of pathological conditions, most commonly arising from wave propagation disruption as a result of functional or anatomical disturbances, or from pacemaker node dysfunction. Cardiac disease is the most common cause of death globally, especially among the adult population in the developed world [19]. Arrhythmias are cardiac conditions involving an irregular or otherwise abnormal heart rhythm. The most common serious cardiac arrhythmia is atrial fibrillation (AF) [20], a condition in which the wave propagation in the atria is disordered, which may be represented mathematically by a state called spatiotemporal chaos [21].

AF can have severely negative consequences on the quality of life of the patient. AF is the most serious cardiac risk factor for stroke, with stroke risk increasing by 480% in AF sufferers, as well as a threefold increased risk of congestive heart failure [22]. An estimated 15 - 20% of all strokes are a result of AF [23, 24]. Furthermore, other cardiac arrhythmias can be triggered by AF resulting from the lack of coordination between the atria and the ventricles, or the strain on the AVN [25, 26]. In general, AF carries a 1.5 - 1.9 fold mortality increase [27].

In addition to the severe consequences of AF, the high prevalence leads to a significant burden on public health. Adults aged 40 and above have a one in four chance to develop AF at some point in their lifetime, with 9% of over 80s currently living with the disease [20, 28]. In the UK, the cost of treating cases of AF and its consequences are estimated at £2 billion [29]. These statistics are only set to increase, partly as a result of greater longevity, more accurate diagnosis, and improved cardiac medical care meaning people can live with AF for longer, increasing prevalence [30]. In the USA, AF rates are projected to increase by more than double (to 5.6 million) by 2050 [31].

Furthermore, AF can often occur with no visible symptoms, and is frequently paroxysmal, which makes accurate diagnosis difficult and the true number of AF sufferers is likely to be higher than estimated [32, 33]. It is expected that a third to a quarter of all AF sufferers have not yet been diagnosed. The average delay between onset of symptoms and diagnosis of AF has been reported to be as high as 2.6 years [34].

2.2.2 Mechanisms of Atrial Fibrillation

AF is characterised by the disorder of the electrical activity in the atria, which dominates the pacemaking signal fired by the SAN. The contracting of the atrial myocytes is therefore uncoordinated, resulting in reduced cardiac output. While the firing rate of the SAN is roughly 60 to 100 BPM (sinus rhythm rate), during AF the firing rate of the atria can reach rates of 400 BPM [35, 36]. This is most dangerous when the AVN can no longer regulate the extremely high-frequency signals through to the ventricles. While not all atrial beats follow through to the ventricles, those that do result in an increased ventricular rate [35] and can lead to Ventricular Tachycardia (VT). This poses an immediate threat to the life of the patient.
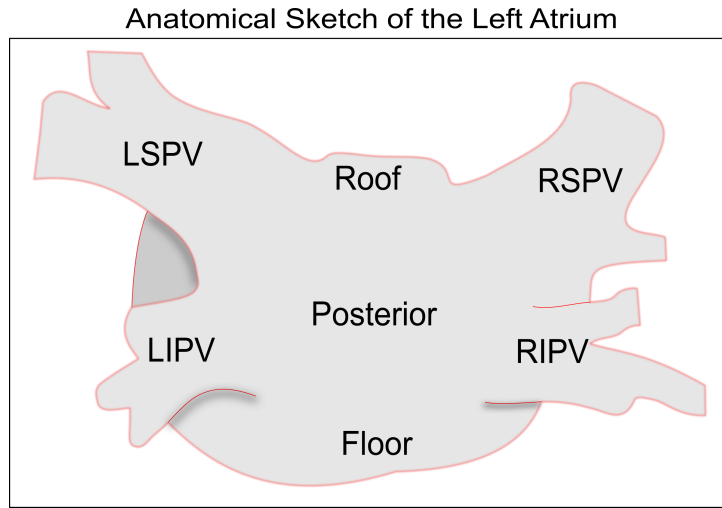
Figure 2.1: **Sketch of the Left Atrium.** Sketch of the left atrium including the pulmonary veins (PVs) (left superior (LS), right superior (RS), left inferior (LI) and right inferior (RI)). The posterior wall faces the chest.

AF is typically diagnosed from the body surface ECG by a fractionation of the P wave. In the typical PQRST complex of a normal ECG, the P wave is a consequence of atrial contractions, so with no coordination in the atrium, there is no well-defined P wave [37]. This is often one of the first clear clinical markers of AF. The AVN's inability to properly regulate these signals through to the ventricles can also sometimes result in irregular R-R intervals [38].

The main causes of AF are ectopic signals (am unwanted source of electrical activity separate from the nodes of pacemaker cells) and re-entrant circuits in the left atria [36, 39]. Ectopic beats are defined as spontaneous activation of cardiac myocytes independent of the SAN. These ectopic beats often fire much faster and dominate the SAN. The most

common ectopic focus location is in a small section of the left atrial myocardium that extends over the base of the pulmonary veins (PVs) (94% from Haissaguerre [40], and 88% from Chen [41]). A sketch of the left atrium, including the pulmonary veins, is given in Figure 2.1.

Although spontaneous activity of the PVs has been observed since the 1800s, there has been significant progress in recent years in understanding the mechanisms linking the PVs to AF [42]. AF can begin as atrial tachycardia (AT) from the rapid heart rate caused by the ectopic beats in the pulmonary veins dominates the firing rate of the tissue across the atria. The locations of the pulmonary veins can be important in the genesis and sustenance of AF.

Re-entrant circuits in this context are a functional or anatomical irregularity that allows an electrical impulse to travel back to where it started, causing a self-sustained 'rotor' (termed spiral wave mathematically). The atria are firing rapidly, but still in a roughly regular manner, a state classified as AT. Due to the spiralling pattern of recovering tissue, one directional blocks can occur, causing re-entrant circuits, spiral waves, and disordered dynamics [43]. This can lead to paroxysmal or persistent AF.

AT alters the physiological characteristics of the cells in a process known as remodelling. The two main effects relevant to electrophysiology are a reshaping of the atria (structural remodelling) and a change in the firing properties of the individual cells (electrical remodelling). Electrical remodelling alters the shape and properties of the AP by the modification of ion channel function. Remodelling can drastically decrease the size of the dome, APD and recovery time, lowering the APD restitution curve [11]. These changes largely occur as a result of increased activation of repolarising K^+ current [44].

Remodelling is the driving force behind the progressive nature of AF, as the progression from sinus rhythm to AT to AF is supported by the structural and electrical changes in the atria, increasing susceptibility to arrhythmia [45, 46]. As a result of remodelling, certain regions of tissue can fire much faster than they should normally, which supports the rapid nature of AF. Electrical remodelling has the end result of increasing the maximum firing rate of the cells during AF, leading to the abnormally high firing rates reaching 400 BPM. The shorter APD increases the likelihood of spiral waves to break up, causing AF.

2.2.3 Clinical Procedures

There exist a number of different clinical approaches for dealing with AF. Antiarrhythmic drugs remain a common treatment method today, over 100 years since their introduction to the medical community [47]. The majority of antiarrhythmic drugs focus on the inhibition of the K^+ current to increase the APD and reverse the effects of electrical remodelling. Alternatively, Na blockers reduce cardiac excitability, reducing the chance of arrhythmia occurring, however as all antiarrhythmic agents affect more than one channel, in practice categorisation, is difficult. K^+ is usually targeted, as this current is not so prevalent in the ventricles, in theory allowing for atrial-targeted ion channel control [48, 49]. However, it is impossible to effectively target specific channels in isolation, for example, amiodarone, presently the most commonly prescribed drug, inhibits the I_{Kr}, I_{Na}, I_{Kur}, I_{to}, $I_{Ca,L}$, and $I_{K,ACh}$ channels [50].

Unfortunately, pharmacological agents for the treatment of AF are associated with only moderate success rates, high recurrence rates, and dangerous side effects [51]. As it is impossible to target only the atria, drug treatment for AF can also affect the ventricles, resulting in an increased risk of ventricular arrhythmias, which are often more dangerous than their atrial counterparts. It has been well known for quite some time that antiarrhythmic drugs can have proarrhythmic effects [51]. A large scale 2011 study on the efficacy of antiarrhythmic drugs identified amiodarone as the most effective drug for terminating AF, but also had the highest rate of an adverse effect occurring, and an overall increased mortality. Dronedarone, a popular alternative, has been found to have a higher recurrence rate of AF, but fewer proarrhythmic events [52]. There is no evidence for a reliably effective and safe antiarrhythmic drug in the treatment of AF.

As an alternative, radiofrequency ablation (RFA) is a minimally invasive surgical technique that has emerged in the last couple of decades as the leading technique for the treatment of paroxysmal AF. RFA uses a catheter (called the ablator) to deliver pulses of radiofrequency energy to burn lesions into the heart tissue with target temperatures of 50 - 55 °C [53, 54]. The lesions formed block the conduction of the AP.

Recently, many creative alternative techniques have been developed for ablation. One such alternative to RFA is cryoballoon ablation, which works by freezing cells instead of burning them, although the two techniques have similar levels of success [55, 56]. Laser Balloon Ablation, in which the veins are ablated by a continuous laser beam [57], is another alternative. As balloon catheters have not yet been widely adopted by the clinical community, it is difficult to make any comparisons between technologies. A 2016 review

stated 'it is important to note that the investigators did not have prior experience with using the investigational catheters' when comparing effectiveness of cryo and laser balloon catheters with the traditional RFA approach [58]. In this thesis, we focus on RFA, as it is by far the most commonly used technology in the present day, and used by our collaborators in both Bristol and Bordeaux, where data was collected.

The origin of the ectopic beats causing the arrhythmia is often within the PVs. To treat AF, RFA is applied around the PV ostium to block any ectopic signal escaping. This technique, called pulmonary vein isolation (PVI), was first developed by Professor Michel Haïssaguerre and documented in 1998 [40]. After successful PVI, a continuous circular lesion is formed around the PV. This isolates the PV from the rest of the atrium so that the ectopic signals can no longer propagate outwards.
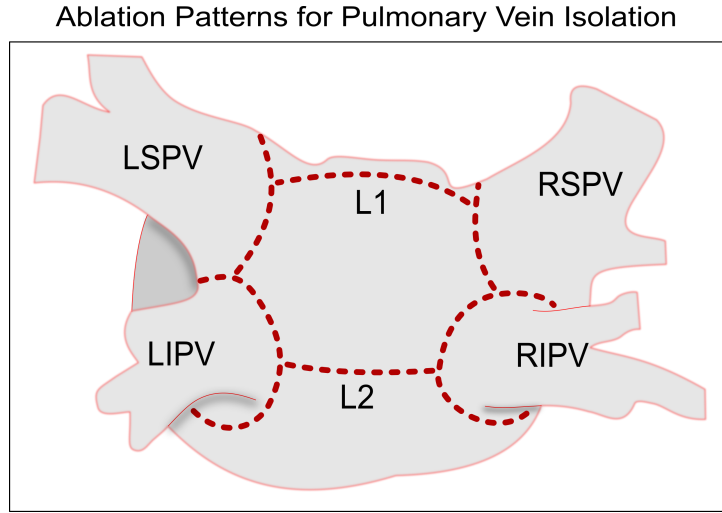
Figure 2.2: **Ablation Strategies for Pulmonary Vein Isolation.** Sketch of the left atrium including dashed lines representing lesions resulting from pulmonary vein isolation by radiofrequency ablation. CPVI lesions encircle the base of the veins, L1 indicates roofline ablation and L2 is the second linear lesion. Together, these form a CVPI+L1+L2 strategy.

There are three different strategies for radiofrequency ablation. Circumferential pulmonary vein isolation (CPVI) describes the circular lesions surrounding and isolating the pulmonary vein. Linear ablation consists of straight lines of ablated tissue, typically from one part of the heart to another. Roofline ablation is a common linear ablation technique which consists of a continuous line joining the superior pulmonary veins (L1), which in combination with CPVI, has been shown to increase effectiveness with few complications [59]. Secondly, it is common to join the inferior pulmonary veins across the posterior wall by another linear lesion (L2). The third ablation strategy, complex fractionated atrial

electrogram (CFAE) ablation, consists of targeting specific points on the atrium with unusual electrophysiological properties, such as a very short cycle length out of synchrony with the rest of the atrial firing rate [60], resulting in nonconductive cells spread across the atrium, which causes spiral waves to break up and dissipate as seen in model studies [61]. These general ablation strategies are consistent across the various technologies available to ablate the veins.

Meta-analyses that perform comparisons of ablation strategies have found mixed results [62]. This is most likely as it is difficult to isolate strategy as the only variable, therefore when comparing outcomes of two trials using different strategies, skill level and technological availability to the clinician also skew results. However, trials involving multiple ablation strategies tend to lean towards a hybrid approach, such as CPVI + CFAE, being the most effective at restoring sinus rhythm [63, 64]. From the available clinical trial data, we conclude that CPVI is necessary but not always sufficient for effective AF treatment. A recent modelling study predicted that CPVI with both linear ablation lines will have the highest antiarrhythmic effect [10]. Figure 2.2 shows a CPVI + L1 + L2 ablation strategy.

In my experience in clinic, CPVI is often the first approach to AF ablation, followed by linear ablation lines if CPVI fails to isolate the veins. However, cardiologists of a similar level of experience at the same institute will often have differing opinions on what the next move should be during a case, to the extreme case of disagreeing on what side of the heart the arrhythmia is coming from when presented the same information. In general, the exact choice of ablation strategy appears to depend on the personal preference and intuition of the clinician.

Perfect isolation is a difficult task, as the movement of the ablator can often leave small conduction gaps in the lesion [65, 66]. This is problematic for two reasons: a conduction gap allows electrical impulses to escape the vein, compromising the effectiveness of the procedure, and secondly, lesions that do not successfully isolate the target area simply create more anatomical obstacles, which can be pro-arrhythmic. Work undertaken in this thesis provides no insight into which ablation strategy is the most effective, but is focused on ensuring that a circular line of lesions is successfully formed in the first place.

Whilst the initial success rate of pulmonary vein isolation is approximately 85% [67], recurrence rates 5 months after ablation therapy can be as high as 30% in paroxysmal AF patients or 78% in permanent AF patients [53]. One popular clinical hypothesis for the
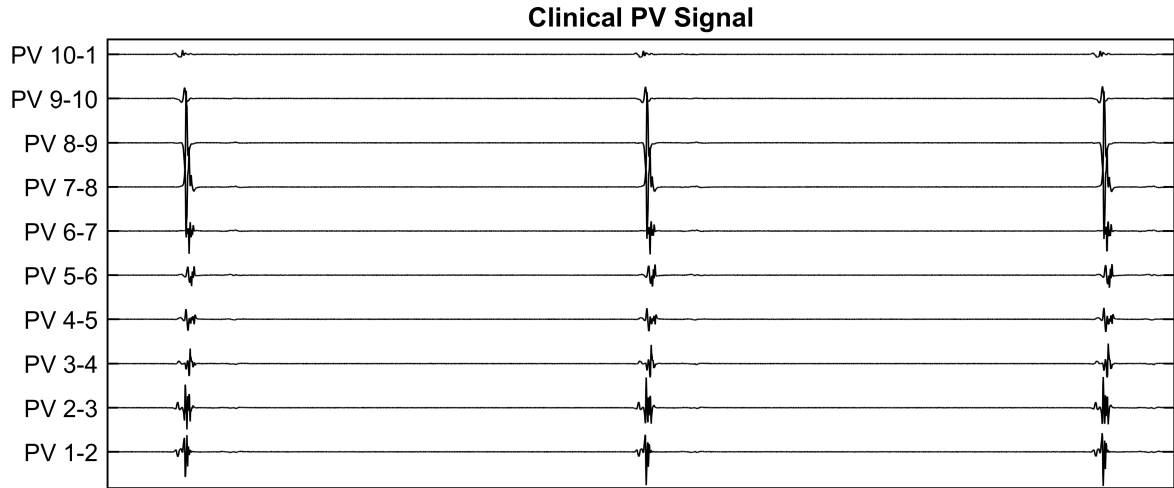
Figure 2.3: **Clinical Pulmonary Vein Recording.** The PV recording of a patient with AF during PV isolation therapy. Bipolar recordings were obtained from a deflectable, circular, 10-pole Lasso catheter (Biosense Webster Ltd).

processes underlying recurrence is tissue regeneration within the ablated lesion, leading to new conduction gaps that undo the effect of the surgery [66].

There are several ablation devices available to isolate the veins (e.g. nMARQ, Biosense Webster) [68]. During the isolation procedure, small conduction gaps in the lesion, which may be caused by poor depth penetration of the lesion, incomplete ablation, or tissue healing over time, must be ablated. Bipolar recordings of electrical activity around the pulmonary vein are taken using a lasso catheter typically consisting of 10 or 20 electrodes. Figure 2.3 shows an exemplary time-trace recorded at the University Hospital of Bordeaux from a deflectable, circular, 10-pole Lasso catheter (Biosense Webster Ltd) during sinus rhythm. The activation pattern of the recorded electrical activity on the lasso catheter is used as a guide towards where to ablate. Further application of ablation is performed at the site or sites at which the first spikes are observed [40, 69].

However, it is common for some electrodes to make poor contact with the tissue, and not display a useful recording. If these missing channels correspond to the region of first activation, this information loss could potentially lead to ablation of the wrong region. Such issues continue to inhibit further development of techniques involving bipolar lasso catheters. In 2011 a method was proposed to infer a PV activation map by gentle movement of the catheter [70], however, the authors raised concerns that this approach resulted in unreliable signals, due to some electrodes touching the endocardium whilst others were not. Further, electrodes located symmetrically with regard to a conduction gap will record a zero signal despite a wavefront passing, this is a known weakness of

bipolar recordings and can cause additional signal loss even at sites with proper contact of the electrodes with tissue.

Ablation of the pulmonary veins carries a risk of pulmonary vein stenosis [71] and if complete electrical isolation is not achieved, the lesions can become pro-arrhythmic through the creation of conduction obstacles that facilitate the initiation of reentrant waves. Consequently, it is desirable to minimise both the time taken to perform the procedure as well as the amount of scar tissue formed through ablation by more accurately determining the optimal ablation location. Information loss that increases the difficulty of this task is potentially dangerous as well as increasing the duration of the procedure. The remainder of this review focuses on mathematical models of the cardiac AP, beginning with a section on general numerical methods used in modelling of cardiac arrhythmia.

2.3 Numerical Methods for Cardiac Modelling

2.3.1 Coupling of Cardiac Cells

In cardiac tissue, cells are electrically coupled via gap junctions, which allow the propagation of an AP. This transfer is facilitated by the transfer of ions (primarily sodium, calcium and potassium) across the gap junction. When one cell is excited, this transfer of ions raises the voltage of its neighbours, and should this excitation be sufficiently strong, the cell will fire an AP which will propagate further. Numerically, this is approximated by nearest-neighbour diffusive coupling using a term $\nabla(D\nabla u)$. This diffusion term, plus the reaction term from the models previously described, creates a reaction-diffusion equation capable of modelling many cardiac conditions.

Numerically, we typically solve these equations using the finite difference method. The more complex finite element method is used when solving cardiac models on more complex domains, such as an anatomically accurate mesh, but these are not necessary for our goals. Numerical simulations require discretisation of the domain into a finitely sized grid or mesh that represents a region of cardiac tissue. For isotropic 2D simulations, we use a simple five point stencil and the central difference method to approximate the spatial derivative, as shown in Figure 2.4. In this chapter Neumann Boundary Conditions are used on all boundaries, implemented by a 3 point stencil on the edges and 2 on the corners, effectively allowing the travelling wave to propagate out of the domain.
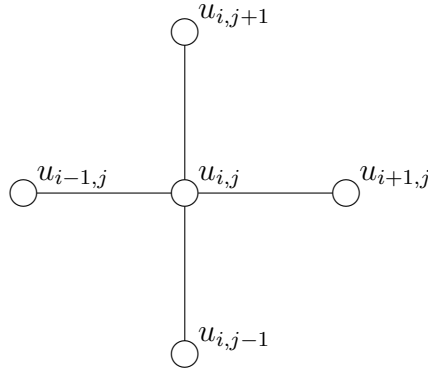
$$\nabla(D\nabla u_{i,j}) \approx u_{i,j-1} + u_{i,j+1} + u_{i-1,j} + u_{i+1,j} - 4u_{i,j}$$

Figure 2.4: **Five Point Stencil for the Finite Difference Method.** A schematic of the approximation method used for the diffusion term $(\nabla \cdot (\tilde{D}\nabla u))$ for isotropic simulations performed on a two dimensional uniform grid (rectangular, cylindrical or toroidal). Time derivatives are approximated by the forward Euler method.

2.3.2 Anisotropy

In the five point stencil displayed in Figure 2.4 diffusion is isotropic, i.e. diffusion is constant in every direction. However, in cardiac tissue, the AP primarily propagates along fibres. The CV in the direction parallel to the fibres is therefore much faster than the velocity in the perpendicular directions.
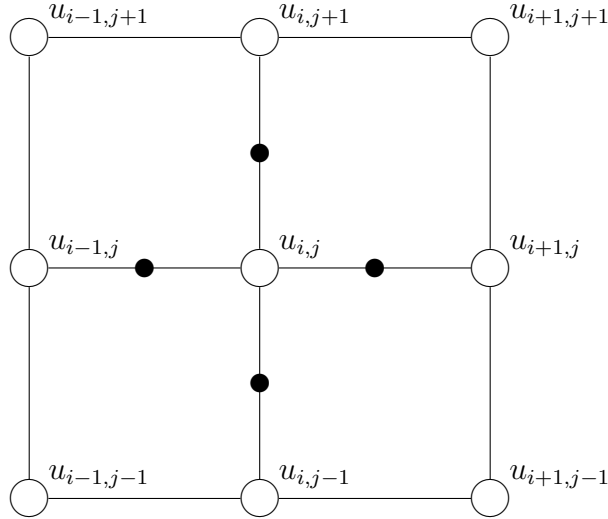
Figure 2.5: **Nine Point Stencil for the Asymmetric Finite Difference Method.** A schematic of the approximation method used for the diffusion term $(\nabla \cdot (\tilde{\mathbf{D}}\nabla u))$ when we consider anisotropy (different diffusion speeds in different directions). For the asymmetric scheme used, $\mathbf{D}$ is defined on the half indices (black circles).

Anisotropy has been well studied in both ventricular and atrial tissue. In ventricular

muscle, a ratio of 3:1 has been observed between conduction velocities in the directions longitudinal and transverse to the fibres (the degree of anisotropy) [72], which has been known in animal hearts since at least 1959 [73]. Recent research using high-resolution optical mapping in the canine atria has indicated that the degree of anisotropy increases with age, from 4.5 in the infant group up to 10 in the old group [74].

However, in a study of 12 patients undergoing open heart surgery in the right atrium [75], found that the ratio of the velocities of the fastest to the slowest conduction directions ranged only between 1.15 and 1.8, and that CV was not dependent on propagation direction. This degree of anisotropy is similar to values used in [76], driven by the clinical data collected from patients undergoing PVI [77]. Due to these discrepancies in experimental and clinical studies, when considering anisotropy in fits to clinical data, we allow the dominant angle and anisotropy degree (the eigenvectors of the diffusion tensor) to vary.

In three dimensional tissue, a further factor affecting diffusion patterns is the twisting dominant fibre direction throughout the tissue. This twist can affect the dominant propagation direction from the epicardium to the endocardium by between 120 and 180 degrees. An excellent description of 'rotational anisotropy' and its effects on excitation spread in the Fenton-Karma model can be found in [78] (this is also the paper that first introduced said model). More recently, it has been claimed that the effect of this can be approximated by using only two layers representing the epicardium and the endocardium [79, 80]. Detailed consideration of this effect, however, is outside the scope of this thesis as we deal only with two-dimensional domains.

As we only consider two-dimensional homogeneous domains when dealing with reaction diffusion equations in this thesis, finite difference methods are sufficient for dealing with all diffusion terms. However, using the 5 point stencil as shown in Figure 2.4, we are limited to the longitudinal and transverse diffusion directions being parallel to the x and y axis. To solve this issue and handle anisotropic diffusion with longitudinal diffusion coefficient $D_\parallel$ in the angle α and $D_\perp$ in the transverse direction, we use a 9 point stencil, and use the asymmetric finite difference method as shown in [81]. As a result, we use a diffusion tensor

$$\mathbf{D} = \begin{pmatrix} D_\parallel b_1^2 + D_\perp b_2^2 & (D_\parallel - D_\perp)b_1 b_2 \\ (D_\parallel - D_\perp)b_1 b_2 & D_\perp b_1^2 + D_\parallel b_2^2 \end{pmatrix}, \tag{2.1}$$

defined on the half indices as shown in Figure 2.5. The method is known as an asymmetric

method due to calculating diffusion on the half-indices requiring different treatment in the x and y axes. If the tensor $\mathbf{D}$ is constant, the calculations reduce to

$$
\begin{aligned}
&\nabla(D\nabla u_{i,j}) \approx \\
&- \left(\frac{D(1,1)(u_{i+1,j} + u_{i-1,j} - 2u_{i,j})}{\Delta x} + \frac{D(1,2)(u_{i+1,j+1} + u_{i-1,j-1} - (u_{i-1,j+1} + u_{i+1,j-1}))}{4\Delta y} \right) /\Delta x \\
&- \left(\frac{D(2,1)(u_{i+1,j+1} + u_{i-1,j-1} - (u_{i-1,j+1} + u_{i+1,j-1}))}{4\Delta x} + \frac{D(2,2)(u_{i,j+1} + u_{i,j-1} - 2u_{i,j})}{\Delta y} \right) /\Delta y,
\end{aligned}
\tag{2.2}
$$

a full derivation of which is contained in Appendix B. If diffusion is isotropic such that $\mathbf{D} = D\mathcal{I}$, Equation (2.2) reduces to the five point stencil in Figure 2.4.

2.3.3 Modelling of Cardiac Arrhythmia

The most simple domain capable of representing the propagation of the cardiac AP is a one-dimensional chain of cells. The 'cable' can be used to model cardiac conduction in the His-Purkinje fibres, where conduction mostly occurs along fibres. In terms of simulation, a one-dimensional domain allows for much quicker simulation than two or three dimensions, and so is useful for quantifying features such as speed of the travelling wave, or AP features in the travelling wave solution, which often differ to the model being run at a single point.

This can extended to a two-dimensional domain, representing a sheet of cardiac tissue. In a two dimensional sheet, depending on the location and spatial shape of the stimulus, plane waves (from stimulating one edge of the domain) and target waves (from stimulation at a single point) can be generated. We present target and spiral waves from a variety of models and for both isotropic and anisotropic diffusion in section 2.5 when we discuss phenomenological models.

In the simplified case of a two-dimensional sheet of tissue, it is possible to induce spiral waves representative of tachycardia, and breakup leading to spatiotemporal chaos, modelling fibrillation. While it is possible to perform these simulations on an anatomically realistic mesh, we present results in a two-dimensional flat slice of tissue to provide an overview of spiral wave dynamics in cardiac models with minimal computational intensity.

Spiral waves can be initiated by perturbing a travelling plane wave in three different ways. Firstly, we can initiate a collision of wavefronts by 'cross-field stimulation', de-

scribed in detail in [82] and [83]. The S1 stimulus creates a plane wave that travels from left to right across the plane. When the wavefront has propagated half-way across the sheet, the S2 stimulus is applied to the bottom boundary, creating a wavefront collision that breaks the S2 wavefront in half, resulting in a spiral wave.

Secondly, an ectopic stimulus applied to the waveback of a travelling plane wave. The second stimulus cannot propagate in the same direction as the first, as this tissue is still recovering. The only available pathway is back towards the source of the S1 stimulus, causing re-entry. This stimulation protocol can result in a 'double spiral wave, which then breaks down into several independent sources' [84] page 251. This is consistent with results of our simulations using this procedure with the Fenton-Karma model, available at `https://www.youtube.com/watch?v=IKybSM8gD8s`. However, the timing required for this is very precise and difficult to reliably reproduce. If the second stimulus is applied to early, there will be no propagation in either direction and if too late, will simply produce a second plane or target wave.

Finally, we can reset the top half of the plane to the resting potential over a single time step, as described by [85], The Virtual Heart's Java Applets, and many others. The half plane reset is less sensitive to timing and so easier to simulate, but less physiologically plausible as an initiation mechanism.

2.4 Early Mathematical Models

2.4.1 Van der Pol

In this section we describe the earliest models in the literature, designed when little was known about the intracellular dynamics.

Model 2.1 *Van der Pol Oscillator*

$$\ddot{v} - \mu(1 - v^2)\dot{v} + \omega^2 v = 0 \tag{2.3}$$

The Van der Pol Oscillator is a classic dynamical system prominent in many areas of applied science, and a staple of many undergraduate mathematics courses in nonlinear dynamics. Proposed initially in the 1920s, the Van der Pol Oscillator is a second order differential equation capable of exhibiting 'relaxation oscillations', which are stable limit cycle attractors with a non-sinusoidal solution [16]. With $\mu = 0$ the equation reduces

to $\ddot{v} + \omega^2 v = 0$, which has trivial sinusoidal solutions of period ω. Increasing the parameter μ causes the oscillations to become increasingly 'sharp' as seen in Figure 2.6. Frequently for use in applications, the Van der Pol Oscillator is either forced or coupled together in a network of oscillators representing a node of coupled pacemaker cells [86, 87].

Forcing of the Van der Pol Oscillator was an early example of deterministic chaos. When forced with a function $A \sin \omega t$, and in certain regions of the parameter space spanned by μ, A, and ω, the solutions of the oscillator tend towards a stable chaotic attractor with positive maximal Lyapunov Exponent [88, 89]. The seemingly random fluctuations recorded at certain frequencies in experiment in the late 1920s were initially dismissed as noise, but are now believed to have been recordings of deterministic chaos [90] long before the work of Lorenz [91].

Shortly after the development of the oscillator, Van der Pol and Van der Mark explored the potential for its use as a cardiac model [87]. Their model, the first mathematical approach to modelling the human heartbeat, consisted of three oscillators representing the sinoatrial node, the atria, and the ventricles. Some 50 years later, the qualitative features (notably the phase locking behaviour) of this model were verified experimentally [92]. In the electrical conduction system of the heart, the overall frequency of the heartbeat is most commonly regulated by the frequency of the fastest element. Systems of coupled Van der Pol oscillators are useful for modelling the cardiac conduction system as this property is conserved - a network of coupled Van der Pol oscillators will phase lock to the frequency of the fastest oscillator, without affecting the amplitude [2, 93]. Furthermore, period doubling bifurcations, the route to chaos exhibited by a forced Van der Pol oscillator, have been observed experimentally in cardiac pacemaker cells [94].

The use of Van der Pol oscillators in cardiac modelling remains useful in the present day, even after the advent of the powerful biophysical reaction diffusion equations that now dominate much of the literature on the subject. A modified version of Van der Pol, from Grudzinski [2], is a popular phenomenological model for the self-excitatory cardiac pacemaker cells of the sinoatrial and atrioventricular nodes and will be discussed later in the chapter. As the Van der Pol oscillator is self-oscillating, it cannot be used to model the behaviour of atrial or ventricular myocytes. Figure 2.6 shows the solution of Van der Pol oscillator resembling the SAN AP. Later in the review, an extended Van der Pol model is fit to a more realistic model to demonstrate how realistic these APs are.
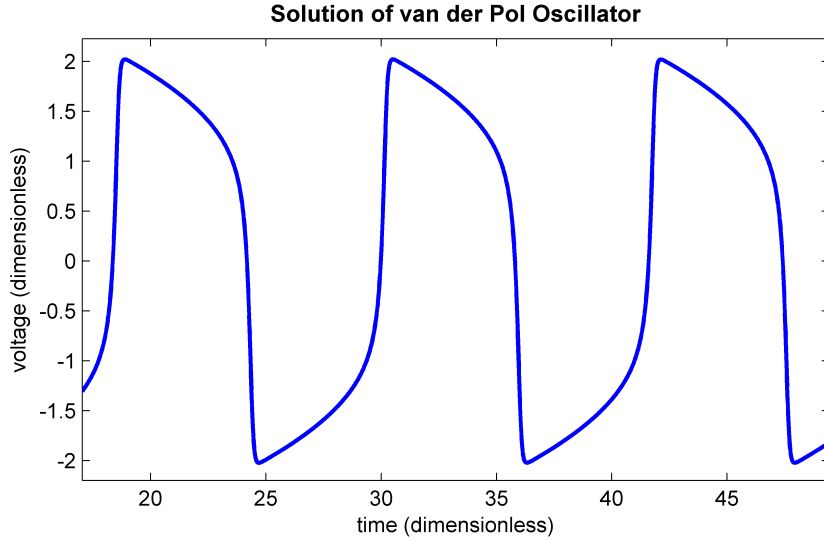
Figure 2.6: **Solution of van Der Pol Oscillator.** The solution of the van der Pol Oscillator resembles the APs generated by the SAN, and was one of the earliest mathematical models used in cardiac modelling.

While the solution of the Van der Pol oscillator does roughly match a real cardiac pacemaker's AP, the lack of biological detail included limits its usefulness in clinical research. As previously discussed the cardiac AP is generated by underlying ionic currents. However, the Van der Pol oscillator pre-dates the mathematical equations for describing these processes, the Hodgkin-Huxley equations, which were not developed until 1952 [95]. As such the biological processes behind the AP generation are not described by the Van der Pol oscillator, and the equation itself has no biological significance. Accordingly, it is impossible to realistically simulate the effect of any pathological conditions at the cellular level, since the parameters μ and ω have no physical meaning. The model has since been modified by numerous authors to add greater detail and/or realism, and modern efforts are described in section 2.4.3.

2.4.2   FitzHugh-Nagumo

Model 2.2 *FitzHugh-Nagumo Model for Neuronal Action Potential*

$$\dot{v} = \alpha \left(v - \frac{v^3}{3} - w \right) + I_{\text{ext}}$$
$$\dot{u} = \mu(v + \beta - \gamma w)$$

(2.4)

The FitzHugh-Nagumo model is a reduction of the Hodgkin-Huxley model [14] that is effectively a modification of the Van der Pol Oscillator. The Hodgkin-Huxley model is a Nobel Prize-winning model described in 1952, developed to simulate the AP propaga-

36

tion in the squid giant axon by a system of four nonlinear ODEs that approximated the underlying ionic mechanisms [95]. Although containing only the potassium, sodium and leak currents, the Hodgkin-Huxley model was the first electrophysiological model based on the underlying biological mechanisms (a biophysical model). Almost every successful mathematical model of electrophysiology since has its roots in the Hodgkin-Huxley model, whether it be a biophysical 40+ dimensional cardiac myocyte model or a phenomenological reduction. A more detailed review of the Hodgkin Huxley equations with respect to the Cardiac Physiome Project can be found in [96]. The Hodgkin-Huxley model is a reaction-diffusion equation. The system of ODEs make up the reaction term, and a diffusion term allows the pulse to propagate through a medium (e.g. cardiac tissue or a neuronal axon).

The equations of FitzHugh-Nagumo were designed to reproduce the basic qualitative behaviour of the Hodgkin-Huxley model, with neuronal AP propagation in mind [14], although like the VdP Oscillator the parameters are purely phenomenological and have no direct biophysical analogue. In the context of electrophysiology, v is the voltage term which produces a spike or AP, and w is a recovery variable which inhibits v for a duration after the AP. I_{ext} is an external stimulus being applied to the model. While $I_{\text{ext}} = 0$, solutions tend to a stable equilibrium. If provided a strong enough stimulus, the solutions will take an excursion in phase space along the $\dot{v} = 0$ nullcline before returning to the equilibrium point.

Due to the model's genericity and simplicity, it is a popular example of a travelling wave model, as it is easy to study analytically as well as very fast to simulate. If multiple FitzHugh-Nagumo type 'cells' are coupled together with a diffusion term (typically such that $I_{\text{ext}} = \nabla(D\nabla u)$), the result is a travelling pulse solution. In this PDE formulation, the FitzHugh-Nagumo model is a generic reaction-diffusion equation, with applications in ecology, physics, and chemistry, among numerous other areas of applied science in which the study of wave dynamics is relevant.

Within cardiology, the FitzHugh-Nagumo model is the simplest model used for the propagation of the AP of atrial or ventricular myocytes. FitzHugh-Nagumo based models have been described as 'good for a first qualitative study, but, of course, are not adequate for a detailed quantitative description' [97]. This may be more applicable to modelling a problem if the use of a biophysical model is too difficult or time-consuming, as the FitzHugh-Nagumo model can be run on a large domain in a matter of seconds, unlike some biophysical models which will be discussed later. While the model is quantitatively

inaccurate for the vast majority of cardiac applications, it is still able to qualitatively reproduce the most common wavefront patterns frequently seen in cardiac cells, such as target, plane, spiral and scroll waves.
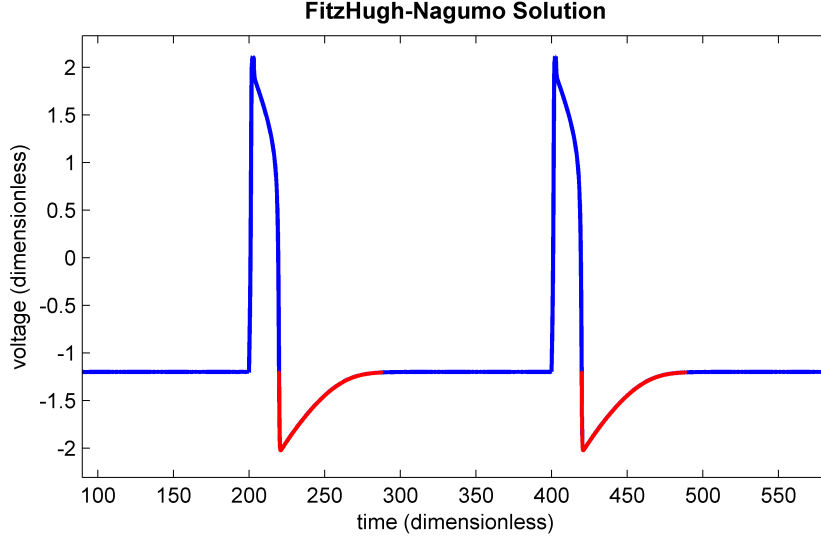
Figure 2.7: **Action Potentials from the Fitz-Hugh Nagumo Model.** Action potentials generated by forcing the FitzHugh Nagumo model with small spike waves with a period of 200 to produce an action potential. The red region of the action potential (below the baseline) is a hyperpolarisation, which is unrealistic in cardiac cells.

If stimulated at a point in the centre of a two-dimensional sheet of synthetic tissue, circular 'target waves' will propagate outwards from the point of stimulation. If stimulated along one edge of the domain, a plane wave will propagate from one side of the sheet to the other. Thirdly, and of most critical importance to simulations of cardiac electrophysiology, FitzHugh-Nagumo travelling waves can be disrupted by either functional disturbances (alterations to v, such as an ectopic stimulus), or by an anatomical disturbance (such as a physical block or slow conduction path) to create spiral waves [86, 98, 99]. Spiralling of cardiac excitation waves are the underlying phenomena of the vast majority of dangerous cardiac arrhythmias, such as AT, AF and VF. In a three dimensional domain, scroll waves are formed [97].

There are also functional limitations of the FitzHugh-Nagumo model. The breakup of spiral waves that describes the transition from stable spirals (tachycardia) to spatiotemporal chaos (fibrillation) is difficult to reproduce with the FitzHugh-Nagumo equations, even qualitatively, mostly due to the unrealistic restitution behaviour primarily caused by the hyperpolarisations (red part of Figure 2.7) that occur after an AP. These are not present in cardiac myocytes. While hyperpolarisations have been addressed by certain

modifications, such as the Ailev Panfilov model [100], which will be discussed in more detail in the following section, the model is generally not a good representation of cardiac tissue, and wave propagation in FitzHugh-Nagumo type cells can be very different from in tissue [101]. In modern cardiac literature, results obtained from the FitzHugh-Nagumo model are often validated by a more realistic model, as described in [98]. Validation of a simple model by a complex one allows the use of the simple model for the speed of computation.

2.4.3 Recent Adaptations of Historical Models

With the benefit of additional experimental data and mathematical techniques available, authors have subsequently modified the van der Pol oscillator and FitzHugh-Nagumo equations to better represent reality while maintaining a similar complexity. In 2004, Grudzinski and Zebrowski replaced the harmonic $\omega^2 v$ term in Equation (2.3) with a cubic term from the Duffing equation [102] $(v(v + d)(v + d))$, creating a combination of the Duffing and Van der Pol oscillators, originally proposed in [2]. Later this was modified to $vf(v + d)(v + e)$ [103], where d, e and f are additional parameters. The model is then given by:

Model 2.3 *Modified van der Pol Oscillator*

$$\ddot{v} + \alpha(v^2 - \mu)\dot{v} + vf(v + d)(v + e) = 0. \tag{2.5}$$

This modification adds two additional fixed points to the phase portrait of the van der Pol oscillator. In addition to the unstable spiral (which tends to the stable limit cycle), the modified oscillator contains a stable node at $v = -e$ and a saddle at $v = -d$, the stable manifolds of which are separatrices which divide the phase plane into two basins of attraction. The second modification (as seen in Equation (2.5)) allows independent control of the locations of the stable node and saddle point. Sufficiently high initial voltage will cause the cell to enter the stable oscillation regime, while on the stable focus side of the separatrix, solutions will tend towards the focus. However, while a pacemaker cell can flat-line, and can produce stable oscillations, the conditions are far more complex than initial voltage. A large enough external stimulus can push the cell from its stable equilibrium point $v = -e$ over the separatrix to produce oscillations. However, the authors state in their original paper [2] that: *The justification in making this improvement is that the phase space of Equation (2.5) resembles the phase spaces [104] of the Morris–Lecar model of the neuron membrane [105].* Evidence that this resembles the phase spaces of cardiac oscillators, however, is not given, and it is a curious decision to base the dynamics
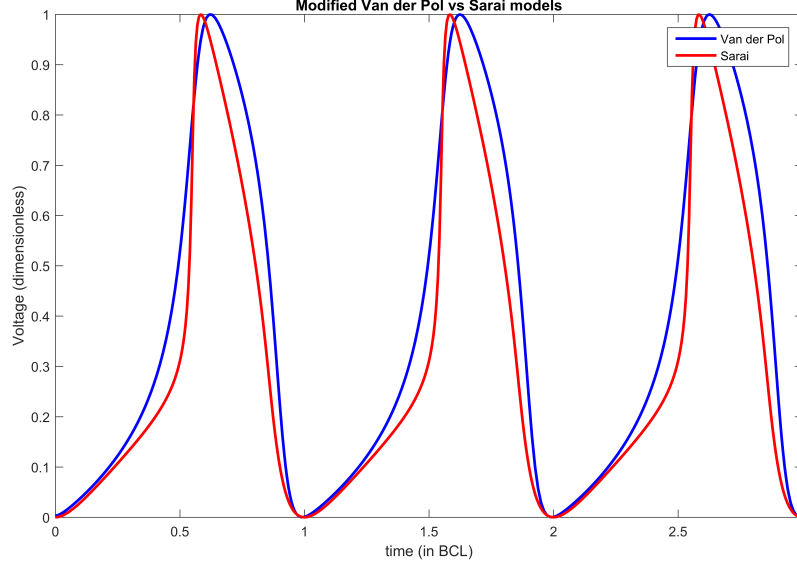
Figure 2.8: **Modified Van der Pol Oscillator vs Sarai Model.** Graph showing three action potentials of the optimal fit of the Modified Van der Pol oscillator to the Sarai model. Fit was performed using the Nelder-Mead Simplex Search.

of a cardiac pacemaker node model on a neuronal AP model when biophysical dynamic models for the cardiac pacemaker AP existed at that time, such as the Kurata model [106].

Nonetheless, the model does reproduce cardiac dynamics relatively well and shows good accordance with recorded AP data. Figure 2.8 shows how close the solutions of Equation (2.3) match the detailed 2003 biophysical model from Sarai et. al. [107], which consists of 41 variables, 99 constants and 146 functional parameters used in computation, used as a proxy for real data. We calibrated parameters by using the Nelder-Mead Simplex Search (NMSS) method to minimise the root mean squared (RMS) error through the entire time trace. Furthermore, it is a simple task to adapt the frequency or amplitude of the AP independently by variation of a single parameter, giving easy control of the model solutions. The oscillator can equally accurately model either the SAN or the slower AVN by variation of the parameter e. When two of these oscillators are coupled, the slower one will phase lock to the frequency of the faster one, much the way the AVN naturally oscillates at a slower frequency to the SAN but will lock to the same frequency during normal cardiac propagation.

Figure 2.9 shows a simulation of this behaviour using two cells modelled with the modified Van der Pol oscillator. The red curve represents the SAN, with $e = 12$, and the blue curve represents the AVN, with $e = 7$ [2]. All other parameters are identical,

and without coupling, the AVN oscillates slower than the SAN. The AVN is coupled to the SAN with one directional diffusive coupling, which is turned on at $t = 25$ in the simulation, resulting in the AVN being locked to the rate of the SAN.

By coupling this oscillator with FitzHugh-Nagumo cells, very simplified models of the atria have been developed, using the Modified van der Pol to model cells in the SAN and AVN, and FitzHugh-Nagumo cells for the atrial myocardium between them. This allows realistic simulation of conduction block caused by a propagation delay across the junction between node and myocardium [103], however, this simulation was performed only in a one-dimensional cable.
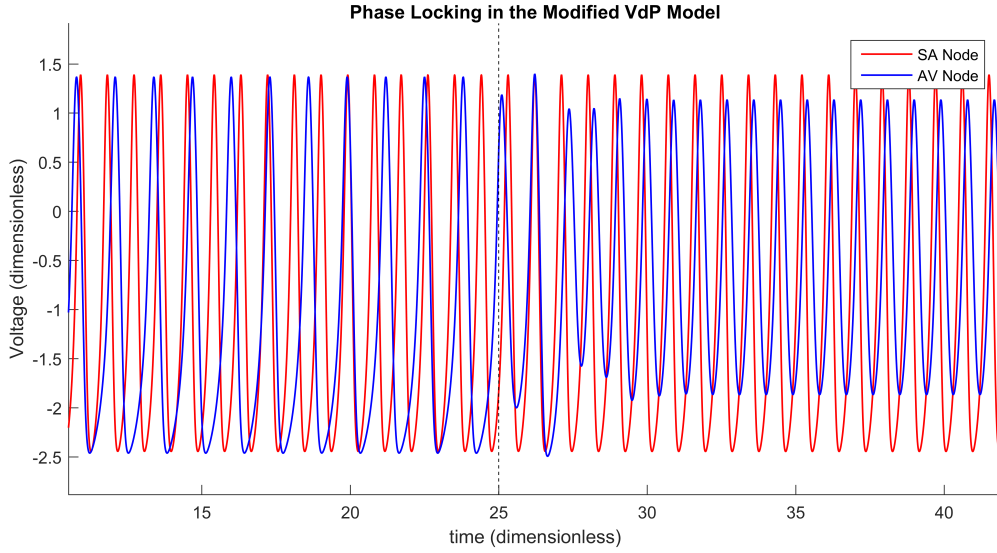
Figure 2.9: **Phase Locking in the Modified Van der Pol Oscillator.** Plots of the SAN and the AVN modelled by the Modified Van der Pol Oscillator. Phase locking behaviour is shown when the AVN is coupled to the SAN from $t = 25$.

Work regarding the coupling of Van der Pol pacemaker models and the FitzHugh-Nagumo model continues to add biological feasibility. In 2013, a one-dimensional cable of SAN cells modelled by the modified van der Pol Oscillator which divides into two separate cables of FitzHugh-Nagumo cells (representing the left and right atria) which then combine into another one-dimensional cable of modified van der Pol Oscillators (representing the AVN) was used to model the entire cardiac conduction system from the SAN to the AVN [86]. A slow pathway or delay along one path can cause a functional conduction block, which in turn creates re-entrant waves originating from the AVN and propagating back towards the SAN, a pathological condition known as Atrioventricular Nodal Reentrant Tachycardia (AVNRT). However, the rapid heartbeat symptomatic of

41

AVNRT is not reproduced. The diffusely coupled grid from [98] provides a more physiologically accurate description of cardiac tissue during AVNRT using the same model on a 100 x 100 grid of FitzHugh-Nagumo oscillators to represent the atrial tissue, with 10 x 10 squares of Modified Van der Pol oscillators in opposite corners representing the SAN and AVN. Slow and fast pathways around an obstacle created AVNRT and alternans dynamics. This is among the most computationally light methods in the literature to describe the atrium in as much depth as two-dimensional wave propagation fronts, and results were also repeated with the more accurate Fenton-Karma model [78], which will be discussed in more detail in section 2.4.

The Aliev-Panfilov model is a 1996 development of the FitzHugh-Nagumo model to address the issues of hyperpolarisation and APD restitution [100], although the independent variable is still dimensionless and the parameters are not physiological.

Model 2.4 *Aliev-Panfilov Model for Cardiac Excitation*

$$\dot{u} = ku(1 - u)(u - a) - uv$$
$$\dot{v} = \epsilon(u)(ku - v)$$

(2.6)

where $\epsilon(u)$ is a step function: $\epsilon(u < a) = 1$ and $\epsilon(u > a) = 0.1$

In this model, a is the threshold for excitation and the parameter k controls the magnitude of the transmembrane current. Parameters we obtained for the model by fitting the APD restitution curve to experimental data. The model is capable of producing spiral waves (2D) and scroll waves (3D) and is ideal for rapid computation of cardiac excitation on a detailed mesh, while retaining a computation time similar to the FitzHugh-Nagumo model. It is unclear why the Ailev-Panfilov model was not used by the groups studying the modified van der Pol, as this would have eliminated any possibility of the dynamics on the atrium and AVN junction being an artefact of FitzHugh-Nagumo hyperpolarisation.

The Aliev-Panfilov model is widely used in rapid simulation of cardiac dynamics, as the propagation patterns are much the same as the more complex biophysical models discussed in the next section. A quick time scale becomes especially important if multiple simulations are required for a range of parameters, making the Ailev-Panfilov model ideal for such investigations [108]. [109] study their dependence on parameter settings and thickness of the medium, finding that as the thickness of the medium increases, so does the complexity of the wave tip meander and the length of the scroll wave filament.

42

The Aliev-Panfilov model has featured prominently in many investigations into breaking up spiral waves with an external stimulus. The defibrillator most commonly used to eliminate fibrillation uses a very strong single electric shock, however, the levels of current can be damaging to cardiac tissue and are extremely painful [110], so it is desirable to reduce the necessary strength of current. Sakaguchi and Fujimoto find that a periodic force to the Aliev-Panfilov model with uniform frequency roughly equal to the frequency of the breathing [111], while Panfilov found that by using a feedback algorithm to drive a multiple shock protocol, only 20% of the current was needed to eliminate spatiotemporal chaos compared to using a single shock, although this number was higher (50%) for more realistic models [110]. Panfilov later studied the mechanisms by which a spiral wave breaks up into chaos, finding that a decreasing intercellular conductance can prevent breakup [112], a simulation result in accordance with common knowledge. Randomly distributed non-excitable cells are also inhibitive to the breakup of spiral waves in the Aliev-Panfilov model [61], which is consistent with the principles of CFAE described earlier, in which patches of tissue are ablated across the atria to prevent formation of spiral waves.

The main disadvantages of the Aliev-Panfilov model are also present in FitzHugh-Nagumo: the dimensionless time scale and the morphology of travelling waves. A dimensionless time scale makes it difficult to infer relevant temporal information, such as CV and firing rate, from the result. Furthermore, while the morphology of an AP is realistic, the morphology of the travelling wave in the spatial axis is not. Waves generated by the Aliev-Panfilov model are typically much thinner than those of a more realistic model, and generated spiral waves are much more robust: i.e. spiral wave breakup (tachycardia to fibrillation) is much more difficult to simulate in the Aliev-Panfilov model, and as spiral waves are formed by the interaction of two wavefronts, the wave morphology is critical to accurate simulation of this behaviour.

The work following the development of the Ailev-Panfilov model typically involves multiple simulations wave propagation on a biophysically accurate grid with a high spatial resolution, which is impossible to perform with a more detailed model. In contrast, the work following Grudzinski's modified van der Pol performs simulations in a context that would not be too difficult with a biophysical model and does not play to the strengths of such a phenomenological model.

2.5 Biophysical Cardiac Models

2.5.1 Key Examples

Biophysical models are the type of models inspired by the Noble model's approach [113] to developing a model of a cardiac cell by including all known biological components. This often leads to a large system of equations with a rich level of biological detail, in principle appropriate for simulation of the effects of various cardiac pathologies, pharmacological agents and invasive surgical procedures. These models are largely based on the ventricular AP, there are significantly fewer models for the sinoatrial, atrial and atrioventricular APs, as shown in Table 2.1.

Biophysical models aim to describe the mechanisms behind the generation of the cardiac AP in as much detail as possible. As more is learned about the heart through experimental investigation, biophysical cardiac models have become progressively more complex, and computationally intensive. Biophysical models are typically built by applying the Hodgkin-Huxley formalism to known ionic currents in the cell, and then the parameters approximated by fitting the resulting solution, or the time trace of functional parameters, to experimental data [96]. The voltage change over time is given by

$$dV/dt = 1/C_m(I_{\text{ion}} + I_{\text{stim}}),\tag{2.7}$$

where C_m is the membrane capacitance, I_{ion} is the sum of ionic currents, and I_{stim} are the external influences, either from neighbouring cells or an artificial stimulus. The dynamic Luo-Rudy model for the ventricular myocyte from 1994 [114] was a significant step forward for the biophysical modelling community and the first example resembling models in use today. The same equation is used to describe the rate of change of each ionic concentration, for any given ion B:

$$\frac{dB}{dt} = -\frac{(I_B \cdot A_{cap})}{V_C \cdot Z_B \cdot F},\tag{2.8}$$

where all undefined parameters are constants except I_B, which is the sum of all ionic currents carrying ion B. I_B is then given by the Hodgkin-Huxley equations for gated ion channels.

Cell Type	Model Class	Name	Variables	Constants	Algebraics	Citation
Pacemaker	Phenomenological	Van der Pol *	2	1	0	1926 [16]
		Grudzinski-Zebrowski*	2	5	0	2004 [2]
	Biophysical	Yanagihara	7	1	17	1979 [115]
		Noble 1984	15	48	44	1984 [116]
		Kurata	27	66	75	2002 [106]
		Sarai *	41	99	146	2003 [107]
		Maltsev	29	86	76	2009 [117]
		Inada	29	58	81	2009 [118]
Ventricular	Phenomenological	FitzHugh Nagumo *	2	4	0	1961 [14]
		Fenton-Karma *	3	12	8	1998 [78]
		Mitchell-Schaeffer *	2	5	3	2003 [8]
		BOCF *	4	20	10	2008 [119]
	Biophysical	Noble 1962	4	5	12	1962 [113]
		Beeler-Reuter	8	10	18	1977 [120]
		Luo-Rudy	8	24	25	1994 [114]
		Sakmann	20	69	60	2000 [121]
		Matsuoka	37	101	141	2003 [122]
		ten Tusscher 2004	17	46	67	2004 [123]
		Michailova	34	102	80	2005 [124]
		ten Tusscher 2006	19	53	70	2006 [125]
		Livshitz-Rudy	18	68	67	2007 [126]
		Mahajan	18	68	67	2008 [127]
		Stewart	20	52	76	2009 [128]
Atrial	Biophysical	Limblad	28	52	78	1996 [129]
		Nygren	29	51	49	1998 [130]
		Courtemanche *	21	49	75	1998 [4]

Table 2.1: **Summary of Mathematical Models for the Cardiac Action Potential.** A list of highly cited dynamic biophysical and phenomenological cardiac models, including the number of state variables, constant parameters, and algebraic parameters (those that depend on the state variables). Attributes of biophysical models were extracted from the CellML Model Repository [131], and the number of constants / algebraic parameters is likely to vary depending on the form of the model used. Models simulated in the thesis are marked with *.

The Luo-Rudy model featured twelve ion channels in a system of fifteen ordinary differential equations with a large number of parameters. The model has been modified to fit various other cardiac cell types, and expanded for extra detail, but remains a popular biophysical model in its original form. [96] cites sixteen different 'extension' models that have been developed using Luo-Rudy as a base. The model accurately reproduces the APD restitution curve of a cardiac myocyte, and as such has been responsible for various insights into how restitution affects cardiac electrophysiology and the mechanisms behind spiral wave generation [132].

The detail behind the Luo-Rudy model opened up many lines of theoretical investigation by varying the parameters in such a way that would require considerable time and effort to accomplish experimentally [133]. One example is the effect of heat on various cardiac diseases, as demonstrated by [134], who discovered that the ionic mechanisms of Brugada syndrome are a result of cell temperature.

The ten Tusscher-Noble-Noble-Panfilov (TNNP) model was a logical development from Luo-Rudy with insights from modern experimental evidence [135]. The model and its derivatives [125] are currently the most prominent cardiac models in the literature, and are capable of modelling epicardial, endocardial, and mid-myocardial cells by a change of parameter values.

Of most relevance to this thesis are biophysical models for the human *atrial* AP. The two most widely adopted by the present literature are both from 1998 and contain 12 ion channels: the 21 variable Courtemanche model [4] and the 29 variable Nygren model [130]. For work in future chapters, we use the Courtemanche model as a proxy for real data (much the way the Ten Tusscher model has been used in the past in the context of the ventricular AP [119]).

Model 2.5 *Courtemanche for Cardiac Excitation*

The Courtemanche model is given by Equation (2.7) *where*

$$
\begin{aligned}
I_{ion} =& I_{Na} + I_{K1} + I_{to} + I_{Kur} + I_{Kr} + I_{Ks} + I_{Ca,L} + \\
& I_{p,Ca} + I_{NaK} + I_{NaCa} + I_{b,Na} + I_{b,Ca}
\end{aligned}
\tag{2.9}
$$

The full model equations are given in Appendix A. The Courtemanche model has been responsible for the proposal of a theoretical anti-arrhythmic drug for the treatment of atrial fibrillation [11]. This 1999 study proposed a new set of parameters to model the

46

(a) Courtemanche Action Potentials

(b) Courtemanche Restitution Curves
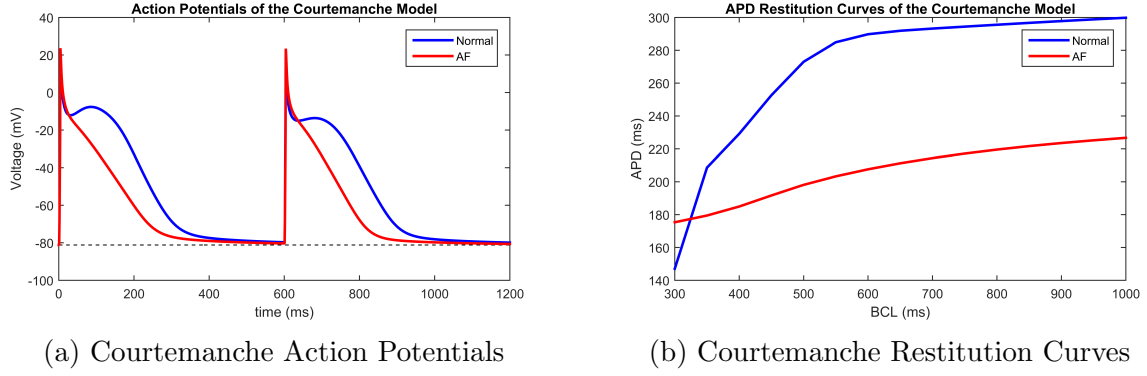
Figure 2.10: **Single Cell Courtemanche Model.** (a)Action Potentials of a single atrial cell, simulated by the Coutemanche model with a time step of 0.1 ms. Action potentials shown are a healthy atrial cell (blue) and the action potential of an atrial cell following AF-induced electrical remodelling. (b) The APD90 restitution curves of the cells in a, calculated at BCL lengths from 300 ms to 1 second in steps of 50 ms.

electrical remodelling process by reducing the currents I_{to}, I_{Kur} and $I_{Ca,L}$ by 50%, 50% and 70% respectively. These currents were thus cited as targets for a theoretical drug, an observation which matches subsequent experimental and clinical data [44, 48, 49].

Most relevant to our purposes (to study the applications of mathematical models with a view to therapeutic decision support during ablation therapy) the Courtemanche model has previously been used to simulate the effect of ablated lesions on the heart [10]. In this study, ablated lesions were set to points of zero conductance, and various ablation strategies were modelled in an attempt to make a comparison in effectiveness. However, during simulations, it was assumed that all lesions were completed successfully. Furthermore, spiral waves were initiated in the atrium using the Courtemanche 1998 model, which has not been adjusted to account for the effects of electrical remodelling. This has a huge impact on the morphology of the AP and APD restitution, as seen in Figure 2.10, which significantly affects the interactions of wavefronts occurring during a spiral wave.

In Figure 2.10 we show the AP and the APD90 restitution curve from the Courtemanche model with the 1998 original parameters and the 1999 fit for electrically remodelled cells. When electrical remodelling is considered, the dome following the spike disappears due to the reduction in the I_{to}, I_{Kur} and $I_{Ca,L}$ channels. When modelling heart tissue during AF treatment, during which fibrillation has already taken place, changes in morphology are liable to affect any simulated recordings, and changes in restitution are likely to affect spiral wave dynamics.

47

2.5.2   Limitations of Complex Models

While biophysical models are the most detailed and becoming more detailed all the time through adaptation to modern experimental data, they may not be the most suitable approach to address clinical challenges, where speed may be of the essence. Additional equations, especially additional dynamic variables, will inevitably cause an increase in computation time. Functional parameters (those that depend on the dynamic variables) will also add to the computation time, especially as the mathematical formulation of the functions becomes progressively more complex. Even with modern numerical techniques in place and today's level of computing power, simulating biophysical cardiac models on a biophysically relevant domain can take a huge amount of time. Modern research on biophysical models aims to speed up computation times by using state-of-the-art GPU parallelisation methods.

In 2011, using 16,384 cores in parallel, computation time on a realistic mesh took 240 times real time [136] using the TNNP model on a mesh, and a 2012 study from Nimmagadda reported speeds of 664 times real time to solve the model on a 256 x 256 x 256 grid [137]. Such figures are of course a ballpark estimate and depend on numerous factors: programming efficiency, language, numerical methods, and hardware. However, if the objective is for the model to be used as part of a therapeutic decision support system which can be simulated in real time alongside surgical treatment, computation must be feasible on a standard hospital computer. The same study from Nimmagadda reported 453 hours to simulate one second of data with the same protocol on a realistic mesh (1,630,800 times real time) on a high-end general purpose processor, and although this figure varies widely depending on the simulation protocol and domain (Okada et. al. reported 6 hours per cardiac cycle on a realistic mesh [138]), we are some way off being able to solve biophysical models on a meaningful domain in real time using standard hardware.

In Table 2.1 details are given for a range of cardiac models, with the type of cardiac cell that they model, and whether they are biophysical or phenomenological. 'Pacemaker' includes models of the atrioventricular and the sinoatrial nodes. Details of biophysical models were obtained from the exported Matlab code from CellML models in the CellML Repository [131] and may vary depending on the formulation, as algebraic parameters (those that depend on the state variables) can typically move inside the differential equations in which they are used. This is not an exhaustive list, but we believe it provides a good overview of electrophysiological models prevalent in the cardiac literature.

A further challenge lies in the number of model parameters. In the most detailed

models, the fast sodium current alone can be described by 9 state variables and 171 parameters [139, 140]. Eventually, a systematic exploration of the parameter space becomes impossible, and the results can become impossible to interpret. If a new set of parameters are obtained by a black box type fitting method (as is often the way these models are calibrated in the first place), how do we know these parameters are biologically relevant? In the words of John von Neumann, '*with four parameters I can fit an elephant, and with five I can make him wiggle his trunk*' [141, 142]. If one investigates how a specific parameter changes the solution, all we see is a cross section of a high dimensional parameter space. Another issue is the methodology behind the determination of the default parameter set; in some biophysical models, parameters have been fit to data collected many years prior [143], or by reusing model components, which may result in parameters for the same model being based on different cell types or even across different species [140].

Furthermore, biophysical models are difficult to study analytically. In Appendix A are the full model equations for the Courtemanche model. As it is impossible to change any of the parameters without in some way, directly or indirectly via the transmembrane voltage, without affecting every variable in the system, traditional analysis techniques (such as bifurcation theory) is ineffective. Even in the spaced clamped system, without diffusion, for which the system is a non-autonomous ODE, it is impossible to build an intuitive understanding of how the model behaves in its entirety. When diffusion is considered, the result is a PDE with many variables, and is even more difficult to approach analytically.

As the focus of this work is to develop tools that could be used in the operating theatre mid-surgery, biophysical models, especially of the modern level of complexity, are not appropriate. Instead, we consider the potential of phenomenological models, using the Courtemanche model as a proxy for real cellular AP.

2.6 Phenomenological Models

2.6.1 Fenton-Karma

The Fenton-Karma model dates back to 1998 and is the first phenomenological model of the cardiac AP that is at least based on the ion channels underlying the electrophysiological behaviour, and accurately reproduces a wide range of cardiac dynamics [78]. The Fenton-Karma model was built to provide a balance between detail and computational efficiency, ideal for studying cardiac wavefront propagation. The main advantages over

FitzHugh-Nagumo type models are that the wavefront propagation patterns more accurately reflect the behaviour of biophysical models, and the restitution properties when the model is forced at different BCLs. The model has been further reduced and extended by various authors, two prominent examples of which are described later in this section.

Model 2.6 *Fenton-Karma Model for Ventricular Myocytes*

$$\dot{u} = \nabla \cdot (\tilde{D}\nabla u) - (J_{fi} + J_{so} + J_{si})$$
$$\dot{v} = H(u_c - u)(1 - v)/\tau_v^- - H(u - u_c)v/\tau_v^+ \qquad (2.10)$$
$$\dot{w} = H(u_c - u)(1 - w)/\tau_w^- - H(u - u_c)w/\tau_w^+$$

where the phenomenological ionic currents are given by

$$J_{fi} = \frac{v}{\tau_d}H(u - u_c)(1 - u)(u - u_c)$$
$$J_{so} = \frac{u}{\tau_o}H(u_c - u) + \frac{1}{\tau_r}H(u - u_c) \qquad (2.11)$$
$$J_{si} = \frac{w}{2\tau_{si}}(1 + \tanh{[k(u - u_c^{si})]})$$

Without diffusion, the model is a three variable ODE with 12 parameters. The three variables consist of the transmembrane voltage u, and two gating variables, v and w. The ion channel modelling is simplified by considering categories of channels, rather than the individual channels themselves. Based on simplifying the models of Luo-Rudy [114] and Beeler-Reuter [120], the Fenton-Karma model contains three ion channels, J_{fi} (fast inwards), J_{so} (slow outwards), and J_{si} (slow inwards) currents. J_{fi} is a single current dependant on the gating variable v approximates the net contribution of sodium channels to the AP, although the actual underlying biophysics are significantly more complex than this in reality. In the same manner, J_{so} represents the potassium currents and depends only on voltage, while J_{si} models the calcium currents, gated by w. A fourth current, J_{ext} (or sometimes J_{stim}) is an external or stimulus current needed to force the cell to spike. In experimentation, J_{stim} can be a square wave used to push the voltage above a threshold and fire an AP. In a healthy mammalian heart, the stimulus is the AP propagating from the previous cell.

In the spatially extended model, much like the biophysical models, the Fenton-Karma model is a reaction-diffusion equation where $I_{ext} = \nabla \cdot (D\nabla u)$. The resulting travelling wave behaves a lot more similarly to the biophysical models than it does FitzHugh-Nagumo, and can produce a broader range of dynamics, notably the spiral wave breakup

to spatiotemporal chaos.
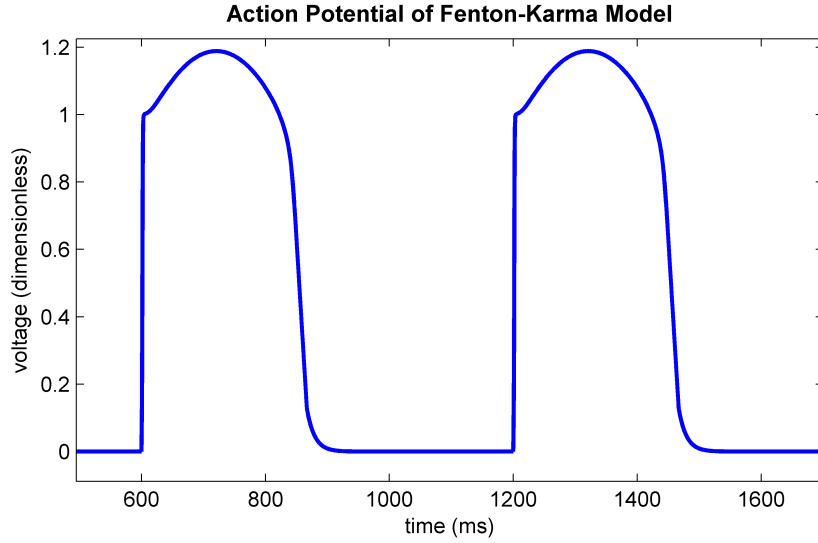
Figure 2.11: **Action Potentials of Fenton-Karma Model.** A plot of the action potential from the Fenton-Karma model, with parameters in [78]. The action potential is from a point model, paced at 600 ms.

It was demonstrated in the original paper that the model can be fit to a few different biophysical models, not only in terms of the AP morphology but also in terms of spiral wave generation, breakup, and wavetip meander. In the original paper, parameter sets were given for the model to reproduce the Beeler-Reuter, modified Beeler-Reuter, and a modified version of the Luo-Rudy model. Many more parameter sets have been derived in later papers, including parameter sets to distinguish the APs of epi/endo/mid-myocardial cells, as well as pathological conditions [144].

The decreased complexity of a phenomenological model allows for much quicker simulations. Because of this, a greater range of questions can be answered in a feasible time frame regarding the propagation of wavefronts through synthetic tissue. The Fenton-Karma model was responsible for demonstrating the effect that fibre rotation had on spiral wave generation in a three-dimensional parallelepipedal slab of tissue [78], a simulation that would have taken many weeks to compute with a biophysical model. Shortly after the proposal of the model, it was used to demonstrate various different mechanisms by which spiral waves in tissue can break up and cause fibrillation [144], and methods by which spiral wave break up could be controlled by a theoretical pacemaking device [145]. We present video simulations of the Fenton-Karma model displaying the break-up of spiral waves and persistent spatiotemporal chaos behaviour by a half-plane reset in `https://www.youtube.com/watch?v=87rYBkRJwl8` and by ectopic stimulation

51

in `https://www.youtube.com/watch?v=IKybSM8gD8s` (linked previously).

2.6.2 Mitchell-Schaeffer

The Mitchell-Schaeffer model is a 2003 reduction of the Fenton-Karma model, with the intention of creating a new cardiac model that was 1) similar to FitzHugh-Nagumo in terms of complexity and computation time, 2) understandable analytically without numerical methods, and 3) have an analytically calculable APD restitution curve as a function of the parameters [8]. The model, therefore, contains less biological detail than Fenton-Karma but is quicker to simulate (especially important for three-dimensional simulations) and analytical approaches are more insightful.

Model 2.7 *Mitchell-Schaeffer Model for Ventricular Myocytes*

$$\dot{v} = J_{in} + J_{out} + J_{stim}$$
$$\dot{h} = \begin{cases} \frac{1-h}{\tau_{open}} & \text{if } v < v_{gate} \\ \frac{-h}{\tau_{close}} & \text{if } v > v_{gate} \end{cases} \tag{2.12}$$

where the ionic currents are given by

$$J_{in} = \frac{hv^2(1-v)}{\tau_{in}}$$
$$J_{out} = -\frac{v}{\tau_{out}} \tag{2.13}$$

The Mitchell-Schaeffer model is the simplest model in the literature that provides a quantitatively accurate description of cardiac tissue, complete with a realistic APD restitution curve and travelling wave morphology facilitating realistic simulations of arrhythmic spiral waves on a reasonable timescale.

The reaction equations are handled by only two currents, an inwards and an outwards current, in addition to the stimulus. The inwards current is regulated by the gating variable h, and the outwards current is only affected by membrane potential v. This resembles the Fenton-Karma model with both inwards currents combined into one with a single gating variable. The model has only five parameters, a firing threshold v_{gate}, and four time constants; τ_{open} and τ_{close} regulate the opening and closing of the gate h, while τ_{in} and τ_{out} are time constants dictating the speed of the respective channels.

As the point model's solutions exist in a two-dimensional phase space, a nullcline analysis can provide a good graphical understanding of the solution. Rather than using
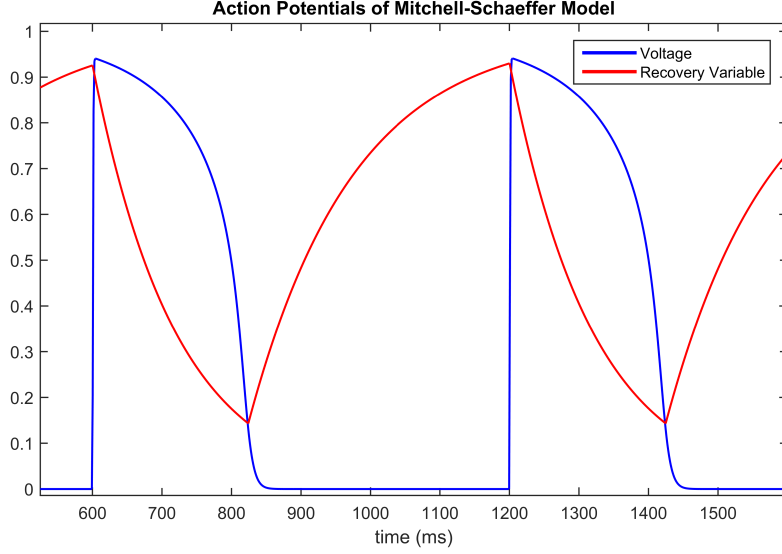
Figure 2.12: **Action Potentials from the Mitchell-Schaeffer Model.** Simulated action potentials obtained from solving the Mitchell-Schaeffer model with the parameter set from [8] and a basic cycle length of 600 ms.

the APD90, approximating the APD as the time until h reaches its minimum value provides an easy way of estimating the APD restitution analytically. This happens when $v = v_{gate}$, so rather than being above a 10% maximum depolarisation, the APD is defined as the fraction of the time v is above the firing threshold. As the equation for $h(t)$ can easily be solved analytically while $v > v_{gate}$, the maximum APD (assuming h starts from its maximum value of 1) is $APD_{max} = \tau_{close} \ln(1/h_{min})$, where h_{min} can be calculated from the $\dot{v} = 0$ nullcline as $h_{min} = 4\frac{\tau_{in}}{\tau_{close}}$. From there, knowing the basic cycle length BCL, it can easily be estimated how much h will grow during the diastolic interval DI the time the next stimulus hits by using the analytical solution for $h(t)$ while $v < v_{gate}$. Repeating the procedure for finding the APD gives the APD as a function f of the diastolic interval:

$$APD_2 \approx f(DI) = \tau_{close} \ln \left(\frac{1 - (1 - h_{min})e^{\frac{DI}{\tau_{open}}}}{h_{min}} \right) \tag{2.14}$$

which very closely predicts the APD restitution curve of numerical simulations. This provides a direct link between the parameters and the electrophysiology without even having to solve the model. Other quantities that can be calculated analytically are DI_{min}, the minimum required value of DI for which the call can fire an AP, and an error parameter $\epsilon = \tau_{out}/\tau_{close}$ that estimates the accuracy of the above calculations.

As each APD can be calculated in terms of the previous one, if one is only concerned with APD restitution, the ODE model can be reduced to a one dimensional map:

$$APD_{n+1} \approx \tau_{close} \ln \left(\frac{1 - (1 - h_{min})e^{\frac{BCL - APD_n}{\tau_{open}}}}{h_{min}} \right). \qquad (2.15)$$
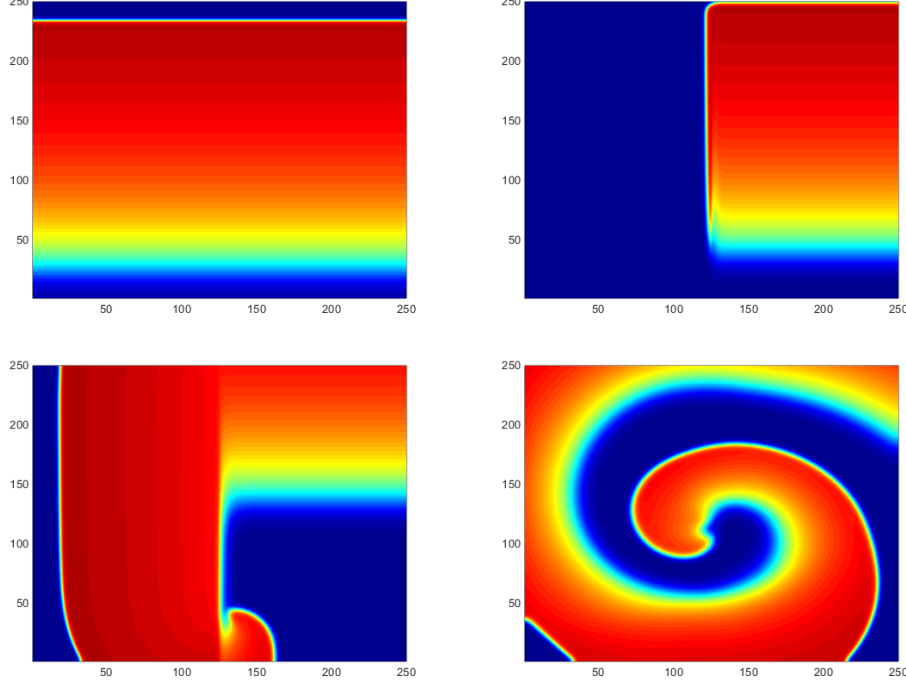
Figure 2.13: **Spiral Waves in the Mitchell-Schaeffer Model.** 4 heat maps of a) a plane travelling wave, b) immediately after the half plane reset c) as the spiral begins to form and d) a fully formed spiral wave. Red corresponds to regions of high Voltage, blue to low Voltage.

This map can be analysed further with classic bifurcation theory. It is possible to divide the parameter space into regions of differing qualitative behaviour based on how the 1:1 solution loses stability upon reduction of BCL. For some region of the parameter space, the map can, via a pitchfork bifurcation, exhibit stable alternans behaviour, an alternation between APs of long and short APD.

In comparison with Aliev-Panfilov, the Mitchell-Schaeffer model is more accurate and adjusting specific parameters allows greater control of the result, but does require a step size 10 times as small to maintain stability [146]. In practice, the Mitchell-Schaeffer model is most commonly used where a model of the body surface ECG based on cardiac wave propagation is the desired result [18, 147], as solving electrical conduction on the torso can be very complex, a simpler cardiac model is preferred. The Mitchell-Schaeffer model provides a way to model realistic activation patterns but without microscopic detail unnecessary for this purpose.
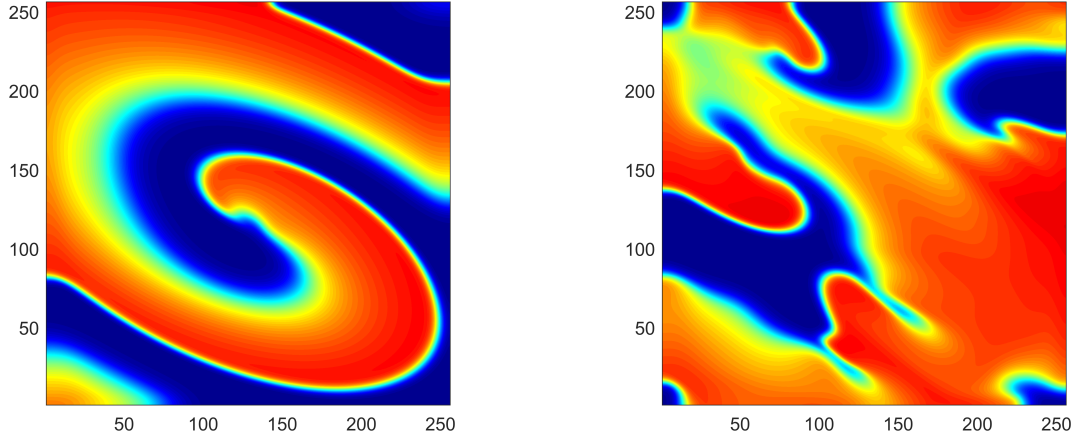
(a) Anisotropic Stable Spiral Wave

(b) Anisotropic Stable Spiral Wave Breakup

Figure 2.14: **Anisotropic Spiral Waves and Breakup.** a) A stable spiral wave with a ratio of anisotropy of 4:1, with dominant angle $\pi/6$ off the horizontal. b) A spiral wave with the same diffusion properties, but parameters on the intracellular dynamics that results in spiral wave breakup (fibrillation). Red corresponds to regions of high Voltage.

Simulations of spiral waves in the Mitchell-Schaeffer model are given in Figure 2.13, performed on a 256 x 256 grid, with stimulation across the bottom edge of the domain. A wavebreak is initiated by a half-plane reset, which causes propagation in the retrograde direction down the left-hand side. This results in re-entry, as this wavefront returns to a place it has already been. This behaviour continues, forming a stable spiral wave. With a change of parameters, this wave can be caused to break up into spatiotemporal chaos. The effect of raising τ_{close}, lengthening the AP, is shown in `https://www.youtube.com/watch?v=JOJ3ryFtMBw`.

In Figure 2.14 we show a simulation using anisotropic diffusion. In this simulation, I chose diffusion coefficients at $D_{\parallel} = 3$, $D_{\perp} = 0.75$, $\alpha = \pi/6$ to demonstrate anisotropy. Applying Equation (2.1), this gives us a diffusion tensor of

$$\mathbf{D} = \begin{pmatrix} 1.3125 & -0.9743 \\ -0.9743 & 2.4375 \end{pmatrix}.$$

The spiral waves in these plots are strongly elliptical rather than circular as in previous simulations. In a real heart, the dominant conduction direction corresponds to the fibre orientation in the heart muscle. A video of the entire simulation, in which a plane wave is broken by a half plane reset to create an anisotropic spiral wave, which breaks up into smaller spirals before eventually terminating, can be found in `https://www.youtube.`

`com/watch?v=Hplmg-rP-qo`. The spiral waves destroy themselves when all cores veer too close to the boundaries. In a human heart, fibrillation can be permanent, in which the fibrillatory dynamics are stable or paroxysmal, in which episodes of fibrillation self-terminate, however the mechanisms behind this distinction remain a mystery.

2.6.3 Bueno-Orovio Cherry Fenton

The Bueno-Orovio Cherry Fenton model (BOCF) is a 2008 extension of the Fenton Karma model [119]. The BOCF model adds an extra variable to Fenton Karma that aims to provide an accurate and complete description of the cardiac AP with the smallest amount of complexity. In comparison to the Fenton-Karma model, the BOCF model is more detailed with a longer computation time (although not orders of magnitude higher). The extra detail allows greater control of the AP morphology, most notably the spike and dome morphology, not possible with the Fenton-Karma model, although the lack of real ionic currents means the model is still unsuitable for applications such as drug study [148].

Model 2.8 *Bueno-Orovio Cherry Fenton Model for Ventricular Myocytes*

$$
\begin{aligned}
\dot{u} &= \nabla \cdot (\tilde{D}\nabla u) - (J_{fi} + J_{so} + J_{si}) \\
\dot{v} &= [1 - H(u - \theta_v)](v_\infty - v)/\tau_v^- - H(u - \theta_v)v/\tau_v \\
\dot{w} &= [1 - H(u - \theta_w)](w_\infty - w)/\tau_w^- - H(u - \theta_w)w/\tau_w \\
\dot{s} &= ((1 + \tanh[k_s(u - u_s)])/2 - s)/\tau_s
\end{aligned}
\tag{2.16}
$$

where the ionic currents are given by

$$
\begin{aligned}
J_{fi} &= -vH(u - \theta_v)(u - \theta_v)(u_u - u) \\
J_{so} &= (u - u_o)(1 - H(u - \theta_w))/\tau_o + H(u - \theta_w)/\tau_{so} \\
J_{si} &= -H(u - \theta_w)ws/\tau_{si}
\end{aligned}
\tag{2.17}
$$

and other functional parameters can be found in [119].

Here u represents the transmembrane voltage, J_{fi}, J_{so} and J_{si} are phenomenological summations of the fast inward, slow outward, and slow inward currents respectively. J_{fi} is effectively gated by the gating variable v, J_{so} is voltage gated, and J_{si} is effectively gated by the product of the gating variables w and s. D_{BOCF} is either a spatially dependant diffusion constant (under the assumption of isotropic diffusion), or a diffusion tensor (under the assumption of anisotropic diffusion). We always take initial conditions at the resting state, where $[u(0), v(0), w(0), s(0)] = [0, 1, 1, 0]$. A full description of this

model can be found in [119].
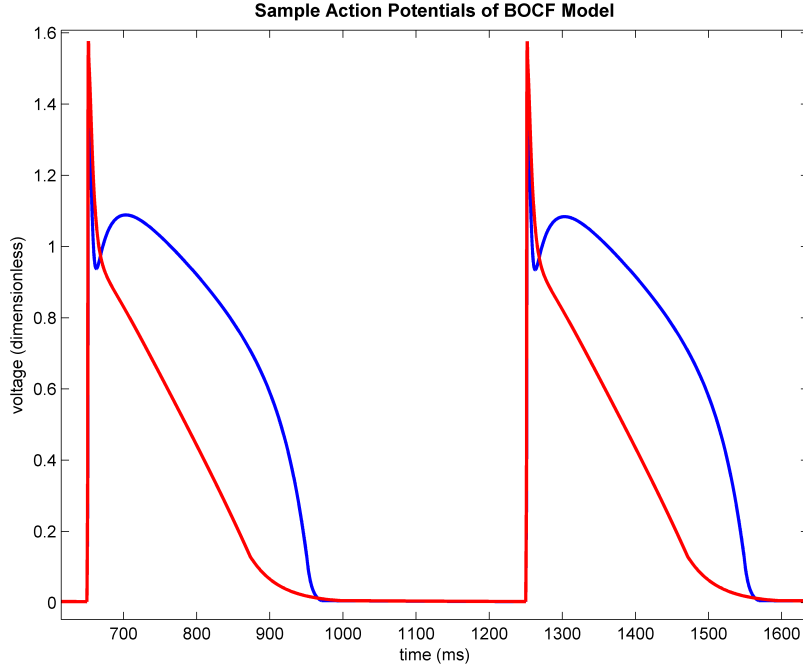
Figure 2.15: **Action Potentials from the BOCF Model.** Action Potentials simulated using two separate parameter sets. In blue is the parameter set from [119], optimised for the ventricular action potential. In red is a parameter fit to [11] for AF remodelled atrial cells. The fit is explained in detail in chapter 3.

The model has been validated by comprehensive fitting to both experimental data and biophysical ventricular models, most notably the TNNP model [135], and the models of Priebe Beuckelmann [149] and Iyer Mazhari Winslow [150] for both the point and the spatially extended form of the model. A list of references for the experimental data used in the development of the Bueno-Orovio Cherry Fenton model can be found in section 2.1 of [119]. The parameters were fit to ensure resting membrane potential, threshold for excitation, upstroke, AP morphology, APD and CV rate dependence all matched the relevant experimental data, for which 5 different parameter sets are given in the paper, for epi/endo/midmyocardial cells, and to fit to the TNNP, Priebe-Beuckelmann, and Iyer-Mazhari-Winslow models. The ratio in computational timescales between BOCF, Priebe-Beuckelmann, TNNP and Iyer-Mazhari-Winslow is 1:31:50:8084 respectively, and a 512x512 grid can take as little as 2 to 5 times real time to compute using a GPU based implementation [151].
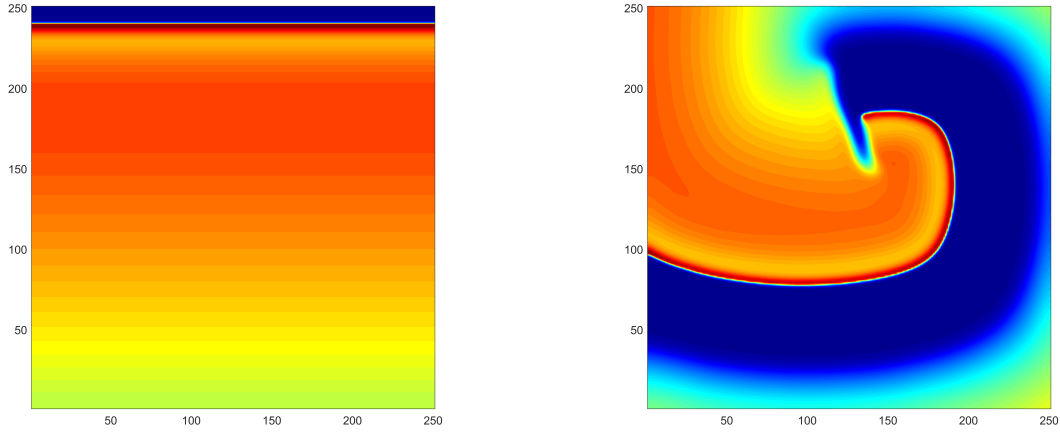
(a) Plane Wave from BOCF Model   (b) Spiral Wave from BOCF Model

Figure 2.16: **Spiral Waves in the BOCF Model.** (a) A plane travelling wave initiated from stimulating the bottom edge of the domain (b) 5 seconds after initiating a wavebreak, the solution stabilises to a spiral wave. As before, red indicates high voltage. Compared to the wavefronts in the Mitchell-Schaeffer model, the BOCF contains a band of yellow shortly after the wavefront due to the spike and dome morphology.

The Bueno-Orovio Cherry Fenton model reproduces key characteristics of biophysical models in tissue simulation as well as a point model, even when spiral waves are generated [152]. The Bueno-Orovio Cherry Fenton model provides us with a good balance of realism, reproducing key features quantitatively, and not having a computation time inhibitive to running multiple simulations. For this reason, it should be ideal for studying the effects of conduction blocks, such as those caused by radiofrequency ablation, and the greater control of AP morphology over the Fenton-Karma model increases likelihood of being able to successfully adapt the model to reproduce the effects of atrial electrical remodelling.

We present a simulation of this in Figure 2.15, which shows simulations using the default parameter set (in blue), which models a healthy ventricular cell and a parameter fit to the AP of an atrial cell following electrical remodelling as a result of AF by using the Courtemanche model with the 1999 parameter set [11] to generate synthetic data (in red). We explain this parameter fit in much more detail in the following chapter, it is shown here for descriptive purposes only. In Figure 2.16 we show the model in a two-dimensional sheet of tissue, in both a plane travelling wave and a spiral wave after initiating a wavebreak. A video of the spiral wave simulation can be found at `https://www.youtube.com/watch?v=-XAt4QgQWug`.

In the following chapter, we investigate the parameter space of the BOCF model in more detail using single and multi-objective optimisation techniques to determine parameter sets corresponding to health and disease, and also to investigate the important parameters along this transition.

Chapter 3

Parameter Optimisation in Cardiac Wave Propagation

3.1 Introduction

3.1.1 Background to Problem

In this thesis I am interested in the applications of mathematical modelling in terms of AF and associated clinical practice, however, the phenomenological models introduced in chapter 2 are all designed to model the ventricles. This is done primarily by fitting parameters to match the solutions of the more complex biophysical ventricular models described in chapter 2, or by fitting to real data. In this chapter, we optimise the parameters of the Bueno-Orovio Cherry Fenton (BOCF) [119] model to produce relevant APs for a model of the atrial tissue in relation to both healthy and diseased states. Secondly, we use multi-objective optimisation techniques to find the key parameters underlying this transformation.

To maximise relevance to AF, we wish to model the atrial AP following AF-induced electrical remodelling. Electrical remodelling, as described in chapter 2.2, is an electrophysiological change at the cellular level that facilitates the sustenance of functional re-entrant waves in the atria through a shortening of the APD. The shorter AP allows for a larger number of excitation fronts to coexist, causing episodes of AF to last for longer.

Although there is a lack of phenomenological models available for the atrial AP, there do exist biophysical models such as the Nygren model [130] and the Courtemanche model [4] discussed in the literature review and given in Appendix A. The Courtemanche model is particularly useful for providing a proxy for real data as it has already been optimised

to model the electrical remodelling process by mimicking the experimentally measured reductions in the ionic currents I_{to}, I_{Kur} and $I_{Ca,L}$ by 50%, 50% and 70% respectively [11]. Although the modification was performed in 1999, predictions made were subsequently verified by experimental data in 2012 [48, 49] and 2015 [44].

3.1.2 Motivation

Many techniques exist for fitting a model solution, $x(t)$ to data, $y(t)$. These methods typically involve formulating the problem as an optimisation function to minimise. The most intuitive optimisation function is the root of the mean of the squared errors at each time point t in the simulation (the Root-Mean-Squared error, or RMS). There are numerous methods available for solving the problem of finding the minimum of a function of n parameters, including the Nelder-Mead Simplex Search (NMSS), Genetic Algorithms (GAs), and Particle Swarm Optimisation (PSO).

These methods are often sufficient for fitting a model to data (either synthetic or experimental) for a single cell model. However, as we are performing this fit with a view to using the resulting calibrated parameters to model travelling waves on the pulmonary vein, we require a fit to the *propagating* AP. This increases the complexity of the problem as we now require both the speed and the morphology of the emerging AP to match the data. While for all other parameters held constant, CV is proportional to the diffusion constant D, effective CV is also influenced by the AP morphology, most importantly the upstroke velocity. A sharp upstroke velocity causes the difference in the intracellular voltage between neighbouring cells to grow faster. This increases the value of the diffusion *term* and causes the next cell to spike faster, thus a smaller value of the diffusion *constant* is required to maintain the same CV. In short, any derived diffusion constant D is only valid for a specific set of parameters. Further, including diffusion multiplies the computation time of each iteration by the number of nodes used in the simulation, increasing the requirement for fast convergence.

For this problem, a potential difficulty arises in fitting the AP by minimisation of the RMS error $E = \Sigma((x(t) - y(t))^2)/N$ due to the temporal translation induced by varying D. Formally, we define the objective function $E_{\text{RMS}}(\mathbf{p})$ for the RMS error between an AP $x_i(\mathbf{p})$ from the BOCF model generated by a parameter set $\mathbf{p}$ and a target action potential y_i, each consisting of N time points i, to be:

$$E_{\text{RMS}}(\mathbf{p}) = \sqrt{\frac{\sum_{i=1}^{N}(x_i(\mathbf{p}) - y_i)^2}{N}} \qquad (3.1)$$

61

As the wave speed varies depending on all 21 parameters, it is possible, in theory, for a set of parameter values for the cell model that generates an AP with perfect morphology to spike at a different time to the data. For such a case, the objective function $E_{\mathrm{RMS}}(\mathbf{p})$ would return a large error. The sharp upstroke exacerbates this problem, as even a small difference in spike time will result in values of t such that $x(t) = 0$ and $y(t) = 1$.

Firstly, this chapter investigates methods by which we can improve the fit by finding a more suitable combination of objective function and fitting method than $E_{\mathrm{RMS}}(\mathbf{p})$ minimised by NMSS. We investigate whether we can obtain a better fit (or the same fit with fewer function evaluations) over the RMS error by using the cross-correlation as an objective function, a method which focuses purely on the morphology and is independent of spike time.

To ensure that the results obtained are not simply an artefact of the NMSS, we verify results by using a single objective GA. This also allows us to be able to compare the efficiency of these two different parameter optimisation methods. All optimisations using both the cross-correlation and the mean squared error will be performed using the NMSS and a genetic algorithm.

These fitting methods optimise only the AP morphology to a single target AP. The second purpose of this chapter is to investigate the use of multi-objective optimisation algorithms to fit not only to the electrically remodelled AP but also map the pathway through parameter space between the two. This could help to obtain more information about the transition between health and disease.

The two questions we aim to answer in this chapter are as follows:

1. Does maximising the cross-correlation provide a better fit for the AP morphology than minimising the root mean squared error?

2. Can multi-objective optimisation algorithms help us to better understand the key parameter changes that model the transition between health and disease?

3.2   Methods

3.2.1   Data Generation and Numerical Algorithms

Synthetic data were generated from simulating the Courtemanche model using a spatial resolution $\Delta x = 0.2$ mm and a temporal resolution of $\Delta t = 0.01$ ms on a one-dimensional

cable of length 2 cm (100 nodes) with a BCL of 600 ms. We simulate two APs by an S1-S2 stimulation protocol in all cases and use only the second one for error calculation to account for restitution properties at this BCL. 600 ms was chosen as the BCL to match the pacing used clinically at the Bristol Heart Institute.

To estimate the value of D for the Courtemanche model, we fit the model to match the clinically observed CV (48 cm/s [153]). To do this we calculated the time elapsed between the 20th and 80th APs in the model (to avoid influence from the stimulus and boundary conditions) using the beginning of the upstroke as a reference point which can be easily and reliably identified, and ensured this corresponded to a CV of 48 cm/s. As the wave speed depends monotonically on D while all other parameters are held constant, optimisation of D can be performed using any basic root finding method. We found a value of $D = 2.615$ calculated through simple interval bisection. At the opposite end to the stimulus, we use Neumann boundary conditions, minimising the effect that the boundaries have on nearby nodes. The red line of Figure 3.1 shows the target AP.

3.2.2 Parameter Fitting Methods for Uniobjective Optimisation Problems

We consider the initial parameter set from the sample fitting code provided in appendix 3 of [119] to be our *nominal parameters* (the initial parameter set) and denote this $\mathbf{p}_0$. However, this code fits to the point model, and as such only contains the 20 parameters for the AP morphology and does not contain a value of D. To estimate a nominal parameter value for D, we used the same technique used to optimise D for the Courtemanche model. The AP generated by $\mathbf{p}_0$ is shown by the blue curve in Figure 3.1.

NMSS [154] is a simple search algorithm for a problem of n continuous inputs, which given an initial point $\mathbf{p}_0$, first creates an initial simplex of $n + 1$ points. We create the initial simplex from $\mathbf{p}_0$ by creating an additional point by a 5% increase along each of the 21 dimensions of the parameter space. To edge towards the minimum, most iterations of NMSS perform a reflection, in which the point on the simplex with the highest function is translated through the centre of the simplex. If this new point is better than the original, we continue reflection, if not, the simplex contracts on to the local minimum. NMSS will stop if a local minimum is detected, therefore if the function has many local minima, the result will be highly dependent on the initial point and unlikely to find the global minimum. To perform this computation, MATLAB's 'FMINSEARCH' function was used.
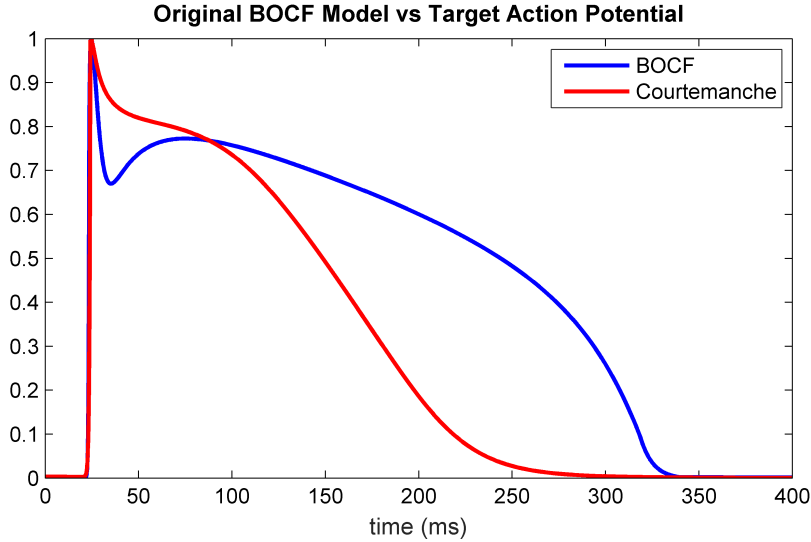
Figure 3.1: **Propagating Action Potentials from Courtemanche and BOCF.** The Courtemanche model factoring in atrial remodelling (red) is the target data. The blue curve is the default parameter set for the BOCF model with only the diffusion constant calibrated so the AP morphologies can be better compared. Simulations were performed on a string of 100 cells stimulated at one end, with the AP displayed on the 80th cell. The APs have an RMS error of 0.2494 and a Cross-correlation Error of 0.1119.

Rather than using one initial point, the GA starts from a population of initial points in parameter space. For each parameter, we use an initial range one order of magnitude either side of $\mathbf{p}_0$. The members of the population with the best fitness value are selected as parents for the next generation. From these, three types of children are created. The best of the parents survive to the next generation as *elite children*. *Crossover children* are created by combining parameters of two parents. Finally, *mutation children* are a random perturbation to a single parent. For single objective optimisation, each generation consists of 200 members, of which 10 are elite, 160 crossovers and the remaining 30 are mutation children. The evolution terminates (indicating convergence) when the relative change in the best member of the population over a number of generations falls below a tolerance. For single objective optimisation, we use 50 generations and a function tolerance of 10^{-6}, meaning the algorithm will continue until the optimal fit across the 50 previous generations has varied below 10^{-6}. MATLAB's 'GA' function was used for all of our genetic algorithm fits.

PSO is not used in this thesis but we include a description here for completeness. PSO [155] is a category of population based meta-heuristics which use random points flying through the parameter space, each updating its velocity based on the performance history of itself and its neighbours. An increased number of particles reduces the probability of

falling in a local minimum, however, the method can converge slowly for some problems [156]. Hybrid methods which attempt to apply the best of both have been developed for the optimisation of the BOCF model to the TNNP Model [157], however, this study is limited in depth, and comparisons between the hybrid method and the existing methods are not performed.

3.2.3 Objective Functions

RMS Error

Calculation of the RMS error is not trivial for a travelling wave, as we wish to avoid artefacts of the simulation protocol from incurring additional error. Factors such as response to the stimulus and influence of boundary conditions are not relevant if we only require a fit for how the AP propagates through tissue.

After simulation, we cut off the first 20 and the last 20 cells. The APs on all cells are shifted in the time axis so that cell 21 (the first cell remaining in the simulation) begins spiking at time $t = 0$. The objective function $E_{\mathrm{RMS}}(\mathbf{p})$ was evaluated on the 80th cell. To ensure a low error, the delay in the AP from the 21st cell to the 80th must match in both models, which effectively constrains the wave speed. If the wave speed is incorrect, then the RMS error will be high regardless of how well the morphology fits.

Cross-correlation

The alternative we propose to minimising the RMS error (an objective function that implicitly requires an accurate CV to provide an accurate measure of goodness of fit) is to fit the morphology separately to the CV, i.e. fitting D separately to the other parameters. The morphology must be fit first, as the influence of the morphology over the wave speed is much greater than the influence of the wave speed over the morphology. Specifically, the parameters responsible for the upstroke velocity have the most influence over the wave speed. This is because a sharper upstroke results in the voltage differential from one cell to the next to become larger at an increased rate, which proportionally increases the conduction velocity (therefore requiring a lower diffusion term). During the morphology fitting step, the wave speed should not have any influence over the error, and so we require an objective function independent of the timing of the AP.

The cross-correlation is ideal for this purpose. The cross-correlation provides the similarity between two discrete signals x and y of N sampling points, where y is lagged by a value τ. This function $(x \star y)(\tau)$ is defined as

$$(x \star y)(\tau) \ = \sum_{m=1}^{N} x(m) \ y(m + \tau).$$

The cross-correlation function will be at its maximum for the value of τ, τ_{max} which maximises the correlation between $x(t)$ and $y(t - \tau)$. The degree of similarity between two signals is given by $(x \star y)(\tau_{\text{max}})$.

The autocorrelation is defined as the cross-correlation of a signal with itself, i.e. $(x \star x)(\tau)$, which will have a maximum at $\tau = 0$. Dividing the cross-correlation by the maximum value of the autocorrelations $(x \star x)$ and $(y \star y)$ normalises the cross-correlation, ensuring that if there is a lag such that there is a perfect fit $(x(t) = y(t - \tau) \forall t < N)$, the result will be 1. Our objective function $E_{\text{cross}}(\mathbf{p})$ for the cross-correlation fit is then,

$$E_{\text{cross}}(\mathbf{p}) = 1 - \frac{\max((x(\mathbf{p}) \star y)(\tau))}{\sqrt{(x(\mathbf{p}) \star x(\mathbf{p}))(0) \cdot (y \star y)(0)}}, \tag{3.2}$$

where as with $E_{\text{RMS}}(\mathbf{p})$, $\mathbf{p}$ is the set of parameters and $x(\mathbf{p})$ is the simulated data using the parameters $\mathbf{p}$. $E_{\text{cross}}(\mathbf{p})$ will give a result of 0 if there is a perfect fit, and 1 for a worst possible case. Minimising this function gives us the parameter values for which the AP morphology of the model most closely matches that of the data independent of the wave speed. We note that minimising this function is the equivalent to maximising the cross-correlation. The wave speed from cell 20 to 80 can then be fit independently using a separate objective function varying only D as described previously when we estimated D for the Courtemanche model.

3.2.4 Multi-Objective Optimisation

Multiple objective optimisation is performed using the Non-dominated Sorting Genetic Algorithm II (NSGA-II) algorithm [158], as implemented by Matlab's 'GAMULTIOBJ' function. The goal of this algorithm is to use an evolutionary process to obtain a Pareto front. For any multi objective optimisation problem with p_m inputs and E_n objectives to minimise, a set of parameters $\mathbf{p}$ is defined as *Pareto optimal* or Non-dominated if it is impossible to reduce the value of one objective function without increasing another. The result of our fit is therefore not a single parameter set, but a front of Pareto optimal solutions.

The NSGA-II Algorithm works much the same way as the GA described earlier, using elite, mutation and crossover children. However, a much greater fraction of elite children must be preserved or too much of the Pareto front will be lost during each generation.

As such we follow the commonly accepted rule of thumb of taking best 35% of the population as elite children. The termination criteria is based not on the best member of the population, but on the relative change in the area behind the front across 100 generations.
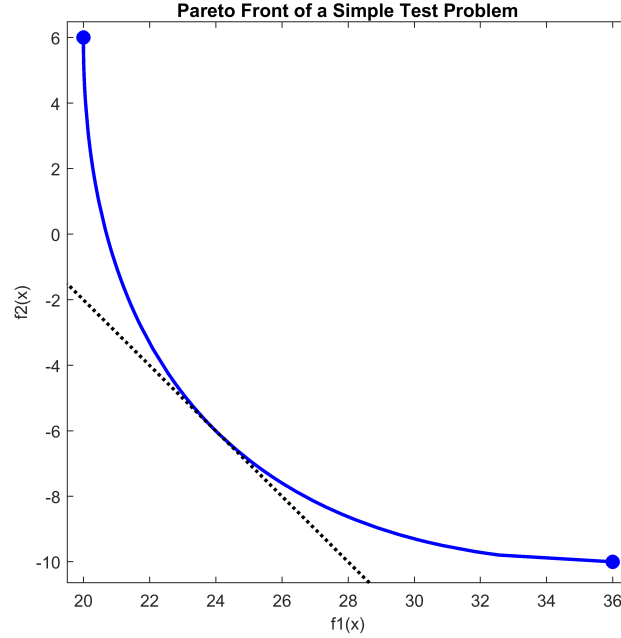
Figure 3.2: **A Sample Pareto Front.** This front displays the Pareto optimal solutions from the simple test problem $f_1(x) = (x-2)^2 + 20$, $f_2(x) = (x+2)^2 - 10$. The ends of the Pareto front correspond to the optimal parameters for the single objective problems. A line $f_2 = -f_1 + c$ runs tangential to the front and the intersection denotes one possible optimal for optimising both objectives.

Firstly, to demonstrate the method, we consider a simple problem with only one parameter for which the global optimum for both objective functions is known. Consider the two functions

$$
\begin{aligned}
f_1(x) &= (x-2)^2 + 20 \\
f_2(x) &= (x+2)^2 - 10.
\end{aligned}
\tag{3.3}
$$

Trivially, $f_1(x)$ has a minimum value of 20 for $x = 2$ and $f_2(x)$ has a minimum value of -10 for $x = -2$. In Figure 3.2 we show the Pareto Front obtained by application of the NSGA-II algorithm with an initial parameter range from $x = -10$ to $x = 10$. The plotted points at either end of the front are the result of optimising f_1 and f_2 independently, and therefore correspond to values $x = -2$ and $x = 2$. In order to determine which value on the front contains the best balance between the two objectives, a straight line can be

drawn either of the forms $f_2 = -f_1 + c$, or connecting the two ends of the front, which can then be translated to the minimum value of c for which the line is tangential to the front. Alternative methods for determining a particular optimum are Euclidean distance to the origin, or some problem-dependent weighting to prioritise more important objectives.

Due to the symmetry in this trivial problem, both ends of the front lie on a line $f_2 = -f_1 + c$. Translating this line to the point where it is tangential to the front gives $f_2 = -f_1 + 18$ which touches the front at (24,6) given by the parameter $x = 0$ (half way between the two local minima). The high degree of symmetry in this problem comes from both objective functions being identical translated quadratics, and cannot be assumed true for the error of a mathematical model.

3.2.5 Pathways through Parameter Space from Health to Disease

We apply this optimisation technique to map a pathway though parameter space that describes how the AP is deformed by AF-induced electrical remodelling. Again, we use the Courtemanche model as a proxy for real AP data, this time using the original 1998 model to represent a healthy AP and the 1999 parameter set including relevant ionic current reductions for a post-AF cell as before. To allow a greater focus on the intracellular dynamics responsible for the change in AP morphology, the section of this chapter concerned with multi-objective fits and pathways through parameter space is performed on single cells.

As the change in the Courtemanche model comes from varying only 3 parameters, we can also estimate intermediate states as required. We define the 'degree of remodelling' R to be 0 for a healthy AP and 1 for the remodelled parameter set. Only APs for $R = 0$ and $R = 1$ are known to the genetic algorithm, but it is worth noting at this time that intermediate APs can be calibrated for validation purposes. We assume that this transition between Courtemanche parameter sets is a linear path from the $R = 0$ set to the $R = 1$ set.

We perform a novel parameter fit in order to map this pathway. We use the NSGA-II algorithm to simultaneously train parameters to fit both the healthy ($R = 0$) and the electrically remodelled ($R = 1$) APs, such that $f_1(\mathbf{p})$ is quality of fit for $R = 0$ and $f_2(\mathbf{p})$ is the quality of fit for $R = 1$. This will allow the calculation of the Pareto front, where one end of the front corresponds to the optimal fit to the healthy cell, and the other end

to the electrically remodelled cell. As one traverses along this front, the AP will deform from the healthy state to the remodelled state.

If the front is sufficiently smooth, the morphology of the AP and the values of the parameters should also smoothly vary along the front. If the Pareto front does describe the transition, then the deformation of the morphology along the front in the BOCF model should match the deformation of the morphology of the Courtemanche model as we vary R from 0 to 1. We can identify key parameters underpinning this AP change by analysing how parameters vary along the front.

3.3 Results

3.3.1 Cross-correlation Minimisation

Firstly, we demonstrate a potential advantage of using the Cross-correlation as a function to fit the morphology of a travelling AP and how this can give an error function more representative of what we are actually trying to fit. This is demonstrated by AP from a parameter set $\mathbf{p}_{slow}$ plotted in Figure 3.3. $\mathbf{p}_{slow}$ has been deliberately chosen to reflect well the AP morphology but with a diffusion constant much too small.
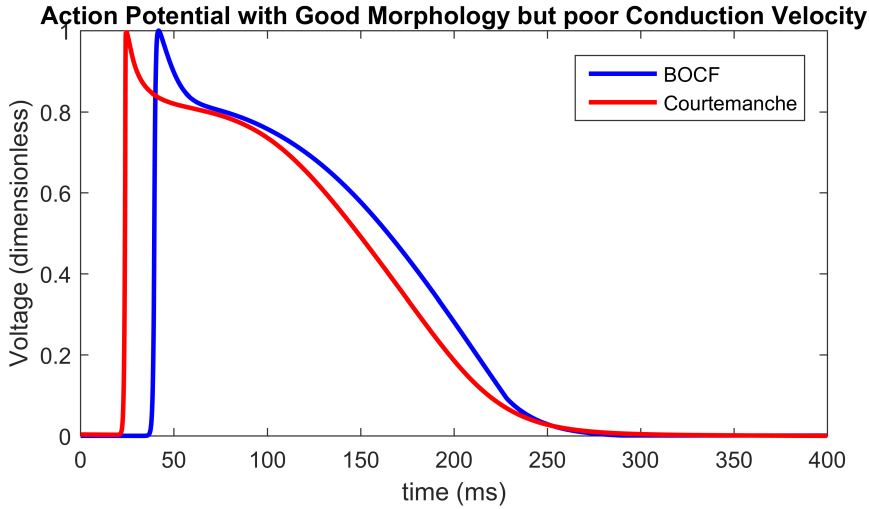
Figure 3.3: **Action Potential with Good Morphology but Poor Conduction Velocity.** A target action potential (red) and a simulated action potential (blue) generated from a parameter set designed to give a good action potential morphology but slow conduction velocity. As a result, the root mean squared error is high, and the parameter set scores poorly, due to one bad parameter value out of 21 parameters.

It is clear to the eye that the morphology of the AP (blue) for $\mathbf{p}_{slow}$ is very close

Method	Objective Function	Evaluations	Root MSE	X-Correlation
None	None	1	0.2495	0.1109
Nelder-Mead	Cross-correlation	3546	0.0389	6.9216×10^{-4}
Nelder-Mead	RMS error	2578	0.0157	6.3866×10^{-4}
Genetic Algorithm	Cross-correlation	23600	0.0344	4.0263×10^{-4}
Genetic Algorithm	RMS error	118400	0.0138	5.7596×10^{-4}

Table 3.1: **Results from Single-Objective Optimisation.** Table showing error in calibrating the BOCF model to the Courtemanche model with two different fitting methods and two different objective functions. Function Evaluations is used to represent speed of fit. The RMS error out-performs the Cross-correlation in every metric for the NMSS. The Genetic Algorithm performed slower but better in every case. Simulations from the Genetic Algorithm are shown in Figure 3.4.

to the target data (red), but shifted slightly to the right because of a slow diffusion speed. As a result, at approximately $y = 25$, the Courtemanche model has reached its peak, but the stimulus has yet to arrive at the 80th cell in the BOCF model, resulting in an error of 1 (the highest error possible). This is a significant source of error when using the RMS error as the objective function. This parameter set has a RMS error of $E_{\text{RMS}}(\mathbf{p_{slow}}) = 0.1819$, which is a marginal improvement over $\mathbf{p}_0$ (0.2494). Using the Cross-correlation, this parameter set has an error of $E_{\text{cross}}(\mathbf{p_{slow}}) = 5.8143 \times 10^{-4}$, which is a massive improvement on the Cross-correlation for $\mathbf{p}_0$ (0.1119). These results show that by using the cross-correlation as an error function, it is possible to isolate error incurred from a poor morphology from the error incurred from a poor CV and that there are regions of parameter space (near p_{slow}) for which this is more representative of the error.

Next, we test how well the two error functions actually perform when used in an optimisation algorithm, using both a genetic algorithm and the NMSS. We present a comparison of the two objective functions numerically in Table 3.1, evaluating the error from both objective functions using both parameter sets, as well as the number of function evaluations used to perform the fit.

The results show that while maximising the cross-correlation *does* calibrate the model parameters to fit the data, there is no clear benefit over minimising the RMS error. It is a curious result that minimising the RMS error resulted in a lower value of $E_{\text{cross}}(\mathbf{p})$ than simply minimising $E_{\text{cross}}(\mathbf{p})$ directly. As this only holds for the NMSS method, it is reasonable to assume that there are many local minima for $E_{\text{cross}}(\mathbf{p})$. For the NMSS, the RMS error performed better in terms of number of function evaluations (2500 to 3500),

| (a) Root Mean Squared Error | (b) Cross-correlation |
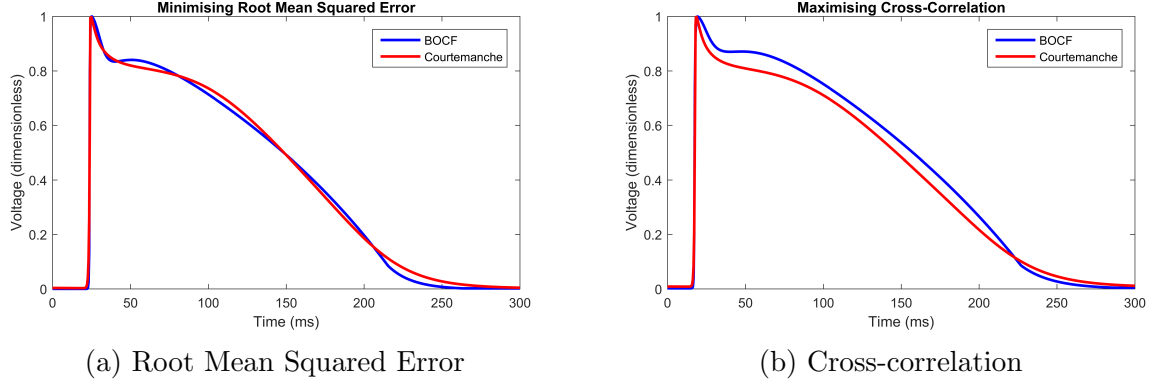
Figure 3.4: **Genetic Algorithm Optimisation of BOCF Model.** Attempts to fit the BOCF model to the target data using the RMS error and the cross-correlation as objective functions. Both fits used a population bound by an order of magnitude above and below the set in [119], and optimisation was performed using the Genetic Algorithm.

which is directly proportional to the evaluation time to perform the fit.

Using the GA, using $E_{\mathrm{cross}}(\mathbf{p})$ as an objective function worked much better than with NMSS. However, there is still no clear advantage to use $E_{\mathrm{cross}}(\mathbf{p})$. The fit derived from using $E_{\mathrm{RMS}}(\mathbf{p})$ follows the remodelled atrial AP much better, as seen in Figure 3.4.

The superiority of the RMS error for performing the parameter fit indicates that the region of parameter space for which the cross-correlation was a notable improvement (the parameters with a good morphology but poor speed) was not visited by the genetic algorithm or the NMSS. The best fit, from observation of the plots in Figure 3.4, is clearly obtained from minimising RMS error, and the parameter set from this fit will be used in future work in modelling the pulmonary vein electrophysiology.

3.3.2 Multi-Objective Optimisation

In this section, we present the results of using the NSGA-II algorithm to optimise simultaneously to the healthy and remodelled APs. Due to the poor performance of the cross-correlation as an objective function, multi-objective optimisation was performed using the RMS error, so $f_1(\mathbf{p})$ and $f_2(\mathbf{p})$ are the RMS error in the healthy and diseased cells respectively.

126 generations were required after the initial population was evaluated, totalling 254000 runs of the objective functions. Evolution was terminated when the convergence criterion was satisfied, that the average relative change in the area behind the Pareto

front (calculated with respect to a reference point given by the maximum values of each objective function on the previous generation's front) across 100 consecutive generations dropped below a tolerance. As 35% of the population are preserved as elite children, of the 2000 members of the population, 700 were Pareto optimal when the algorithm and these form the Pareto front. The remaining 1300 lie a short distance behind the front.
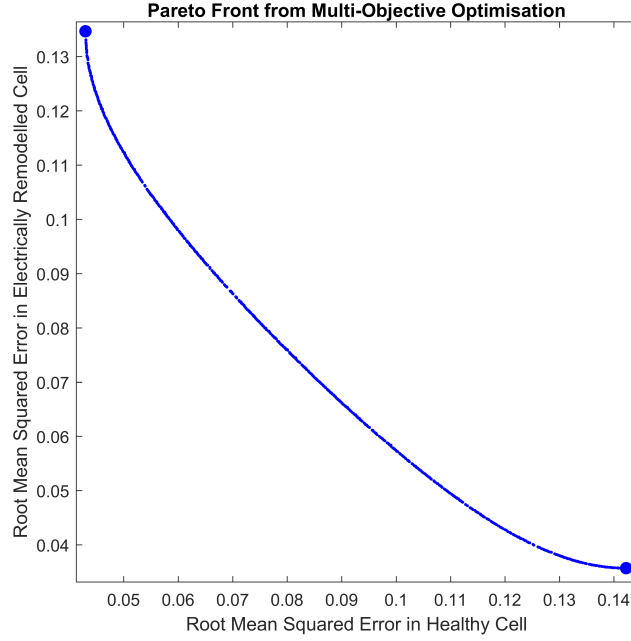
Figure 3.5: **Pareto Front from Multi-Objective Optimisation of BOCF Model to Healthy and Diseased States.** This figure displays the Pareto Front of 700 points obtained from simultaneously fitting the BOCF model to the healthy and the diseased atrial action potentials. The smoothness of the curve indicates that parameter values deform smoothly across the front.

We display the 700 individuals in the Pareto front in Figure 3.5. The top-left point in the front (0.0430, 0.1346) marks the optimal fit for the healthy AP. As one travels across the front, the AP is deformed towards the electrically remodelled state. The bottom right point, situated at (0.1422, 0.0357) marks the optimal fit for the AP following electrical remodelling. The line $f_1(\mathbf{p}) = f_2(\mathbf{p})$ is not drawn as we are computing the Pareto front to find the pathway from one state to another, rather than to find a balanced optimal solution.

A fragmented front with large discontinuities would indicate large jumps across parameter space, where the set of Pareto optimal solutions actually contains many different

fronts. The smooth, continuous nature of our solution indicates that the whole front does generally correspond to the same region of parameter space and that the AP does indeed deform smoothly across the front.
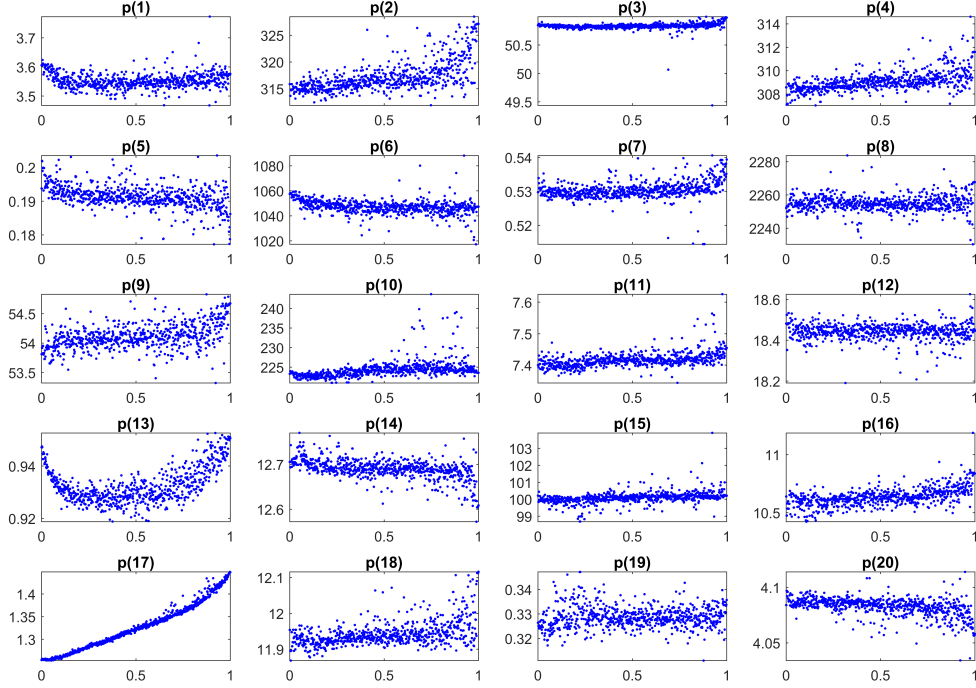
Figure 3.6: **Parameter Changes along the Pareto Front.** Scatter plots showing how all 20 parameters change along the front, with the degree of remodelling on the x axis and parameter value on the y axis. Each point in the plot represents one of the 700 parameter sets on the front. $\mathbf{p}(17)$ stands out as a clearly important parameter change due to the strong correlation between parameter value and position along the front.

In Figure 3.6 we include scatterplots of all 20 parameters in the model along the front. The parameter set which optimises the fit to the healthy cell is composed of the first data points in each of the 20 plots. This plot contains valuable information about how the parameters affect the solution. As we know consecutive points in the front give a minimal change in AP morphology, a high variance implies that the model is not sensitive to parameter changes (a variety of parameter sets could potentially give the same solution).

We note that the vast majority of the parameters appear to have little correlation with the position on the front, with the exception of the weak nonlinear response in $\mathbf{p}(13)$ (u_{so}, a phenomenological constant in the time constant of the slow outwards current) and the strong correlation in $\mathbf{p}(17)$ (u_s, a phenomenological constant in s, the gating variable

Parameter	Correlation	Relative Change	Parameter	Correlation	Relative Change
1	-0.0107	-0.1226 %	11	0.4666	0.6239 %
2	0.6281	3.3249 %	12	-0.0673	0.0084 %
3	0.1110	0.2920 %	13	0.4136	2.4485 %
4	0.5820	1.4052 %	14	-0.5197	-1.1899 %
5	-0.4499	-3.3741 %	15	0.3899	0.8455 %
6	-0.3341	-0.7858 %	16	0.5691	6.4857 %
7	0.3093	0.8276 %	**17**	**0.9835**	**13.3751 %**
8	0.0676	-1.1345 %	18	0.4891	0.1360 %
9	0.4779	1.7900 %	19	0.0404	-0.4118 %
10	0.4242	0.2937 %	20	-0.4772	-0.4456 %

Table 3.2: **Parameter Value Significance and Relative Change** The Correlation columns show correlation between parameter values and position along the front. Only parameter 17 has a significant correlation at 0.9835, the next strongest correlation is 0.62 on parameter 2. Relative change gives the percentage change in the parameter from the healthy to the diseased state. Again parameter 17 stands out, as its value at $R = 1$ was 13.37% higher than at $R = 0$. The next largest magnitude absolute change is parameter 16, at 6.48%

for the slow inwards current). The exact values of the Pearson correlation coefficients are given in Table 3.2 and provide further evidence for the increase of $\mathbf{p}(17)$ as the key parameter change in the transition between healthy and remodelled APs. The locations of these parameters in the BOCF model is given in Equation (3.4) where show a subset of the equations of the full model, with u_{so} and u_s highlighted in bold.

$$
\begin{aligned}
\dot{u} &= \nabla \cdot (\tilde{D}\nabla u) - (J_{fi} + J_{so} + J_{si}) \\
\dot{s} &= ((1 + \tanh[k_s(u - \mathbf{u_s})])/2 - s)/\tau_s \\
J_{si} &= -H(u - \theta_w)ws/\tau_{si} \\
J_{so} &= (u - u_o)(1 - H(u - \theta_w))/\tau_o + H(u - \theta_w)/\tau_{so} \\
\tau_{so} &= \tau_{so1} + (\tau_{so2} - \tau_{so1})(1 + \tanh[k_{so}(u - \mathbf{u_{so}})])/2;
\end{aligned}
\tag{3.4}
$$

$\mathbf{p}(17)$ is the phenomenological constant u_s inside the tanh function of the equation for the gating variable s. An increase of u_s will shift the $\tanh[k_s(u - u_s)]$ function to the right (seen in Figure 3.7), lowering $\dot{s}$. s is a phenomenological gating variable which has a resting state at 0 and turns positive during an AP, so a decrease in $\dot{s}$ will lower the value of s throughout the AP. Any decrease in the value of s will also decrease the absolute value of the phenomenological slow inwards current approximation J_{si}.

The parameter change will have a stronger effect while $\tanh[k_s(u - u_s)]$ is close to
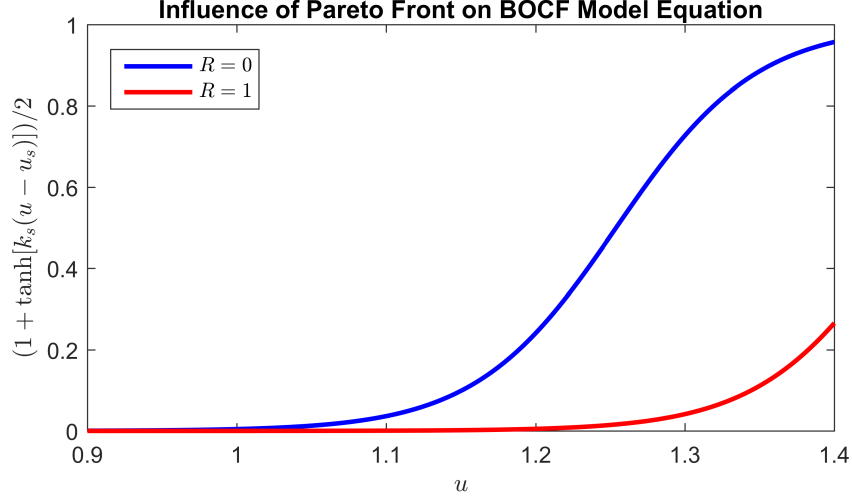
Figure 3.7: **Influence of Pareto Front on BOCF Model Equation.** Plot showing $(1 + \tanh[k_s(u - u_s)])/2$ in terms of u for the healthy action potential (blue) and the remodelled action potential (red), showing the interval of u for which the parameter change is important.

0 (while $u \approx u_s$). Although all plots of the APs in this thesis are normalised to allow better visual comparison across models, u ranges from 0.9 to 1.3868 for $R = 0$ and from 0 to 1.3916 for $R = 1$. We plot the values of $(1 + \tanh[k_s(u - u_s)])/2$ for values of u from 0 to 1.4 in Figure 3.7, holding k_s ($\mathbf{p}(16)$) constant at the mean value on the front (10.6337). This plot helps to visualise the interval of u for which our identified changes in the parameter u_s has the biggest influence on the equations of the BOCF model (when u is large).

As there are 3 ion channels in the BOCF model and 13 in the Courtemanchce model, u_s and u_{so} have no direct counterpart in the Courtemanche model. However, the ion channels reduced to create the synthetic data, in accordance with experimental evidence, were the slow outwards channels: I_{to} (transient outwards) and I_{Kur} (ultra-rapid delayed rectifier), and the slow inwards channel $I_{Ca,L}$ (Calcium leak). It is known that *the reduction in $I_{Ca,L}$ alone can account for most of the morphological features* associated with AF-induced remodelling [11]. These morphological features mostly refer to the reduced APD and size of the dome (the secondary spike in the AP following the initial peak), allowing more wavefronts to coexist, and making spiral waves more likely to form. The parameter change obtained from our parameter fit also functions to reduce the strength of the slow inwards current, which reduces the APD and size of the dome, in accordance with the findings above.

75

3.3.3 Pathways Through Parameter Space

In this section, we provide a more sophisticated error analysis to investigate how well the parameter change across the Pareto front, most importantly the change in u_s, approximates the actual transition in the biophysical model. We calculate error along the front for 100 equally spaced values of R from 0 to 1. As only $R = 1$ and $R = 0$ were used in the creation of the Pareto Front, if the intermediate parameter sets along the front do not accurately represent the intermediate APs, we can expect to see a large error far from the ends. Firstly, we present results simply from using 100 parameter sets equidistant along the front. The result is shown in Figure 3.8.
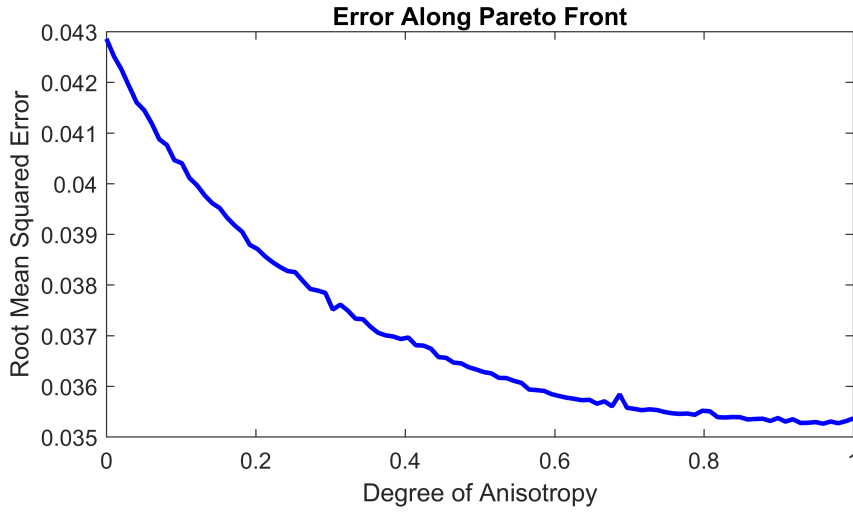
Figure 3.8: **Errors in Intermediate Action Potentials.** Graph showing the change in error through the pathway from health to disease. There is no additional source of error in the intermediate values.

We note that the end points of this curve are constrained by the optimal fits for the healthy and remodelled APs. The decrease is simply an artefact of the model fitting better to the remodelled AP due to its simpler morphology. The important result is the largely monotonic change from one state to the other. There is no clear additional source of error incurred for the intermediate values of R, implying that APs were reproduced well along the front. However, this is only one possible way we can evaluate error along our parameter fit, and there are many alternative ways to traverse the front:

1. As before, use the raw values from the parameter sets on the Pareto front, including every oscillation in all 20 parameters (original front).

2. Use values of u_s on the Pareto front and assume everything else is held constant at the mean value (reduced front).

3. Fit a linear function through the values of u_s and hold the others constant (linear fit).

4. Fit a quadratic function through the values of u_s and hold the others constant (quadratic fit).

5. Fit a quadratic function through the values of u_s and of u_{so} and hold the others constant (two parameter quadratic fit).

6. Ignore the intermediate front altogether and linearly interpolate all 20 parameters from one end to the other (end to end interpolation).

The reduced front will tell us how important u_s is compared to the other parameters. The polynomial fits give an equation for how parameters vary across the front, which can tell us more about the underlying dynamics. The end to end interpolation would be the intuitive way of estimating parameter change without using the multi-objective GA, and comparing error along this path with the others tells us how important calculation of the Pareto front is.

Figure 3.9 shows the error from all pathways previously described. The end to end interpolation (in black) shows the error from simply linearly changing all parameters from one end of the front to the other. The poor quality of fit for this approximation shows that using only the ends of the front (as would be calculated if both objectives were optimised independently) is an insufficient method to capture the smooth deformation of the AP between states and highlights the importance of the multi-objective technique.

The red curve shows the error as only u_s is varied along the front and the others are held at the mean value. This has a largely similar morphology to the original front (in blue) which is evidence of a change in u_s being able to map the transition. However, the reduced front contains numerous upwards spikes (notably on 0.69, and between 0.85 and 0.9). This is a result of certain points on the Pareto front lying in different regions of parameter space, which can be verified by the points in the plot for $\mathbf{p}(17)$ in Figure 3.6 which do not lie on the linear trend. In the original front, this is accounted for by a change in the 19 other parameters for the same point on the front, resulting in increased error when the mean value is taken.

This sensitivity to location on the front can be smoothed by fitting polynomials (linear in yellow, quadratic in purple) through the change in u_s. As u_{so} also has a notable

77
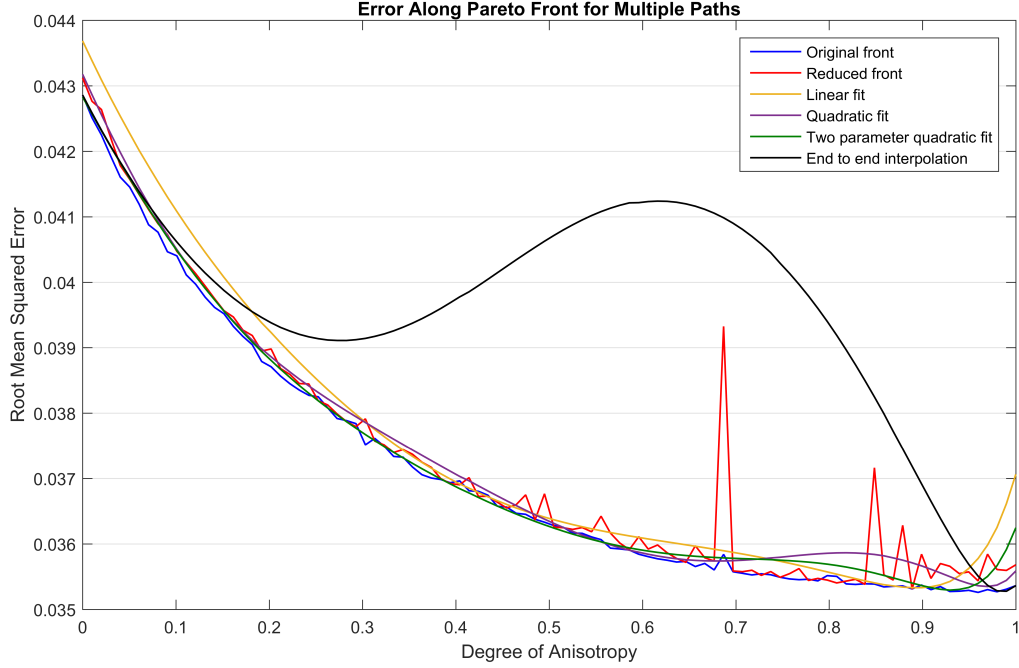
Figure 3.9: **Error Along Pareto Front for Multiple Paths.** Graph showing the change in error through the pathway from health to disease for multiple approximations of the Pareto Front. All curves feature a similar morphology, with the exception of the end to end interpolation, the only curve which does not use intermediate values along the front. This is an important result, as it demonstrates the importance of considering the entire front.

nonlinear trend, we also fit quadratics through u_{so} (in green).

As these paths through parameter space are simply polynomials in one or two dimensions, the error is much smoother than the numerical parameter sets on the Pareto front and allow for calculation of an AP at any point on the pathway. As can be seen from the linear fit (gold line) linear regression through the parameter space gives a good overall shape but has the highest error on the end points. This is to be expected when using a linear function to approximate a curve which is not perfectly linear.

It is difficult to infer any more details from the graph, so mean errors are given in Table 3.3 for comparison. This table has been ordered in increasing error. The best fit was from using all of the information from the original front. The next best fit was from approximating two parameters with a quadratic function. Taking only one parameter into account resulted in a higher error, with the quadratic fit performing batter than the reduced front and the linear fit. The worst fit was from ignoring the front and

Path	Error
Original Front	3.7120×10^{-2}
Two Parameter Quadratic Fit	3.7218×10^{-2}
Quadratic Fit	3.7303×10^{-2}
Reduced Front	3.7310×10^{-2}
Linear Fit	3.7448×10^{-2}
End to End Interpolation	3.9666×10^{-2}

Table 3.3: **Total Error Along Front** Table showing the error along the entire front. Results show the more of the front is taken into account, the lower the error.

interpolating end-to-end. Results essentially show us that the more of the front we take into account, the better the fit is across the transition.

3.4 Discussion

This chapter aimed to explore the potential of parameter fitting methods to firstly adapt a phenomenological model designed for the ventricles to model the atrial AP, and secondly, use multi-objective optimisation techniques to characterise the pathway from healthy to diseased states. Firstly, we investigated whether the cross-correlation was a better objective function than the RMS error for fitting the morphology and CV of a propagating AP.

The results show that the two are connected in that parameter values that scored well on one objective function also performed well on the other. However, while the results show that the cross-correlation is a good *measure* of fit in certain regions of parameter space, it is not efficient as an objective function. For the NMSS, minimising RMS error resulted in a lower value for the cross-correlation than minimising the cross-correlation did, and the cross-correlation offered no clear advantage when a GA was used.

Our results also allow us to also make comparisons between NMSS and the GA. We see that for single objective optimisation, the genetic algorithm provided a minor increase in quality of fit at the cost of a huge increase in number of function evaluations, although different metaparameters (convergence criteria, population size, etc.) are likely to have an effect on this. The choice of optimisation algorithm should, therefore, be chosen based on the application, and whether optimising the AP model on a case specific basis is required. The parameter fit obtained from minimising the RMS error will be used in our future work on modelling of the pulmonary vein electrophysiology.

We are mostly limited by the lack of real human data to serve as a target AP for the BOCF model. However, using the Courtemanche model as a proxy for real data, we were able to ensure that the model and 'data' were both stimulated with an identical stimulation protocol on identical cables of tissue. Further, there are many different methods available for global optimisation which could have been used to provide further testing of the objective functions, such as simulated annealing, statistical emulation and particle swarm optimisation.

Our second main result in this chapter comes from investigating the potential of a multi-objective genetic algorithm to determine pathways through parameter space, connecting states corresponding to health and disease. As a result, we could reduce the transition from two disconnected points in 20-dimensional phase space to a simple polynomial in one or two dimensions.

We identified the phenomenological constant u_s, was the most important parameter in mapping the transition between healthy and diseased states. We also demonstrated that identification of this parameter, responsible for changes to the slow inwards current, is consistent with experimental evidence.

We found that using the Pareto front for this purpose provided a much better representation of the AP deformation than assuming a linear connection between the two points. The use of a Pareto front for this purpose is a novel idea, and one which we feel is potentially applicable to mapping smooth transitions through parameter space in other mathematical modelling applications, e.g. [159]. These results were obtained from a single cell to focus on the intracellular dynamics.

As in the previous section, we are limited by a lack of real data, in this case along the transition. We approximated the pathway in the Courtemanche model by a linear function and found a nonlinear change in the BOCF model parameters. In truth, of the three currents affected by the remodelling process, some may be reduced quicker than others. We cannot claim that the parameter path obtained for the BOCF model maps the true physiological transition. We claim only that it maps the transformation obtained from a linear path in the Courtemanche model much better than the more intuitive approach of assuming a linear path in the BOCF model.

Further, we acknowledge that there is no well grounded theory to explain why the Pareto front well approximates the intermediate values in the transition. Findings appear

positive for the sample problem in this chapter, but it is unclear how well this method would apply to other problems and would be an interesting topic for future work. At this time, we can only speculate that this approach would work well in a range of problems where a nonlinear change in parameters of one model is required to reproduce the response to a linear input.

Chapter 4

Modelling of Pulmonary Vein Recordings

4.1 Introduction

4.1.1 Background

This chapter introduces a new model capable of producing synthetic pulmonary vein recordings of the type in Figure 4.1, recorded during the process of circumferential pulmonary vein isolation (CPVI)[1,2]. We recall from the literature review that AF is often initiated by an ectopic signal from the pulmonary veins and that the prevailing method of treatment is to isolate the vein from the atrium by forming a continuous lesion around the base, and that there are various strategies available to do this.

CPVI is a minimally invasive surgical technique for treatment of AF, in which a circular lesion is formed surrounding the pulmonary vein via the application of radiofrequency energy, electrically isolating the left atrium from the pulmonary vein and so preventing the propagation of an action potential (AP) in or out of the myocardial sleeve. Whilst the initial success rate of pulmonary vein isolation is approximately 85% [67], recurrence rates 5 months after ablation therapy can be as high as 30% in paroxysmal AF patients

---

[1]The work presented in this chapter has been reported in the following publication: Green HD, Thomas G, Terry JR. (2017) Signal Reconstruction of Pulmonary Vein Recordings Using a Phenomenological Mathematical Model: Application to Pulmonary Vein Isolation Therapy, Frontiers in Physiology volume 8 (496), DOI:10.3389/fphys.2017.00496. For this publication the contributions were as follows: HG and JT provided concept; designed and executed the study; analyzed and interpreted the data. GT provided data; performed analysis of clinical and reconstructed signals. All authors wrote and approved the final manuscript.

[2]Further, the techniques have been published in the following patent application: Terry JR, Green HD. (2017) Detection of conduction gaps in a pulmonary vein, WO Patent App. PCT/GB2016/053,421

or 78% in permanent AF patients [53]. It is desirable to ensure that the ablation process is completed as quickly as possible, as the duration of the procedure is known to strongly correlate with the rate of recurrence [160]. Additionally, ablation of the pulmonary veins carries a risk of pulmonary vein stenosis [71] and if complete electrical isolation is not achieved, the lesions can become pro-arrhythmic through the creation of conduction obstacles that facilitate the initiation of reentrant waves.
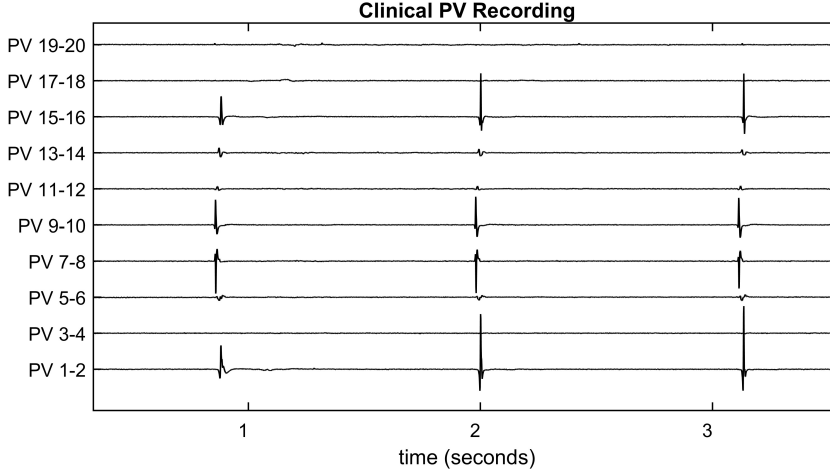
Figure 4.1: **Clinical Pulmonary Vein Recording.** The pulmonary vein recording of a patient with atrial fibrillation during pulmonary vein isolation therapy. Spiking indicates electrical activity as the action potential propagates through the recording catheter. Since the pulmonary vein is not a perfect cylinder, not all electrodes make a good contact. For example, Channels 3-4, 17-18, and 19-20 show no spiking activity for this reason. These are referred to as missing channels throughout the thesis.

Often the initial circular lesion made during CPVI are incomplete and small conduction gaps can remain. These are most commonly due to poor depth penetration of the lesion and the ablation catheter not maintaining a continuous contact with the heart tissue. To provide a guide to the surgeon as to the location of the conduction gaps, bipolar recordings of electrical activity around the pulmonary vein are taken using a lasso catheter typically consisting of 10 or 20 electrodes (see Fig. 4.1 for an exemplary time-trace). The conduction gap is assumed to correspond to the location of the electrode(s) where the first spikes are observed and these sites are targeted for further ablation [40, 69]. However, as the pulmonary vein is not a perfect cylinder it is common for some electrodes to make poor contact with the tissue. Figure 4.1 is an example of this happening in clinic, and in this case, it is difficult to infer the activation pattern across PV 17-18 and 19-20. If these missing channels correspond to the region of first activation, this information loss could potentially lead to ablating the wrong region, or concluding the process has been

successful.

In this chapter, we focus on developing a mathematical representation of the phenomenology of the electrical signal recorded from the lasso catheter and to use this to reconstruct missing electrical signals. This is in contrast to typical approaches to modelling the cardiac AP or the body surface ECG where physiologically detailed models are typically used (see, for example, [15, 96] for comprehensive reviews). Developed appropriately, phenomenological models can be used to produce patient-specific simulations of the electrophysiology during treatment and could, therefore, form a part of a therapeutic decision support system to minimise the impact of information loss in clinic.

The use of physiologically detailed mathematical models has enabled personalised 3D modelling of the atria, largely involving detailed biophysical models to investigate mechanisms behind the sustenance of AF [161, 162]. Additionally, fibrosis patterns have attracted significant recent attention [163], and results obtained from the detailed models have elucidated the role of so called 'islands of fibrosis' in the atria [164]. Further, techniques are in place for the simulation of 'virtual ablation' and bipolar electrograms [165, 166, 167, 168]. In a 2014 study [10] a variety of ablation strategies were simulated and compared in a computational study, finding that CPVI with two additional linear lesions (along the roof and posterior wall) showed the highest AF termination rate.

However, such studies typically make the following assumptions:

1. the data collected and used to constrain the model is the 'ground truth';

2. ablated lesions made by the cardiologist are continuous.

Both assumptions are likely to be invalidated in the clinical setting, where significant information loss due to poorly connected electrodes is commonplace and conduction gaps create discontinuous lesions. These were highlighted in 2011 by Miyamoto *et al.* [70] who proposed a method to infer a pulmonary vein activation map via gentle movement of the catheter. In conclusion, they raised concerns that signals were unreliable due to some electrodes touching the endocardium whilst others were not. A further issue is that bipolar electrodes located symmetrically to a conduction gap will record a zero signal despite a wavefront passing through.

To address these challenges, we develop an application of the BOCF model (introduced in chapter 2 and discussed extensively in chapter 3) on a cylinder with regions of zero conduction representing ablated tissue to build simulated representations of the

bipolar signals recorded by the lasso catheter. Our focus on a simplified model of the phenomenology of the electrical signal, rather than a detailed model of the underlying electrophysiology, is twofold. First, a cardiologist uses information from the macroscopic electrical recordings to identify appropriate site(s) to ablate, without recourse to any detailed understanding of the underlying electrophysiology. Second, the time available for the surgical procedure is of the order one-hour meaning that the model must efficiently reproduce a signal to be of use as a decision support tool during the procedure. The BOCF model provides a pragmatic balance between the quality of the simulated signal and the computational time required to produce the output. For example, many detailed biophysical cardiac models, such as [4, 123, 130, 149, 150] require significant time (of order hours) to compute appropriate APs, rendering them inappropriate in the clinical setting. In contrast, the BOCF model can be run multiple times for parameter estimation and sensitivity analysis over much shorter timescales (of order seconds to minutes).

We demonstrate that this simple model can reproduce the activation pattern across electrodes recorded in clinic. Furthermore, we test the potential of the model to reconstruct recordings that have been lost to poor contact. We verify the accuracy of the simulated recording using clinical data and minimising the root mean squared error between the activation patterns in the model and those in the data. To test the accuracy of the reconstruction, we use recordings for which all channels are spiking cleanly and remove a subset, so that the original signal can be used for error calculation.

Further, we present results showing cases in which the reconstruction of signals via the model would lead to reducing the number of RFA pulses. Reducing the number of RF pulses would both minimise unnecessary damage to the heart and shorten the duration of the procedure. This is significant due to the correlation between the duration of the procedure and the rate of recurrence [160].

4.2 Methods

In this section, we introduce the mathematical model used to generate the underlying AP which is in turn used to generate a travelling wave of intracellular potential within the pulmonary vein. We describe the methods used to simulate the models and how their parameters may be calibrated (either from synthetic data or clinical recordings). We further describe how the model can be used to reconstruct missing channels from data collected clinically from a lasso catheter. A schematic of how the overall process might be used to provide clinical decision support is illustrated in Figure 4.2.
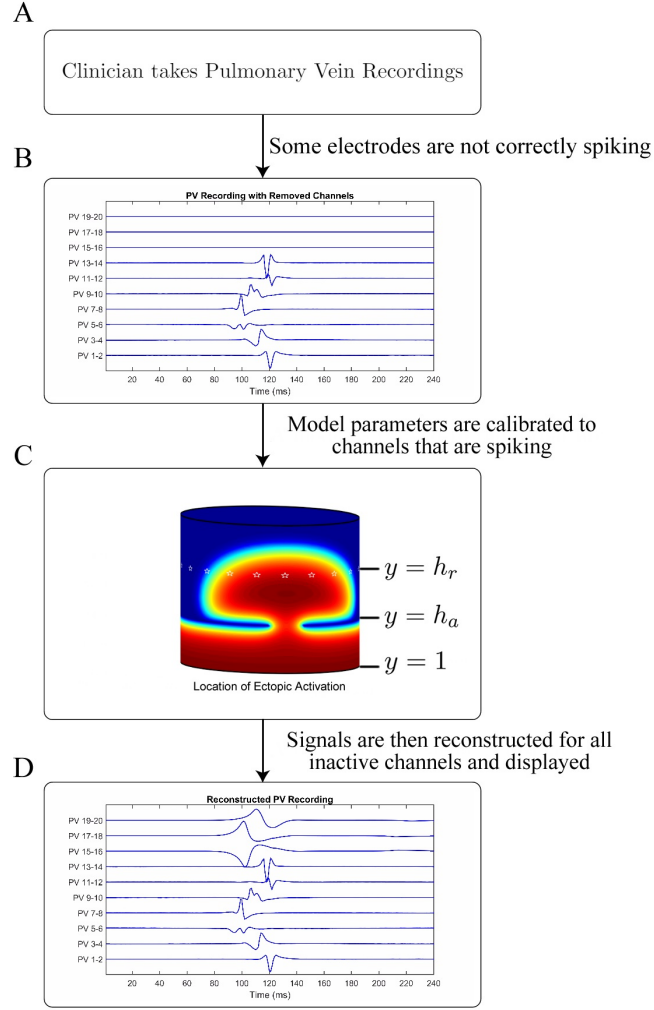
Figure 4.2: **Schematic and Application of Model.** Figure showing the intended application of the model. A) A cardiologist records Pulmonary Vein Recordings using a lasso catheter. B) An example of a pulmonary vein recording with some channels not correctly spiking (missing channels). C) A model simulation demonstrating the propagation through a conduction gap, showing high intracellular potential in red and low in blue. White stars are plotted on the electrode locations. D) The result of applying the model to the signal in B to recover the lost channels.

4.2.1 Mathematical model of the underlying AP

To simulate the pulmonary vein AP we use the four variable BOCF model as discussed in previous chapters. Given that the shape of the emergent electrical activity recorded on the lasso catheter may be constrained by the underlying structure and function of the AP, a propagating AP was simulated using the detailed biophysical Courtemanche model for the human atrium [4, 79, 169] as a proxy for clinical AP data. A generic AP from the

Courtemanche model was modified to account for the electrical remodelling associated with AF [11] and used as the initial stimulus for the BOCF model with parameters as defined in the sample fitting code in the appendix of [119].

These parameter choices were then evolved using the NMSS [154] (implemented by MATLAB's FMINSEARCH), by minimising the root mean squared error between subsequent APs (see Figure 4.3). Alternatively, any of the methods discussed in chapter 3 for single-objective optimisation would be appropriate. In this chapter we present the methods used in our published article for consistency. With a spatial resolution $\Delta x = 0.2$ mm, a diffusion constant of $D_{Court} = 2.615$ was necessary for the simulated wave front to match the conduction velocity of 48 cm/s observed clinically [153]. To eliminate any effects from boundary conditions or transients from the stimulus, the fit was performed at the point $x = 10$ mm on a tissue cable 20 mm long. A cycle length of 600 ms was used to match the clinical data. This process resulted in the parameter choices defined in Table 4.1.

Figure 4.3 shows the shape of the propagating APs under the above conditions using the BOCF model with parameters as in Table 4.1, alongside the Courtemanche AF model as described in [11]. The important qualities reproduced were conduction velocity (indicated by the simultaneous spike), upstroke velocity, and AP duration.

For the case of anisotropic diffusion an asymmetric finite difference method was used to simulate the BOCF model (see [81] or Appendix 2 for full details). Since in general the degree of anisotropy for an individual patient is unknown, we included the principal axes and eigenvalues of the diffusion tensor as additional parameters to be optimised by our fitting algorithm. Physiological studies place the anisotropy ratio between 2 and 10, [74, 170], which were used as bounds in our algorithms. The initial principal axes were placed at 45 degrees to the x and y axes, maximising the effect on the propagation pattern.

4.2.2   Simulating Pulmonary Vein Recordings

2D simulations of the pulmonary vein were performed by numerical integration of equation (2.16) by a finite difference method over a discretised cylindrical domain to represent the excitable myocardial sleeve extending over the base of the pulmonary vein. Dimensions vary from vein to vein, with the right inferior typically the largest and the left inferior the smallest [171]. We assume dimensions within the range of observed measurements: a length of 15 mm [172] and a diameter of 12.5 mm [173, 174]. A spatial resolution

Parameter	BOCF	BOCF-AF	Parameter	BOCF	BOCF-AF
τ_v^+	1.6650	1.6234	τ_{so2}	1.0261	0.9862
τ_{w1}^-	82.6769	69.1816	k_{so}	2.0487	2.3769
τ_{w2}^-	9.0959	14.1985	u_{so}	0.5149	0.9220
k_w^-	63.8099	65.4466	τ_{s1}	2.5879	2.5603
u_w^-	0.0331	0.0316	τ_{s2}	18.5596	12.5106
τ_w^+	213.1962	140.2385	k_s	2.0468	1.5749
τ_{fi}	0.1256	0.0990	u_s	0.7033	1.1640
τ_{o1}	431.0734	452.4879	τ_{si}	2.1260	2.1756
τ_{so1}	33.2039	25.6007	$w_\infty^\star$	0.6520	0.9408
τ_{so1}	33.2039	25.6007	$w_\infty^\star$	0.6520	0.9408
D_{BOCF}	N/A	0.8314			

Table 4.1: **Parameter Values of Bueno-Orovio Cherry Fenton Model.** The original parameters of the Bueno-Orovio Cherry Fenton model [119] alongside the parameters obtained from our fitting algorithm. Diffusion coefficient D_{BOCF} was not given in the original model.
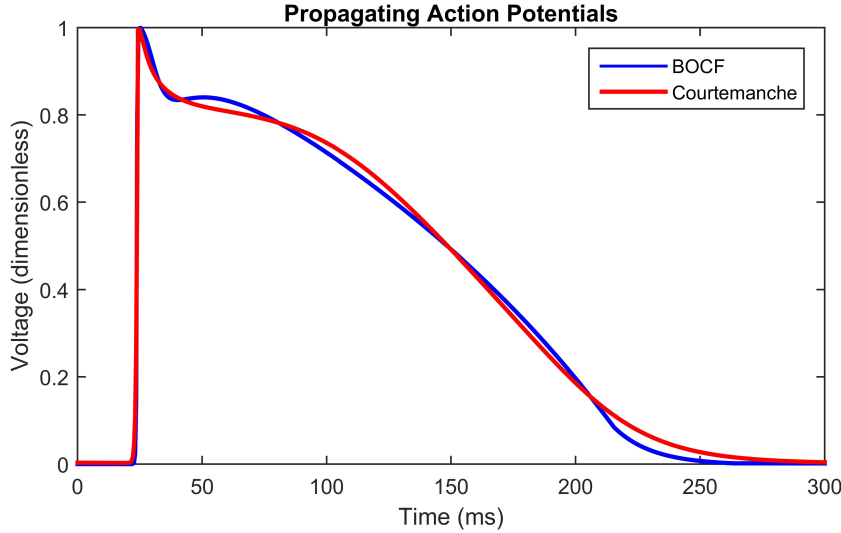
Figure 4.3: **Propagating Action Potentials.** Plots of Courtemanche [4] (blue), and BOCF [119] (red) models using the parameters in Table 1, of an AP at a point 10 mm from the stimulus with a spatial resolution of 0.2 mm and a time step of 0.01 ms. Model calibrated by minimising the root mean squared error using the NMSS. The Courtemanche model is solved using the parameters in [11].

of $\Delta x = 0.2$ mm was used to discretise this cylinder into a rectangular domain of 200 x 75 grid points. Periodic boundary conditions were used along the lines $x = 1$ and $x = 200$, whilst Neumann boundary conditions were used along the lines $y = 1$ and $y = 75$ (where x and y represent nodes on the grid). We set the conductivity to 0 to model the effect of lesions due to ablated tissue at the relevant points, following the approach introduced

in [165, 166, 167]. As we are only concerned with the effect on the AP propagation from the ablation process, we do not require a model of the thermodynamic processes of the catheter itself [175, 176].

A visual representation of this structure is shown in Figure 4.2, which shows the propagating intracellular potential with the lines $y = 1$, $y = h_a$ and $y = h_r$ annotated (panel C). An ectopic is initiated from a stimulus along the line $y = 1$; the edge of the myocardial sleeve furthest from the atrial junction. Virtual ablation is performed by introducing a line of lesions on the circle $y = h_a$ such that $D(x, h_a) = 0$. Conduction gaps are modelled such that $D(x, h_a) = D_{BOCF}$ (for conductive tissue on small segments of the circle $y = h_a$). Consequently, semi-circular wavefront(s) will form on the other side of the lesions. Although loosely based on the underlying mechanisms, the values of the obtained parameters are phenomenological and fit to the available data to ensure an accurate simulation on the lasso catheter electrodes, not to provide an estimation of the real location of the conduction gap.

We simulate pulmonary vein recordings from the lasso catheter across n electrodes (where n is typically 10 or 20), on $y = h_r$, where $h_r > h_a$. The electrodes are assumed to be equally spaced $d = 200/n$ apart, such that for an n electrode catheter $c = (a, h_r)$ where $a = \{d, 2d, ..., nd\}$). At each point $c = (x', y')$, an approximation for the surface potential Φ described originally in [177] is given by:

$$\Phi(x', y') = aD(x', y') \int \int (-\nabla u) \cdot \left[\nabla \frac{1}{r}\right] dx dy, \qquad (4.1)$$

where

$$r = \sqrt{(x' - x)^2 + (y' - y)^2}. \qquad (4.2)$$

Bipolar recordings between electrodes i and j (denoted PV i-j clinically) are simulated by

$$\text{PV i} - \text{j} = \Phi(a_i, h_r) - \Phi(a_j, h_r). \qquad (4.3)$$

Throughout this chapter, we divide the pulmonary vein into three equal sections, with the ablation line positioned at $h_a = 25$ and the recording catheter positioned at $h_r = 50$. This is a practical consideration, as quantifying these measurements during the procedure would be difficult given information collected as standard in clinical practice.

4.2.3 Relative Activation Time Curves

The important characteristics of both the simulated and recorded data are the activation times (from the maximal absolute value of dV/dt) of each signal compared to the others, as this gives a representation of the wavefront shape termed the *relative activation time curve*. It is necessary to use the absolute value as the recordings are bipolar. The relative activation time curve can be visualised by plotting the catheter along the x axis and its activation time on the y axis, giving a curve of the activation times of each signal relative to the others.

To understand the relationship between the relative activation time curve and parameters of the overall pulmonary vein model, the quantity, size and locations of conduction gaps are used as input parameters since these have the most profound effect on the emerging wavefront shape. The root mean squared error between relative activation times obtained from simulated and clinical recordings are minimised, again using the NMSS (implemented by MATLAB's FMINSEARCH) to establish the location of conduction gaps which result in the most accurate activation time curve. Here it is important to note we do not claim to have found the location of the conduction gap(s) via this fit, only that we have calibrated model parameters that most closely recreate the phenomenology of the waveforms from the recording catheter.

4.2.4 Reconstruction of Missing Channels

In the cases for which there is poor contact between recording catheter and tissue, the signal is typically flat or white noise. This is evident, for example, in channels PV 3-4, 17-18 and 19-20 in Figure 4.1. To reconstruct missing electrode recordings, a partial relative activation time curve was obtained from the active channels. Model parameters of the overall pulmonary vein model were calibrated from the active channels, using the NMSS (implemented by MATLAB's FMINSEARCH).

4.2.5 Clinical Data

Pulmonary vein recordings used in this chapter were obtained from adult male and female subjects undergoing pulmonary vein isolation therapy at Bristol Heart Institute. Bipolar recordings were obtained from a deflectable, circular, 20-pole Lasso catheter (Biosense Webster Ltd). Patients with both paroxysmal and persistent atrial fibrillation were included but all cases were paced into normal sinus rhythm by pacing at 600 ms intervals, as per standard clinical practice. All data were appropriately anonymised prior to their use in this study. Under United Kingdom law, patient data collected during normal clinical

routine and anonymised before research use may be used for research without additional consent.

4.3 Results

4.3.1 Model Simulations

Firstly, we explore dynamics of the model. The heat maps in Figure 4.4 show the intracellular potential and an approximation of the surface potential from Equation (4.1) on the pulmonary vein. The ablated lesion exists along the line $y = h_a$, denoted on the y axis label, with a small conduction gap which allows propagation of the action potential towards the electrodes (illustrated by white circles). The boundaries on the top and bottom of the grid are Neumann, while on the left and right periodic boundaries are used such that the rectangular heat map represents a cylinder. This is more clearly shown when the surface potential is used, as in panel b) of the figure, on which it is clear that the left boundary matches up with the right boundary. The intracellular potential of this simulation with the corresponding synthetic PV recordings is available as an animation in `https://www.youtube.com/watch?v=hoCOJ66BBOI`.

As we are taking bipolar recordings, the spike on the simulated pulmonary vein recording is influenced by but does not directly resemble the action potential morphology. In Figure 4.5 we show one representative channel of the pulmonary vein recording. The black signal is a channel simulated directly from the intracellular potential, i.e., simply subtracting one action potential from another. The red line is the voltage trace resulting from applying equation (4.2).

When the cell at the first node experiences an action potential, the second node is still at the resting potential due to the high value of dV/dt following the stimulus. As the action potential has a sharp upstroke and a slow recovery to the resting potential, when the second cell fires and reaches its maximum, the first one is still in the plateau phase, causing a return to the baseline when the difference is calculated from the intracellular potentials. Any subsequent activity is small oscillations resulting from both cells returning to the resting potential. As the surface approximation takes a greater area of the domain into account, the difference in maximal dV/dt between activation and recovery is much smaller, resulting in a biphasic spike pattern which more closely resembles the morphology recorded in clinic (blue line).
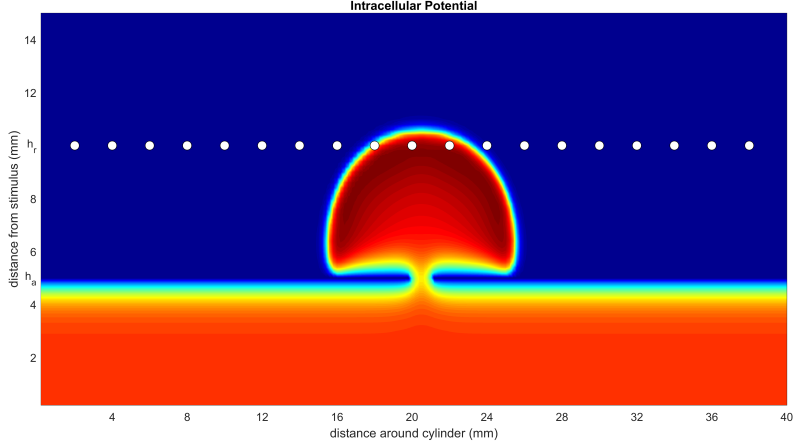
(a) Intracellular potential as wavefront passes through conduction gap
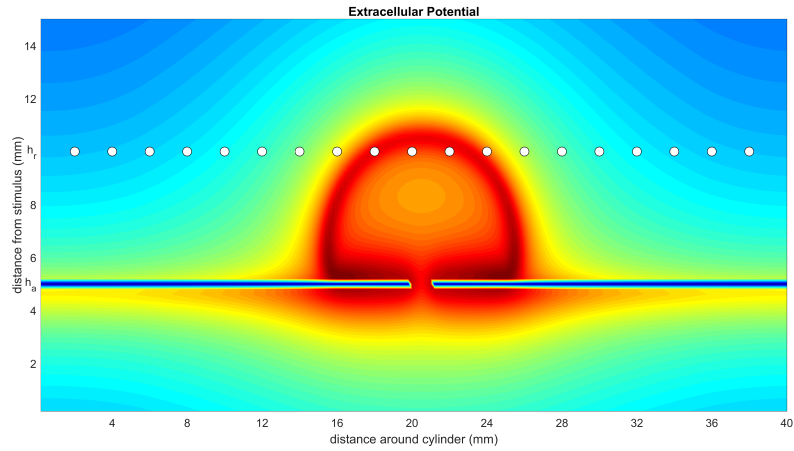
(b) Approximation of the surface potential

Figure 4.4: **Simulation of Pulmonary Vein Electrophysiology.** Heat maps of the intracellular potential (a) and an approximation of the surface potential (b) as a cardiac wavefront passes through a conduction gap on a cylinder at the same point in time with the same parameters. The electrodes are illustrated by white circles, with h_a and h_r noted on the y axes. Red corresponds to regions of high voltage, and blue corresponds to regions of low voltage. The surface potential is more symmetrical about the wavefront.

4.3.2 Fitting Model to Data

Next, we consider how well the model can reproduce the phenomenology of the pulmonary vein recordings when all 10 channels are active. To consider this, we use an exemplary set of clinical pulmonary vein recordings collected during pulmonary vein isolation therapy (as described in the methods). The goodness of fit between clinical recordings and model simulations is determined by minimising the root mean squared error between the relative activation times of the model and the data. This is achieved by varying the positions of conduction gaps in the model. The average of ten recorded events in the data is used to
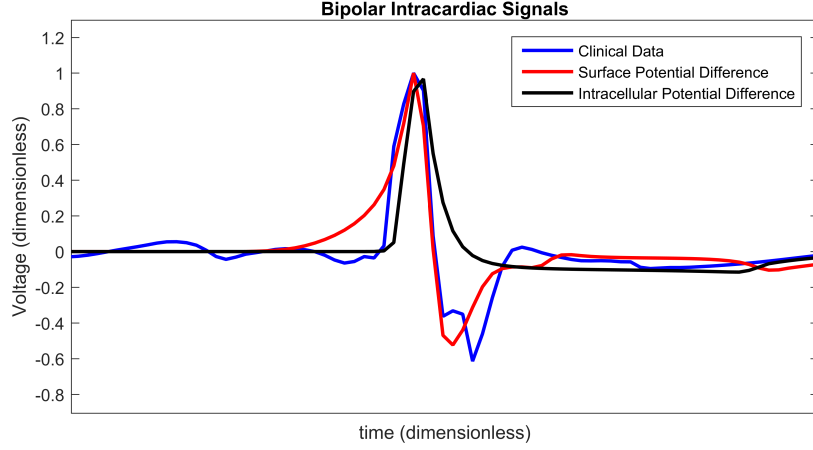
Figure 4.5: **Bipolar Intracardiac Signals.** Voltage traces of bipolar recordings from the data (in blue) from calculating differences between intracellular potentials (in black) and from applying the surface potential approximation before calculating potential difference (in red). Using the surface potential approximation gives a much better representation of the biphasic spike seen in clinic. Time has been rescaled to easier compare morphologies.

form the target relative activation time curve. This ensures some robustness to variation in the data and enables us to estimate the conduction gap location and width as parameters, which should be constant until ablated.
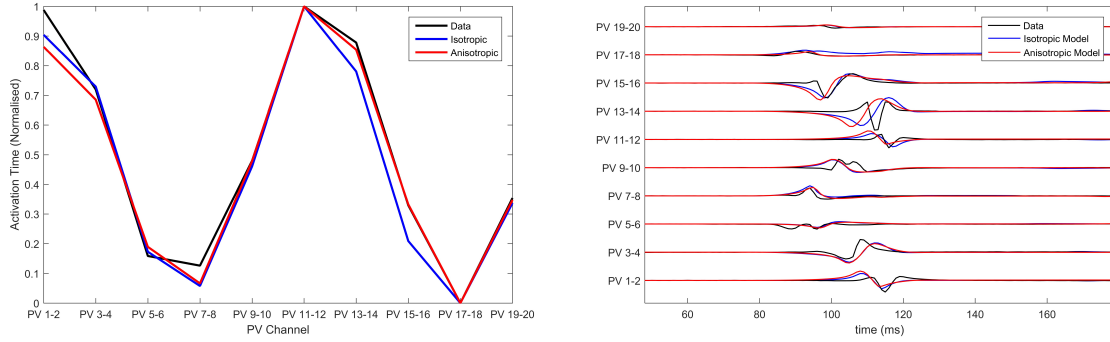
(a) Relative Activation Time Curves

(b) Model and Clinical Pulmonary Vein Data

Figure 4.6: **Parameter Fitting and Comparison with Clinical Recordings.** a) Presenting the relative activation time curves for the clinical data [presented in full in panel 4b)] (black), the model assuming isotropic diffusion (blue) and the model assuming anisotropic diffusion (red). Parameters of the model were calibrated by minimising the root mean squared error between clinical recording and the model using the Nelder-Mead method. b) Presenting an exemplar of clinical pulmonary vein recordings collected during pulmonary vein isolation therapy at the Bristol Heart Institute (black). Overlaid are the model simulations, with parameters calibrated as described in 4a), under the assumption of isotropic diffusion (blue) and isotropic diffusion (red) respectively.

For the chosen clinical data, and for parameter choices of the underlying BOCF model as in Table 1, we find that the root mean squared error between the relative activation time curve of the clinical data and that of the model (assuming isotropic diffusion) is minimised by placing conduction gaps centred on points $x = 65.5$ and $x = 167$, with widths 11 and 6 respectively. Both the number of minima and their locations are used to optimise position and width of the conduction gaps. This is important since both the number of minima and their locations within the relative activation time curve emerge as a result of the conduction gaps generating the signal. In current clinical practice, the earliest activation time(s) (e.g. the minima of the relative activation curve), are the most important, as these are assumed to be closest to the conduction gap and therefore the optimal ablation site. This is illustrated in Figure 4.6a, where we also present a model fit under the assumption of anisotropic diffusion. In this case the conduction gaps are centred on points $x = 59.5$ and $x = 164.5$, with width 11 and 13 respectively.

In Figure 4.6b, we present a comparison between the original choice of clinical pulmonary vein recordings and simulations for the two classes of model. Time units of the model are rescaled such that the relative activation time-scale of the model is equivalent to that of the clinical recordings, which permits a clearer visual comparison. Note that both classes of model result in visually similar simulated pulmonary vein recordings. We perform a more rigorous analysis of differences between anisotropic and isotropic diffusion later when considering the ability of the model to reconstruct missing channels in the clinical data.

Next, we tested the capacity of the model to predict future ectopic events, given an average over an initial ten events. For the identified choice of model parameters from the initial ten events, we simulated a series of additional ectopic events and for each event we calculated the root mean squared error between relative activation time curves obtained from either simulated or clinical ectopic events. We define t_0 as the time of the last event in the training set, and t_N as the time of the Nth subsequent ectopic event. Figure 4.7 shows how this error scales as the number N of the ectopic event moves further away from the training set. The apparent periodicity in the error is most likely due to rhythmic movements of the patient, such as breathing.

4.3.3 Reconstructing Missing Channels

We now focus on the capacity of the model to reconstruct missing channels, exemplars of which were shown in Figure 4.1. This is a key result of this chapter and the one with most relevance to a potential clinical decision support system. To test the accuracy of the
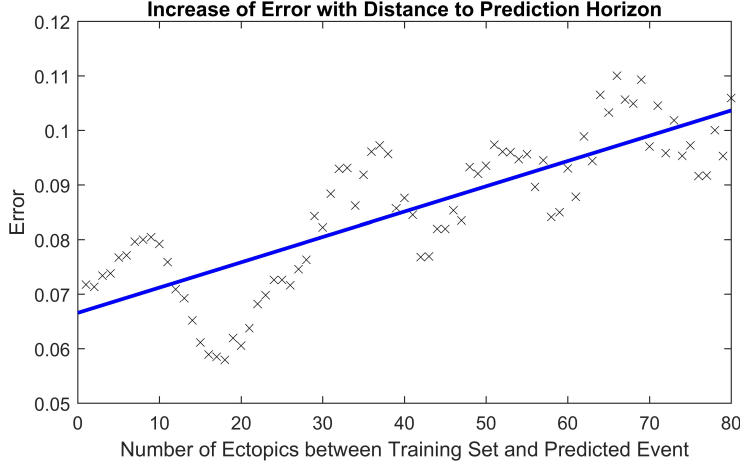
Figure 4.7: **Increase of Error with Prediction Horizon.** Illustrating how the root mean squared error in the activation time curve scales as the number of the ectopic event N increases away from the initial ten ectopic events used to calibrate model parameters. The line of best fit is displayed in blue. The periodicity in the error is likely due to rhythmic movements of the patient, such as breathing.

model, we start with a clinical recording for which all channels are active. We then eliminated a subset n ($n = 0$ to 5) of the channels replacing them with a zero time trace. Five was chosen as the upper limit since clinically a recording with less than half the channels active would not be relied on for determining the site of ablation. We then estimated model parameters using the same approach as in the previous section, but only data from those channels that were active. Using these parameters we then contrasted the error between the relative activation time curves obtained from the simulated next ectopic event and the subsequent ectopic event from the original clinical recording (including all channels). This enables us to assess how well the model can reproduce clinically relevant information (since the relative activation time curve is used for determining the site of ablation).

Figure 4.8 shows a box plot for each value of n. Each box in the box plot represents the root mean squared error between the relative activation time curves obtained from the average across 20 model simulations (with anisotropic diffusion and without) and that obtained from a clinically recorded ectopic event. The case $n = 0$ enables us to consider the limit of the goodness of fit between the model and the clinical data. This is effectively the intrinsic error attributable to the choice of model. For subsequent plots, n random channels were removed from the training set (simulating the effect of lost information due to poor contact). Different time intervals and different signals were used for each calculation so that the error distribution presented is as close as possible to the errors
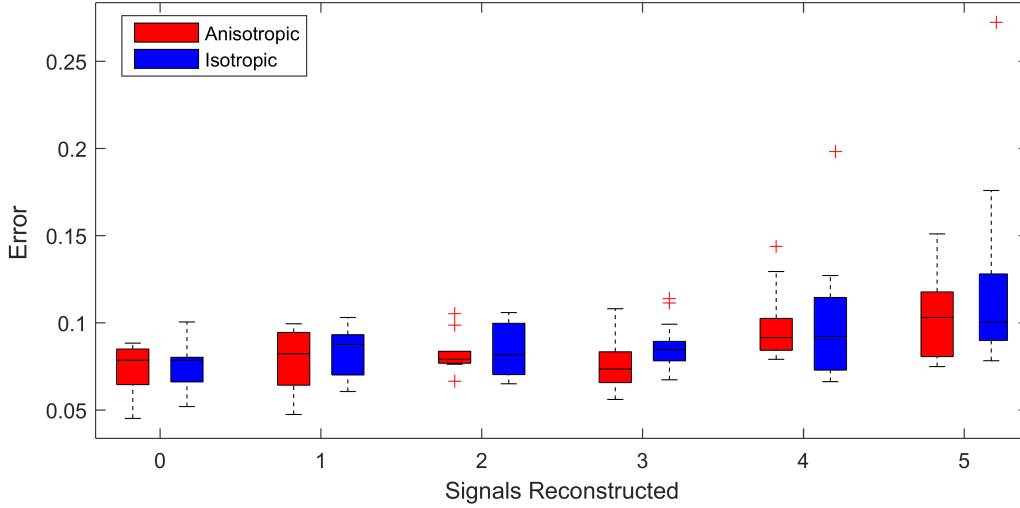
Figure 4.8: **Error vs Number of Reconstructed Channels.** Box plot illustrating how increasing the number of missing channels influences the minimised root mean squared error between the relative activation time curves obtained from the model (assuming both anisotropic diffusion (red) and isotropic diffusion (blue)) and the original clinical recording. For each case, 20 simulations for up to 20 random choices of channels to be reconstructed were performed. (+) symbols denote outliers in the 1% tail of the error distributions. The case of 0 reconstructed channels enables a comparison of the limit of the goodness of fit between models and the clinical data. We see that for 3 or fewer channels being reconstructed, uncertainty is predominantly due to model choice rather than the number of reconstructed channels, as we see no significant change in the mean error between model and clinical data. We use an unequal variances t-test to determine whether the errors came from a distribution with equal mean and find that with the exception of 3 channels reconstructed there is no significant difference in the errors between models.

that we might expect to observe in clinic. This is important as it minimises the likelihood of observations simply being due to an artefact of the ectopic event chosen for the fit.

For up to 3 channels reconstructed, the median and maximum errors do not significantly increase over that of the control whether or not anisotropy is considered. This is an important result as it demonstrates reconstructing up to three missing channels is not a significant source of additional error and therefore the model as presented may ultimately have clinical use under these conditions. Removing more than 3 channels leads to information loss resulting in outliers with statistically significant errors (see the cases for 4 and 5 channels removed). This demonstrates the limit of the number of missing channels that the considered models can reliably reconstruct.

To consider the whether the assumption of anisotropic diffusion is significant, we

performed an unequal variances t-test (so-called Welch's t-test) to test whether the errors from each model could have come from a distribution with the same mean. This test consistently showed no significant difference ($p > 0.05$), except for the case of 3 signals reconstructed ($p = 0.0414$). This suggests that whilst anisotropy is clearly important in terms of the underlying physiology, it does not significantly affect the quality of model fit to the phenomenology of the recorded signals. This is an important consideration as calibration of model parameters is more efficient under the assumption of isotropic diffusion.

4.3.4 Potential Clinical Application

To test the potential of this technique to aid the clinical procedure, we presented a cardiologist specialising in pulmonary vein isolation therapy, with three variations of clinical recordings collected from three patients:

1. the original clinical recordings with all channels active;

2. the original clinical recordings with key channels identifying the earliest activation hidden;

3. a hybrid whereby we reconstruct channels (removed in scenario 2) using the mathematical model and present these alongside the remaining active channels.

These scenarios are illustrated in Figure 4.9. The cardiologist was unaware of the origin of each recording, and to avoid bias, the recordings were supplied in a random order. The following results were obtained (summarised in Table 4.2 for convenience). For patient 1, given the original data, the first point of ablation would have been around PV 5-6, with PV 15-16 noted as a second choice. With channels 15-16, 17-18, and 19-20 removed, only PV 5-6 was identified as the only appropriate ablation zone. When these channels were reconstructed by the model, PV 17-18 was identified as the second choice of ablation target. For this patient, the model has helped to identify a second relevant ablation target that was not identified when channels were missing. If initial ablation is not successful, the cardiologist will ablate in the area surrounding the target area, hence an initial estimate closer to the optimal location will result in successful isolation using fewer radiofrequency pulses. This will result in a smaller region of tissue being ablated and a shorter procedure.

In the second patient presented, a clear earliest spike time was present on PV 5-6. The removal of PV 5-6 and its neighbours led to PV 9-10 being identified as an ablation

97

Patient	Missing	Reconstructed	Original
1	PV 5-6	PV 5-6 / 17-18	PV 5-6 / 15-16
2	PV 9-10	PV 5-6	PV 5-6
3	PV 3-4	PV 9-10	PV 7-8

Table 4.2: **Effect of Signal Reconstruction on Clinical Decision.** The channel corresponding to the area the cardiologist would ablate given the recording with channels missing, the original data, and the data with the missing channels reconstructed via the model. The decision made with the reconstructed signals is closer to the original than the decision made using the missing recordings, demonstrating that the model reconstruction has minimised the impact of the information loss on the clinical outcome. Recordings from Patient 1 are given in Figure 4.9.

target. In this case, the reconstruction led to the same zone being targeted as the original signal, while the estimation with the recordings missing was two channels away. For this patient, reconstruction of the missing recordings led the cardiologist directly to the optimal decision.

In the final patient, the earliest spike, on PV 7-8, was removed, along with PV 5-6 and 9-10. As previously, these missing channels shifted the chosen ablation target by 2 channels. The reconstructed signal led to a target selected which was closer to the target chosen with all information present. As with patient 1, we infer this result as satisfactory, as starting closer to the optimal target will lead to quicker isolation of the pulmonary vein.

In all three cases, the missing channels influenced the decision made by the cardiologist, demonstrating the potential impact of information loss in clinic. However, when the cardiologist used the recordings combined with the signals reconstructed by the mathematical model to make a decision, the decision made was closer to the decision that would have been made had all information been present. Whilst these results provide only limited proof of concept at this stage, assuming the original data and clinical decision to represent the "ground truth", then we believe there is significant potential for our approach to minimise the effect of this lost information.

4.4   Discussion

In this chapter, we have demonstrated that key features of pulmonary vein recordings can be generated by a phenomenological model, in this case, the BOCF model. Calibrating parameters of the BOCF model using the post fibrillation AP of atrial myocytes, simulated using the biophysical Courtemanche model, provides a method for rapid simu-
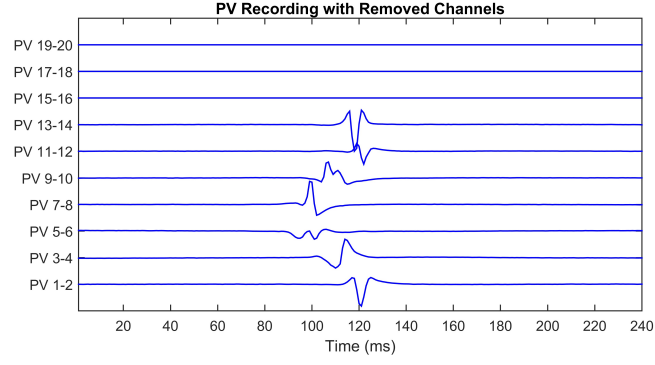
(a) Pulmonary Vein Recording with Channels Removed
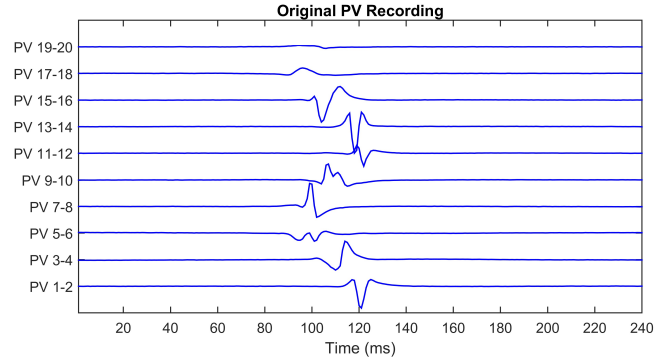
(b) Pulmonary Vein Recording with Original Channels
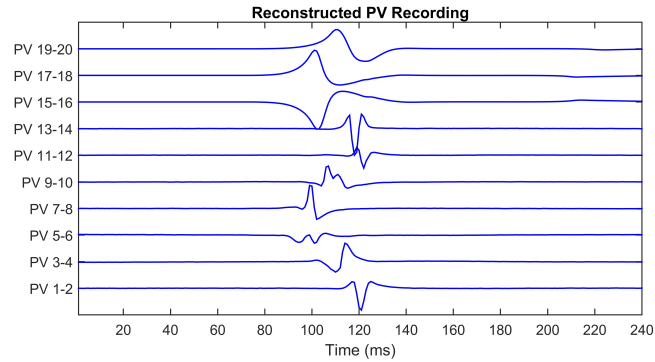
(c) Pulmonary Vein Recording with Reconstructed Channels

Figure 4.9: **Illustrating the model reconstruction of pulmonary vein recordings.** In panel a) we present the original recording with three removed channels. In panel b) the original recordings, and in panel c) the original recordings combined with the reconstructed channels using the mathematical model. We presented these data to the cardiologist who made a decision about the tissue underlying the channels they would ablate in each case. This process was repeated for patients 2 and 3. In all three cases reconstruction of the missing signals resulted in an improved clinical decision in contrast to only using the recordings with missing signals.

lation of atrial cells afflicted by AF-induced electrical remodelling. This is in contrast to more detailed biophysical models [4, 123, 130, 149, 150] which may take several hours to produce an output. Given that pulmonary vein isolation therapy typically lasts at most two hours, having a mathematical model that can run in close to real time, is a critical advantage when assessing suitability as a potential clinical decision support system.

Towards this aim, a primary result of this study was to model the phenomenology of recordings from the lasso catheter used during the pulmonary vein isolation therapy of AF. We found that the resulting model simulations accurately reproduce the relative activation time curve seen in recordings from patients undergoing this procedure. The pulmonary vein recordings made in this process are not always complete; there is often the complete loss of some of the recording channels. This is most commonly due to poor contact made between electrodes on the catheter and the pulmonary vein itself. This loss of information can result in non-optimal clinical decision making during the isolation therapy procedure. To address this issue we have demonstrated that a mathematical model fitted to the available channels of the data can be used to reconstruct those missing channels and we presented evidence in support of the accuracy of these reconstructions through comparison to clinical data.

Of note, we find that up to three channels can be reconstructed without significantly increases the inherent error due to the use of a model. The results show that, in principle, these ideas could be adapted as part of a clinical decision support system, which could be run in the operating theatre and provide information to the cardiologist during the procedure.

A potential limitation of this study is the loss of biological detail arising from our use of a phenomenological model over a biophysical one. However, it is important to note that the appropriateness of any mathematical model is dependent on the challenge it is designed to address. Here, we focus on the case of pulmonary vein isolation therapy, where a cardiologist is using recordings of the emergent electrical signal from the heart to make rapid decisions about regions of the heart to ablate. Consequently, a model that can capture the phenomenology of these recordings (which ultimately are what the cardiologist is using to guide their decision making) is a valid approach and does not require a detailed analysis of the contribution of ionic channels and other physical quantities involved in AP propagation.

In our current model, a number of assumptions have been made, most importantly

100

regarding the conductance and the geometry. Whilst we account for anisotropic diffusion by considering additional parameters, the diffusion tensor used is still homogeneous across the conductive tissue, and the wave approaching the conduction gap is planar. This is primarily since detailed fibre direction information would not be accessible to the cardiologist during the clinical procedure. A further key assumption is the approximation of the pulmonary vein sleeve as a cylinder. In the clinical procedure, the relevant region of cardiac tissue is not only the pulmonary vein sleeve but also the atrial tissue surrounding the ostium. However, while tissue expansion and asymmetry of an anatomically accurate domain may affect the results for a given set of parameters, the signal reconstruction technique incorporates the fitting of the parameters to the available signals, which will account for the impact of these assumptions. Further geometrical assumptions, such as the angles between the incoming wave, the ablation line and the recording catheter, can not be quantified using standard clinical equipment and so we do not consider them in the current study. We also assume that all cells are free atrial wall myocytes, rather than pulmonary vein myocytes which have a shorter AP duration and amplitude in addition to a lower upstroke velocity in comparison to the left atrium [178]. However, under current clinical practice, it is not possible to identify which areas of the pulmonary vein ostium is populated by pulmonary vein myocytes as opposed to those of the atrial wall.

While the model developed in this chapter has been developed with clinical applicability in mind, future work will be necessary to establish the ultimate validity of and optimise this approach in a clinical context. In particular, it is important to establish the optimal level of detail of model required to reconstruct missing signals, and whether additional detail can improve the accuracy of the methods, given the constraints of time and recording protocols in standard clinical practice. Further, clinical metadata regarding the locations and times at which ablation was performed on the patient is typically not collected during the ablation procedure, so it is difficult to infer the optimal ablation zone from patient data. The availability of such data would open up many new lines of research, including the use of either phenomenological or biophysically detailed patient-specific models to estimate the optimal ablation site directly.

Chapter 5

A Data-Driven Approach to Signal Reconstruction

5.1 Introduction

5.1.1 Background

Previous work in this thesis has been focused on the modelling of cardiac tissue by focusing on the electrophysiology, specifically the AP, and how it propagates through tissue. This process has facilitated the modelling of clinical signals recorded by the lasso catheter during treatment of radiofrequency ablation. However, for this problem, the most important quantity which we are trying to model is the activation times across the channels in the recording. Clinically, the morphology of the emerging spike is of much lesser concern than its activation time. In this chapter, we explore methods by which the activation time across the recording catheter may be approximated without recourse to models of cell dynamics.

The primary advantage of such a technique would be the significant reduction in computation time. Even the simplest AP models require the solution of a reaction-diffusion PDE, which can be computationally intensive on a large grid with a small time step, especially so when parameters of the PDE must be calibrated. This would lead to a decrease in computation time (especially so when parameters must be calibrated, requiring multiple runs of the PDE). The trade off is the significant loss of biological feasibility and detail. Without a realistic mechanism generating any synthetic data, the scope of questions that can be interrogated using the model is much smaller. In this section, we briefly review the existing model-free approaches, then develop extensions and methodologies by which these could be applied to address the problem described in the

previous chapter: the reconstruction of missing channels on pulmonary vein recordings.

5.1.2   Review of Existing Methods

Path-Finding Methods

One way to quantify AP propagation without modelling the AP itself is to use graph-based path-finding methods. Path finding methods rely on the fact that the cardiac AP is transferred only by gap junctions (short range connections), and therefore the time taken for an AP to propagate from one point to another is closely related to the shortest distance between the two points across the tissue surface.

The standard algorithm to find the shortest distance between two points on a weighted graph is Dijkstra's Algorithm, proposed by Dijkstra in 1959 [179]. Dijkstra's algorithm uses an iterative procedure, starting from the start node, n_s, and working towards the goal node, n_g. We define a set 'closed' as the set of nodes that have been 'visited' by the algorithm, and a set of tentative distances T, which are originally 0 for $n = n_s$ and ∞ for all other nodes. For each step in the algorithm:

1. The unvisited node n with the shortest tentative distance $g(n)$ is visited

2. The tentative distance of all neighbouring nodes n_i not in the visited set is updated to $\min\{g(n_i), g(n) + e(n, n_i)\}$ where $e(n, n_i)$ is the weight of the edge from n to n_i

3. n is added to the set 'closed' and the tentative distance is the shortest path from n_s to n. The algorithm terminates when $n_g \in$ closed

Such algorithms were investigated in the context of cardiology by Wallman in [180], in which a development of Dijkstra's algorithm, known as the A* (A Star) algorithm, was used to estimate the arrival time of a propagating cardiac wavefront on a 3D mesh by calculating the shortest path across the tissue. Dijkstra's original algorithm will always find the shortest path on any weighted network. The A* algorithm uses a heuristic $h(n)$ which provides an estimate of the distance of the optimal path from n to n_g [181]. When calculating a path through physical space, the heuristic is the Euclidean distance to n_g. Step 1 is modified so that the visited node is the one with the minimum $g(n) + h(n)$. This modification reduces the number of nodes visited on the way to n_g, although it is possible for the A* Algorithm to fail to find the optimal path if the Euclidean distance from node n to n_g is not a good estimation of the path length. This can happen if, for example, there is a region of very costly paths between node n and n_g, such that a longer
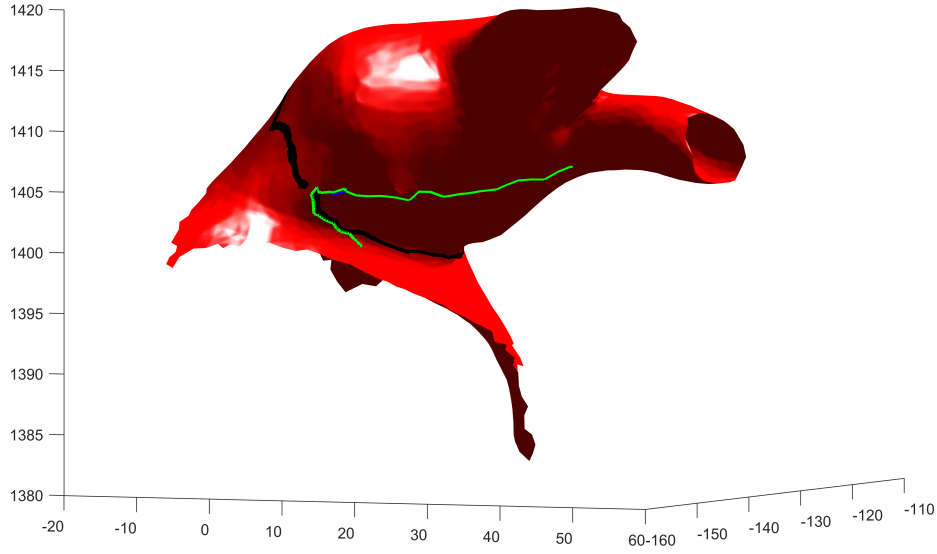
Figure 5.1: **Pathfinding on the Pulmonary Vein.** Shortest paths are shown from Dijkstra's Algorithm (green) and the A* Algorithm (blue) across a pulmonary vein. The blue path is mostly hidden behind the green path. The small discrepancy occurs when both algorithms take a different route around a parallelogram in the mesh and have identical path lengths.

path around this region is actually quicker.

We performed this method using the PV mesh recorded by the University Hospital of Bordeaux to find the shortest distance from one point to another (Figure 5.1). The cost along each path was assumed to be the Euclidean distance between the two points. As such, the Euclidean distance is a good heuristic and the A* Algorithm will find the shortest path. A line around the join between the PV and the atrium was drawn to represent an ablated lesion. All edges on the faces touching the vertices on this line were set to be of infinite length so that the path cannot pass through it. A gap was left to represent a partially complete lesion. The paths taken from both algorithms were identical lengths, with the only difference being that the A* Algorithm chose a different path around a parallelogram in the mesh.

Figure 5.2 compares the computational efficiency of the two algorithms by calculating the shortest path across a straight but long section of the PV. Both algorithms computed identical shortest paths. However, 3512 vertices were visited by the A* Algorithm, while Dijkstra's Algorithm visited 20833 vertices, representing a significant decrease in computation time by using A*.

A limitation of this technique is the requirement of high-resolution heart scans, coupled with the locations of the electrodes in the catheter. In the model previously described, it was simple to place electrodes at equal points at a certain distance from the lesion. Any estimation of activation time patterns across a catheter using path-finding methods would be critically dependant on where we choose to draw the lesion, which number electrodes are on which side of the PV, and how we choose to orient the recording catheter.

(a) Nodes visited by the A* Algorithm   (b) Nodes visited by Dijkstra's Algorithm
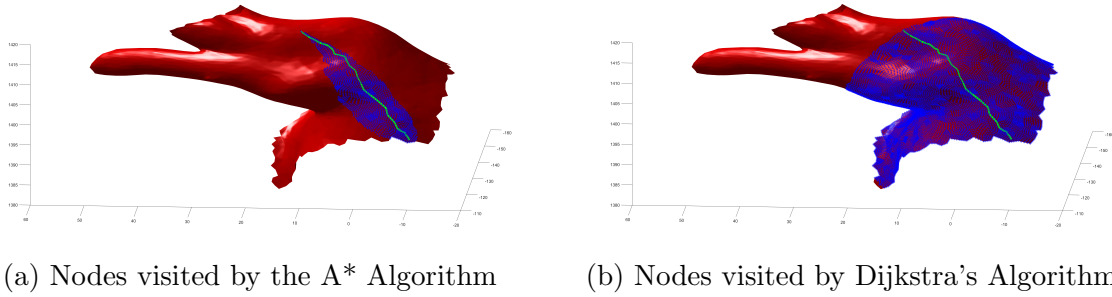
Figure 5.2: **Visited Nodes from A* and Dijkstra's Algorithm.** The optimal path (green) is identical for both the A* Algorithm (a) and Dijkstra's (b). However, the number of nodes visited by the A* Algorithm is signficantly smaller. The points marked in blue are the points visited by the algorithm, and is representative of the computation time reduction.

Weber's Sine Wave Model

An alternate 'model' proposed to represent the recording pattern across a circular catheter is a simple sine wave. [77, 182]. Although these studies were performed not with the recording catheter around the PV ostium (as it is in CPVI therapy) but on a flat wall of the atrium, the activation pattern across the catheter was modelled by fitting a sine wave to the activation times using the equation

$$t(n) = t_c - A \cdot \cos\left[\phi(n) - \phi_0\right]$$
(5.1)

where $t(n)$ are the activation times and $\phi(n)$ is the angle of the electrode on the catheter.

These studies were performed with clinical applications in mind. In [182], using the orientation of the catheter and the shape of the sine function, CV (calculated by sine wave amplitude) and direction of the wavefront (calculated by where the minima and

maxima are) were calculated accurately. The latter is especially relevant to our goals, as this was tested in clinic by pacing the atrium from the pulmonary veins. Fitting a sine wave facilitated the estimation of which PV was initiating the ectopic bursts, which would help a clinician know which vein to focus on. In [77], the technique was extended to estimate CV restitution, by pacing the atrium at different frequencies and measuring the CV.

Using a sine wave is a convenient and extremely efficient way of quantifying the activation pattern on the lasso catheter. However, as presented, the technique is too simple to model some of the issues faced in clinic during CPVI. For instance, the sine wave has been chosen with a period equal to the distance around the vein, meaning that each wavefront is modelled by one and only one full revolution. This is true for large wavefronts across the atrial surface, but not true if the recording catheter is placed around the pulmonary vein ostium, as two conduction gaps.

In this chapter, we investigate ways in which Weber's approach can be developed in a manner that can be applied to guiding a clinician during CPVI, which can be compared against the model previously described. We describe developments of the method to more accurately model the complexities occurring from recording around the PV ostium, and present results obtained from fitting to clinical data. From there, we describe methods by which synthetic pulmonary vein recordings could be developed to replace missing signals as previously described. As the techniques described in this chapter do not rely on a differential equation, parameter calibration and computation time are faster.

To put the time scales in context, computation one time step of one node of the BOCF model is approximately equal to 3 of the sine wave. With a spatial resolution $\Delta x = 0.2$ mm, we have 15,000 nodes to perform this computation, and at a temporal resolution of 0.01 ms, 60,000 time steps to simulate 600 ms of data. The ratio in computation times for the PV model to the Extended Sine Model is $2.7 \times 10^9 : 1$. The PV model has 4 parameters to calibrate to data compared to 5 from the Extended Sine Model. This reduction in dimensionality reduces the ratio in effective computation time in clinic to approximately $3.5 \times 10^8 : 1$, although this is of course dependent on the efficiency of the code.

5.2 Methods

5.2.1 Extended Sine Model

As in the previously discussed work, we use a sine function to model the activation across electrodes. However, we can exert a greater control of this function than has previously been explored by Equation (5.1). We introduce two new parameters:

1. ω - a parameter to control the frequency of the sine wave.

2. m - a parameter that permits a linear trend in the sine wave.

ω is an important consideration for the application, as this removes the assumption that the catheter contains only one cycle of the sine wave. This is important as there may be multiple conduction gaps in the ablated lesion, or a coiling of the lasso catheter, causing multiple minima to appear in the activation time curve. The linear term allows greater control of the curve. Without this term, both minima would occur at the same point in time, which is not usually the case, as the wavefront can pass through both conduction gaps at different times, or at different speeds (a smaller gap slowing propagation down greater than a larger one). We define x to be on the half-integers between the electrode numbers, for example, the channel PV 3-4, corresponding to the difference between electrodes 3 and 4, is represented on the x axis by $x = 3.5$. Our model, the Extended Sine Model, for the activation pattern is then:

$$y = A \sin\left(\omega(x - \tau)\right) + mx + c. \tag{5.2}$$

This equation can be used in the same way as Equation (5.1) for estimating the CV from the parameter A. As the x axis is representative of the electrode number and not physical space, the value of ω will depend on the number of electrodes on the catheter. $x = 0.5$ and $x = n + 0.5$ both correspond to the midpoint of the first and last channel. Therefore the model is defined on the interval $x \in [0.5, n + 0.5]$.

5.2.2 Reconstruction of Missing Signals

Equation (5.2) provides a quick and simple way of modelling the activation pattern across the catheter. It does not, however, contain a model for the morphology of the spike, and so simply calibrating the parameters to match the data does not immediately give us a method of producing a synthetic pulmonary vein recording in a situation where signals are missing. In this chapter, realistic synthetic spikes are generated by using the spikes of the channels on the catheter which are functioning correctly. This ensures a spike

morphology consistent with the other spikes on the catheter.

If some channel n is inactive, we can estimate the activation time by calibrating the Extended Sine Model to the others. Synthetic spikes can be generated by calculating a superposition of the neighbours of the series of inactive channels. As we are only concerned with generating one activation spike, copies of these signals are made, shifted so that they have the same activation time. The superposition of these two waves can be used to generate a synthetic spike. This can then be shifted such that the activation time is the same as the model predicts it should be.

If multiple consecutive channels are inactive, as is often the case in clinic, we use a weighted amplitude superposition of the neighbours of the inactive signals. For example, if PV 11-12 and PV 13-14 are both inactive, PV 11-12 is calculated by $(2 \times PV9 - 10 + PV15 - 16)/3$. This assumes that the wave morphology varies uniformly across the active channels.

5.2.3 Signal Processing

As in the previous section in which a reaction-diffusion equation was used to model PV recordings, clinical data from Bristol Heart Institute was used to validate model results. This data was collected according to the methods described in chapter 4.

In this chapter, we quantify the activation time using an adaptation of the methods described in [182]. Firstly, as cardiac electrograms are extremely noisy, each signal in the electrogram is denoised. We implement a wavelet-based denoising algorithm [183] as implemented by MATLAB's 'WDEN' function. Wavelet denoising is preferred over Fourier Transform-based methods as they preserve sharp features in the data and can maintain a fine resolution in both frequency and in time.

A *wavelet* is an oscillation with a well defined amplitude which starts and returns to zero at the end of the oscillation. The Wavelet Transform of a signal $x(t)$ is defined as a function of a scale parameter s corresponding to the frequency and a translation parameter τ describing the translation of the wavelet through the signal by

$$X(s,\tau) = \frac{1}{\sqrt{s}} \int_{-\infty}^{\infty} x(t)\varphi\left(\frac{t-\tau}{s}\right) dt. \tag{5.3}$$

The function $\varphi(t)$ is the *mother wavelet* a basis function used to generate wavelets by translation by τ and scaling by s. While a Fourier Transform uses a basis function $e^{i\omega t}$,
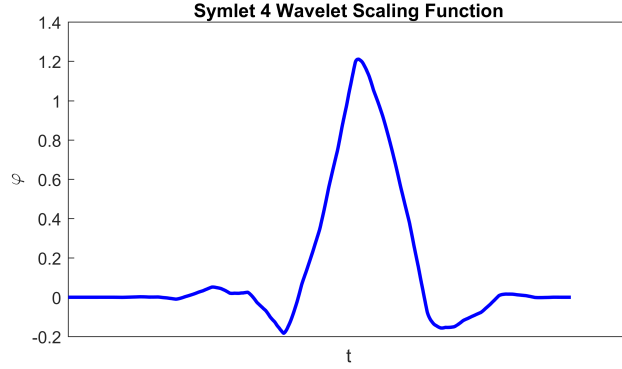
Figure 5.3: **A plot of the Symlet 4 Wavelet Scaling Function.** A plot of the function $\varphi(t)$ used in the Wavelet Transform in Equation (5.3). The scale on the t axis is irrelevant as the function is always scaled by a factor of s and translated by τ.

there are many different options for $\varphi(t)$, a comprehensive review can be found in [184]. Most common for denoising are the Daubechies Wavelets, introduced in [185], which have no closed-form solution but are calculated from the cascade algorithm [186]. The Symlet Wavelets are a modification on Daubechies with greater symmetry [187], and have been applied in a number of different fields for the purposes of denoising [188, 189]. A plot of the sym4 wavelet is given in Figure 5.3. The Wavelet Transform $X(s, \tau)$ is then thresholded and inverted to provide a denoised signal.

We then apply a Nonlinear Energy Operator (NLEO) to the filtered signal. The NLEO was originally designed for speech recognition applications [190],[191], and attempts to quantify the 'energy' E of a discrete signal x by the transformation

$$E_n = x_n^2 - x_{n-1} \cdot x_{n+1}. \tag{5.4}$$

The algorithm has more recently been used to quantify the level of activity in a noisy cardiac signal [192, 193]. The energy function E produces a sharp positive spike for epochs with a high positive second derivative and negative values of x, and epochs with a high negative second derivative and positive values of x. This indifference to sign is important for bipolar recordings, as both peaks of a biphasic spike will have positive energy.

As bipolar electrograms typically produce a biphasic spike, the resulting energy from the NLEO will often have two positive spikes (one for the up spike and one for the down spike). We apply a Gaussian Filter with a window width of 30 time points to the energy to find the maximum across multiple spikes [194]. The Gaussian Filter is a smoothing transformation with a number of applications, most notably used by the blur function of

(a) Raw Signal

(b) Denoised Signal

(c) Signal Energy

(d) Filtered Energy
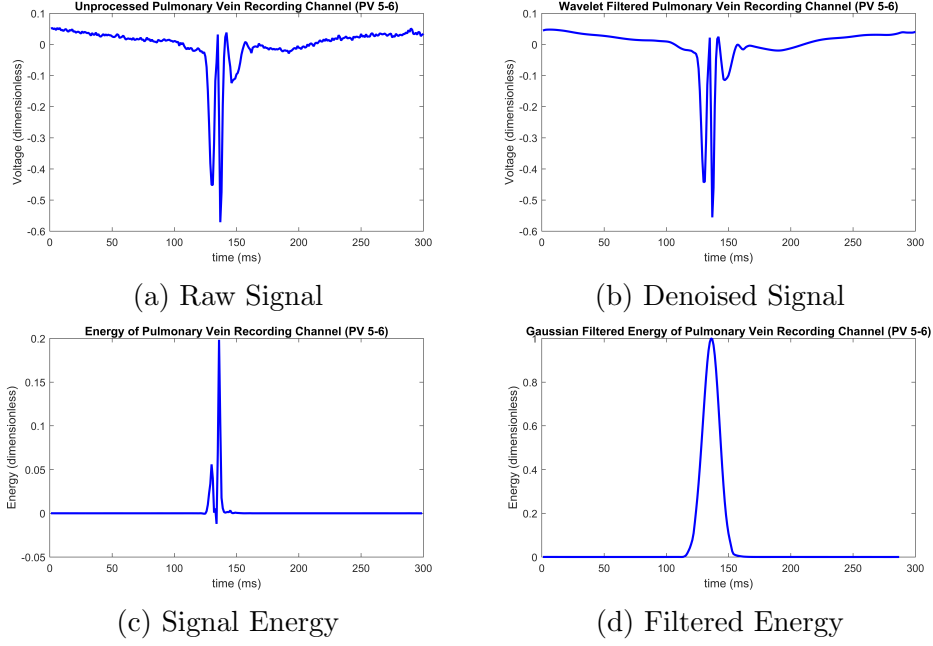
Figure 5.4: **Signal processing of a noisy PV recording.** The raw signal (a) is denoised using a Wavelet Transform of the type in Equation (5.3) to produce (b). Using the nonlinear energy operator (5.4) the 'energy' of the signal is computed (c). This is passed through a Gaussian Filter (5.5) to produce a smoothed energy function (d).

(a) Original Signals

(b) Activation Time Curve
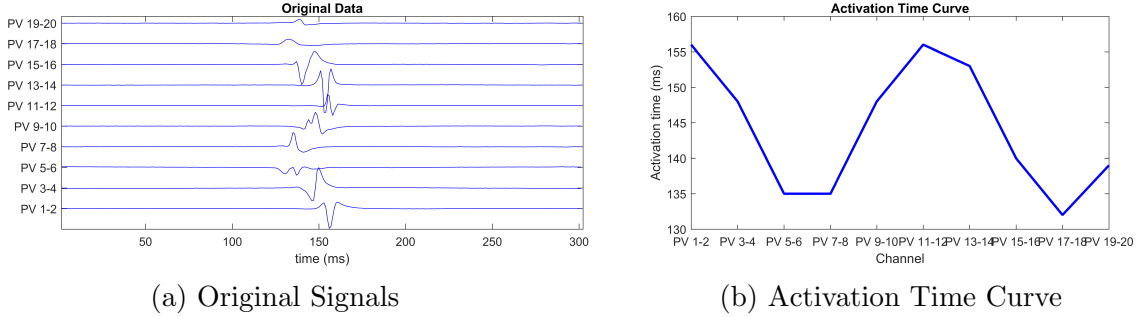
Figure 5.5: **PV Signals and Activation Time Curve.** (a) A PV recording with all channels correctly spiking. PV 5-6 in this signal is the example signal used in Figure 5.4 to describe the signal processing algorithms. (b) The activation time curve calculated from applying the described algorithms on all 10 channels.

Photoshop. A window of a discrete size (in our case 30) is generated by the function

$$w(n) = e^{(-n^2/2\sigma^2)} \tag{5.5}$$

where σ is the standard deviation of the Gaussian Function (0.4 for a standard Gaussian Filter). The function $w(n)$ then acts as coefficients of a moving average filter which passes through the signal. After the resulting filtered energy is shifted backwards by half the width of the window, the maximum of the smoothed energy function is inferred to

be the activation time of the signal. The whole process is given in Figure 5.4, and the application (the computation of an activation time curve) is given in Figure 5.5.

5.3 Results

5.3.1 Quality of Fit

Firstly, as in chapter 4, we investigate the capacity of the model to reproduce the phenomenology of the activation pattern across the recording catheter in an ideal setting. We quantify the goodness of fit by evaluating Equation (5.2) on values of x corresponding to the electrode numbers in the catheter, as defined in the methods. As all data used in this thesis is recorded on a 20 electrode catheter, x is defined on $1.5 + 2n$ where $n = 0$ to 9.

Figure 5.6 shows the result of fitting Equation (5.2) to the activation time curve of the exemplary pulmonary vein recording in Figure 5.5. We plot only the activation time curves as this model does not produce a time trace of the electrical signal to compare with the data. However, as the model is simply a continuous sine function, we can plot the relative activation time curve as an actual continuous curve. There is no need to normalise the activation time curve in this case, as Equation (5.2) has a parameter A to control the amplitude and c to control the y-intercept. For the data presented in Figure 5.6, optimised parameters were as follows: $A = -11.93$, $\omega = 0.5763$, $\tau = 3.712$, $m = -0.0341$, and $c = 145$.

While Weber's original paper used the parameter A to infer CV, this was performed with recordings on the atrial wall. In our case, in the pulmonary vein, the excitation wave does not pass across the middle of catheter (as this corresponds to the middle of the PV, where there is no tissue). Either a high CV or a low curvature would result in all electrodes activating closer together and lower the parameter A. As a result, due to tissue topology, we cannot infer conduction velocity. $\omega = 0.5763$ implies a sinusoidal period of 10.90, which corresponds to 1.83 complete cycles around the catheter, caused by the presence of 2 distinct conduction gaps. $m = -0.0341$ adds a slight negative gradient to the sine wave, causing one minimum to occur at an earlier time than the other, reproducing the known effect of cardiac wavefronts passing through a wide gap faster than a narrow one. The parameters τ and c simply change the initial phase of the sine term and the time since the recording began, neither of which have any relevance to the physiology.

Secondly, we demonstrate the importance of the additional terms introduced in Equa-
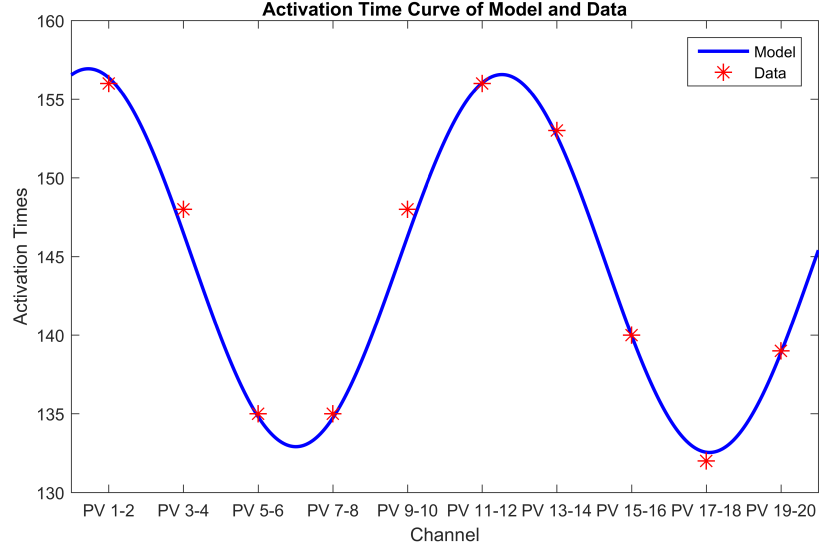
Figure 5.6: **Comparison of Extended Sine Model and Data.** Presenting a comparison of the Extended Sine Model for the activation times on a lasso catheter (blue curve) with recorded data from a patient collected during pulmonary vein isolation therapy at Bristol Heart Institute (red stars).
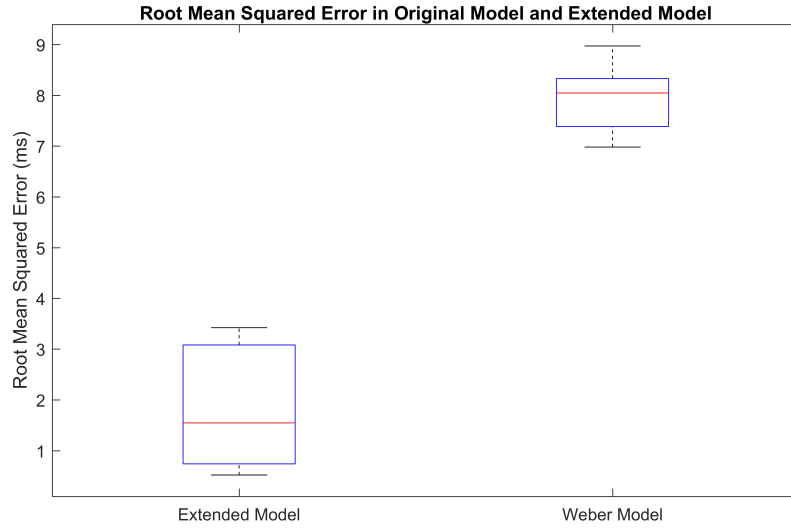
Figure 5.7: **Comparison of Errors in Sine Model and Extended Sine Model.** Boxplots presenting a comparison of the simple model for the activation times on a lasso catheter (blue curve) with recorded data from a patient collected during pulmonary vein isolation therapy at Bristol Heart Institute (red stars). Extended Sine Model was significantly better ($p = 3 \times 10^{-11}$).

tion (5.2) by comparing the quality of fit with that of Weber's original model (Equation (5.1)) described in [182]. We used 10 different ectopic events across the same 3 patients in the previous chapter and optimised both equations using the same genetic algorithm.

The results are demonstrated in Figure 5.7. The Extended Sine Model obviously has a significantly lower error ($p = 3 \times 10^{-11}$ from a Mann-Whitney Test).

The large error in the original model is due to the parameter ω, which is not fixed in our extended model. As the period in Weber's model is constrained to the circumference of the catheter, when applied to signals taken from within the PV, the frequency is often wrong. Minimising the RMS error naturally weights the optimiser towards eliminating the largest errors first. As a result, any parameter optimising scheme will avoid such regions of parameter space, and return a curve with an extremely small amplitude. As the model was designed to be used when the catheter is on the atrial wall, this evidence is not criticism of the model itself, but merely shows that the extended model is needed to model the catheter activation time when placed around the PV.

5.3.2   Reconstruction of Missing Channels

In this section, we present results from using the Extended Sine Model to reconstruct channels lost in the operating theatre. Firstly, we present an example case of using the Extended Sine Model to reconstruct recordings lost in clinic.
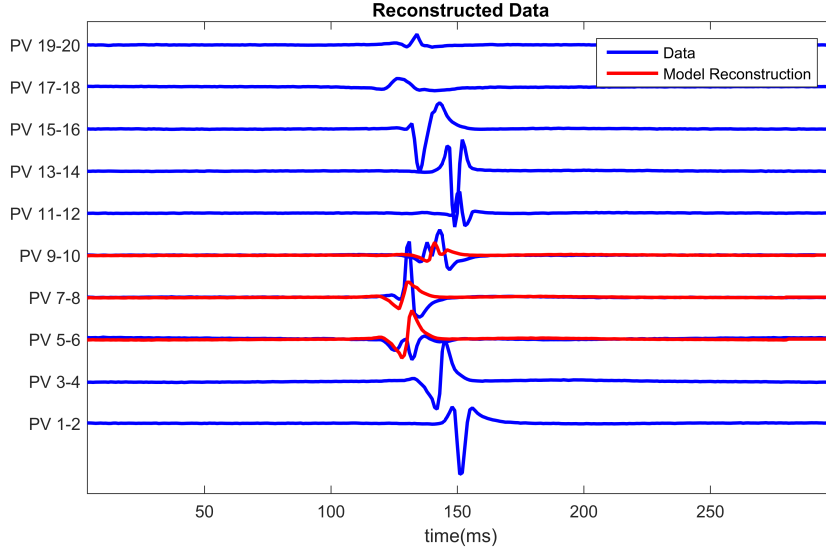
Figure 5.8: **Example of Signal Reconstruction using Extended Sine Model.** An example of reconstructing missing signals on PV 5-6, 7-8 and 9-10. The original data is shown in blue. The signals generated by the reconstruction algorithm driven by the Extended Sine Model is overlaid in red.

Figure 5.8 shows an exemplary case. Signals PV 5-6, 7-8 and 9-10 were removed from the recording prior to the optimisation of the Extended Sine Model. The activation times

on the missing channels, important for clinical decision making, are well reproduced by this technique. As the spikes on the reconstructed channels are formed by a weighted average of the time traces on PV 3-4 and PV 11-12, the result is a realistic spike which reflects the complexity of the spike on the recording. A realistic looking spike is potentially important if the technique is to be used by a clinician to make decisions.

We numerically quantify the error in this procedure in the same way as in the previous chapter: by taking a recording in which all channels are spiking cleanly and eliminating a random subset during the fitting procedure. The results of this are displayed in Figure 5.9, in which each box plot corresponds to a different number of channels being removed and reconstructed, and the y axis shows the RMS error in activation times across the recording. As both are RMS Errors across all 10 channels, boxplot 0 is essentially the same as shown for the Extended Model in Figure 5.7. This shows the error inherent in the model, which is used as a control to test how much of the error is incurred from the missing information.
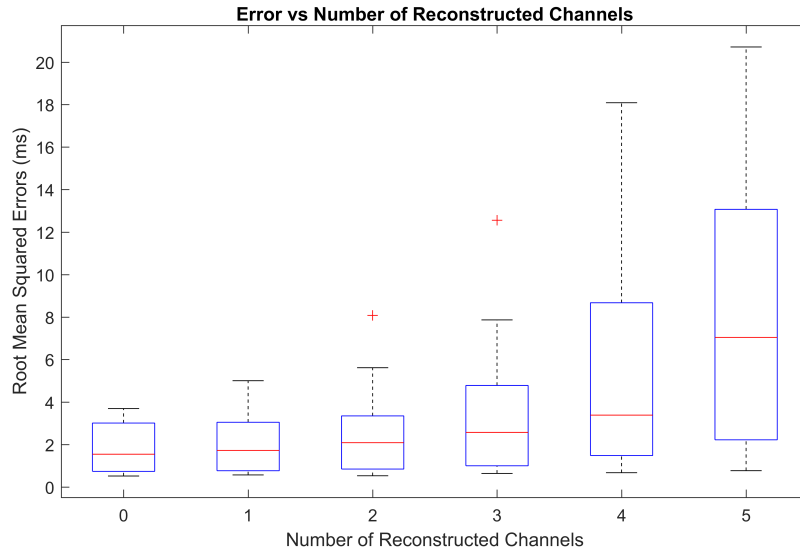
Figure 5.9: **Error vs Number of Reconstructed Channels.** Box plot illustrating how increasing the number of missing channels influences the minimised root mean squared error between the relative activation time curves obtained from the Extended Sine Model and the original clinical recording. For each case, 20 simulations for up to 20 random choices of channels to be reconstructed were performed. (+) symbols denote outliers in the 1% tail of the error distributions. The case of 0 reconstructed channels enables a comparison of the limit of the goodness of fit between models and the clinical data. For 2 or fewer channels, there is no statistically significant error incurred during the reconstruction. For 3, the error increase is significant but of a small magnitude.

Errors were compared using the Mann-Whitney Test. Reconstructing either 1 or 2 channels resulted in no statistically significant increase in error ($p = 0.3632$ and 0.2116 respectively). For 3 reconstructed channels, the upper quartiles of the errors are notably higher, and the distribution is significantly higher than that of 0 reconstructed channels to the 5% confidence interval ($p = 0.0281$). For 4 and 5 reconstructed channels, the errors are significantly higher than that of 0 ($p = 0.0014$ and 1.2493×10^{-5} respectively).

These results suggest that we can reconstruct up to two missing signals using the proposed technique without introducing additional error. In this results section, we do not perform the test on how this influences the clinical decision, instead this is explained in the following chapter on a much larger dataset, allowing for statistical comparisons to be made between the Extended Sine Model and the PV Model.

5.4 Discussion

In this chapter we have developed an extended version of an existing model for the activation times on the lasso catheter used during AF ablation. The original model was proposed to infer propagation direction and conduction velocity in the atrium by placing the catheter against the atrial wall. Such a model provides an advantage of several orders of magnitude in terms of computation time over the reaction-diffusion model presented in the previous chapter.

However, the model does not reproduce the activation times on the catheter when it is placed around the ostium of the pulmonary vein. Our extension of the model added two extra parameters that allow for the model to reproduce the activation patterns seen on the catheter on this topologically different surface with more complex wavefront curvature due to propagation through the conduction gap.

We demonstrated an algorithm that can use this model to reconstruct a missing signal by using the superposition of its neighbours. Up to 2 channels can be reconstructed with no significant increase in error. 3 channels results in a significantly significant but small in magnitude increase in error. It is unclear if this increase in error will compromise the ability of the model to guide clinical decision making in situations where more than 3 channels are missing. For more than 3 channels, the error increases quite rapidly, especially at the higher tail of the distribution.

There are a number of limitations in the techniques proposed in this chapter, most

notably from the extremely simplified model of the activation front. Unlike the PV Model described in chapter 4, the Extended Sine Model is not based on any underlying biological principles at all. While this approximation provides an improvement of several orders of magnitude in terms of computation time by avoiding the need for solving a PDE numerically, many assumptions are present. By the use of a sine wave, all minima will be equally spaced apart, which may not be the case in all clinical recordings. While extra parameters could help address this assumption, if too many parameters are introduced, the model could become over-defined for the number of data points remaining, resulting in an unreliable fitting process. Furthermore, the model is less adaptable to advances in technology. With the PV Model, various factors such as fibre orientation, local inhomogeneities in CV and shape of the PV were not included because they are not recorded in the standard clinical procedure, however, they could be in future work if this situation changes. This is not possible with the simplicity of the Extended Sine Model in this chapter, however, in its present form it may still be a viable alternative to reconstructing inactive channels in clinic.

The viability of this model in the operating theatre as part of a therapeutic decision support system during radiofrequency ablation will be investigated in the next chapter alongside the PV Model by testing both techniques using a dataset of 27 patients. This test will provide a level of statistical power which allows a rigorous comparison of the PV Model and the Extended Sine Model for the purposes of minimising the impact of information loss on clinical decision making. This will help ascertain whether the computational efficiency of the Extended Sine Model justifies the extreme simplifications of the physiology.

Chapter 6

Trialling Prototype Decision Support Tools

6.1 Introduction

In the previous chapters, we have presented two different methods for reconstructing missing pulmonary vein recordings in clinic. In chapter 4 we presented a model driven approach based on the underlying electrophysiology. In contrast, chapter 5 presented a more data-driven approach that used an extended sine wave to model the activation times and then generated an electrical signal using the average of the neighbours. These methods were calibrated using pulmonary vein recordings from Bristol Heart Institute.

We demonstrated that it is possible to reconstruct pulmonary vein recordings that have been lost to poor contact. In this chapter, using a much larger dataset from a greater number of patients, we perform a more sophisticated statistical analysis of the reconstruction methods.

Firstly, we compare how well the methods fit to clean data for which all spikes are visible, simply to compare the accuracy of which the phenomenology on the lasso catheter (specifically the activation times) is reproduced. The remainder of the chapter focuses on the reconstruction problem.

Secondly, we perform statistical analysis on the error on the active channels compared to the missing ones. If we find a strong correlation between the error on the active channels and the missing ones, we can accurately predict to what level of accuracy our reconstruction is valid, which is potentially valuable information if the reconstruction is to be used to inform clinical decision making.

Finally, explore both methods on this larger dataset. Where previously with $n = 3$ patients we could only look at the results case by case, with a larger dataset we can employ more sophisticated statistical analysis to compare the decision making with the removed and reconstructed data.

6.2   Methods

6.2.1   Mathematical Models

The mathematical models used to represent the phenomenology of the PV recordings are the same as those discussed in the previous chapters. From here on 'PV Model' refers to the work in chapter 4, in which a reaction diffusion equation solved on a cylindrical domain was used to represent the wavefront propagating through an ablated lesion during ablation. 'Extended Sine Model' refers to the extension of Weber's Sine Model presented in chapter 5, which reproduces the activation time pattern on the recording catheter without modelling the underlying electrophysiology.

6.2.2   Data Collection

For comparison between the two models 27 PV recordings were collected from adult male and female subjects with both paroxysmal and persistent atrial fibrillation undergoing pulmonary vein isolation therapy at Bristol Heart Institute. Bipolar recordings were obtained from a deflectable, circular, 20-pole Lasso catheter (Biosense Webster Ltd). These signals were collected under the supervision of an experienced cardiac technician who helped to identify the epochs of interest.

As in previous chapters, all data were appropriately anonymised prior to their use in this study. Under United Kingdom law, patient data collected during normal clinical routine and anonymised before research use may be used for research without additional consent.

6.2.3   Assessing Influence on Decision Making

As previously, we tested the influence of the presented techniques on clinical decision-making by presenting modified recordings for each of the 27 patients to a cardiologist experienced in the procedure of CPVI and recording their choice of ablation target. Signals were presented as follows: A) the original signal, B) the signal with channels removed

to simulate information loss, C) the removed channels reconstructed using the PV model and D) the removed channels reconstructed using the extended sine model. The original signals were presented to the cardiologist twice to examine inherent variation in the decision-making process.

For case B, as some recordings contained a high level of noise during periods of inactivity, replacing them with a zero time trace as in chapter 4 led to recordings that looked very artificial, with the active channels keeping their residual noise and the inactive ones modelled by perfectly flat line. We improved this aspect of the test by using a wavelet denoising algorithm to 'designal' the time trace, such that the removed recording is left with the same amplitude of noise that was in the original recording. This better simulates the effect of lost information than a zero time trace.

The 135 recordings (5 cases from 27 patients) were presented to the cardiologist in a random order. For some recordings, signals were inferred to be 'far field' signals by the cardiologist, meaning the electrodes were picking up distant activity from elsewhere in the heart. If the signal is truly far field, this would have been determined by the body surface ECG spiking simultaneously with the PV recording. To avoid such technicalities affecting results, we perform all statistical analyses on $N = 23$ patients.

Clinical decision making in each case was compared with the decision made with the complete information. We quantify 'error' in terms of the number of channels the decision made was away from the original decision. e.g. if channel PV 3-4 was identified as a target on the original recording, and the neighbouring channel PV 5-6 was targeted with the model, that corresponds to an error of 1. In rare instances the cardiologist identified two neighbouring channels when the earliest activation time was unclear. In these cases, an average point was used. If the modified signal was identified as far field, an error of 5 was recorded.

6.3   Results

6.3.1   Complete Data Fits

Firstly we investigate the capacity of both the PV Model and the Extended Sine Model to reproduce the activity on the recording catheter in the ideal setting in which all 10 channels are active. Relative activation time curves in both models were normalised so that the errors can be easily compared. We find a very similar error in both models. The

mean error across all 23 patients were 0.1247 (SD = 0.0626) in the PV model and 0.1238 (SD = 0.0573) in the Extended Sine Model. Boxplots showing the distributions of the errors in both models are displayed in Figure 6.1.

Figure 6.1: **Boxplots of Error Distributions in PV Model and Extended Sine Model.** Boxplots showing the distribution of the root mean squared error in activation times of pulmonary vein recordings from complete PV recordings from 23 different patients. There was no statistically significant difference in the error distributions of the two models ($p = 0.9515$).

From the boxplots displayed it is clear that both models have a similar median in error. To further explore the relationship between errors, Figure 6.2 displays each data displays error in both models for a particular patient as a single data point. There was a strong positive correlation between the errors in both models ($r = 0.8314$, $p = 8.89 \times 10^{-7}$). Upper and lower bounds for r for a 95% confidence interval are $[0.6378, 0.9262]$. This correlation implies that both models either fit or don't fit equally well to the same patients.

As data is clearly paired (from the strong correlation) we use the Wilcoxon signed rank test to determine if there is any statistically significant difference in the distributions. The test returned a significance value of $p = 0.9515$, giving very strong evidence that there is no statistically significant difference in the medians of the errors in both models. In summary, there is very little difference in the quality of fit of either model to the relative activation time curve of a complete PV recording.
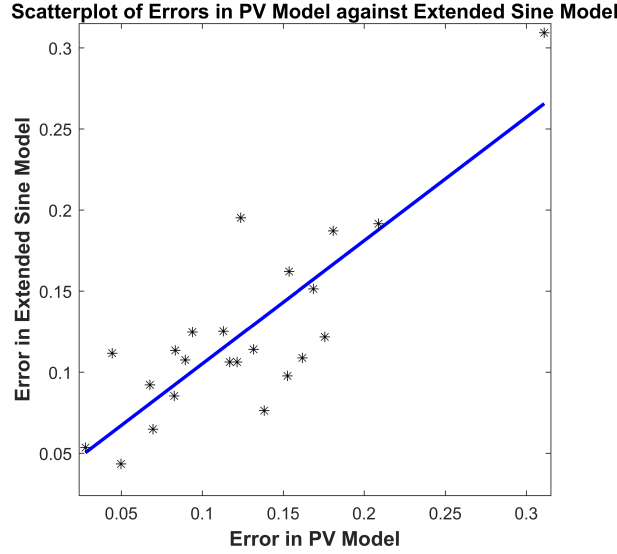
Figure 6.2: **Scatterplot of Errors in PV Model against Extended Sine Model.** This scatteplot shows the error in both models for each patient in the study, with line of best fit in blue. The strong positive correlation ($r = 0.8314$) shows that the errors are similar in each model for each individual, not just across the entire group.

6.3.2 Signal Reconstruction

The previous section indicated that there was no statistically significant difference in the quality of fit of either model when trained to complete signals. In this section we investigate the relative errors in the model when applied to reconstruct signals missing in the operating theatre. For each of the 23 patients, 3 channels (those inferred to be the most likely a clinician would first attempt to ablate) were removed from the recording. Both models were trained using only the remaining 7 channels. Error was calculated across all 10 channels, giving the results displayed in the box plots in Figure 6.3.

The mean error in the PV model was 0.2158 (SD = 0.1133) and in the Extended Sine Model was 0.1912 (SD = 0.1182). As previously, we used the Wilcoxon signed rank test to test for any significant differences in the medians of both distributions. The Wilcoxon signed rank test returned a significance value of $p = 0.3615$, implying no statistically significant conclusions one way or the other. We repeated the computation using the Mann-Whitney test (which does not rely on the data being paired) and arrived at a similar conclusion ($p = 0.2625$).

We also calculate the correlation between the errors on the 7 visible channels and the 10 in the complete recording. The relationship between these errors has the clinical relevance of being able to predict how accurate the reconstruction will be. A strong cor-
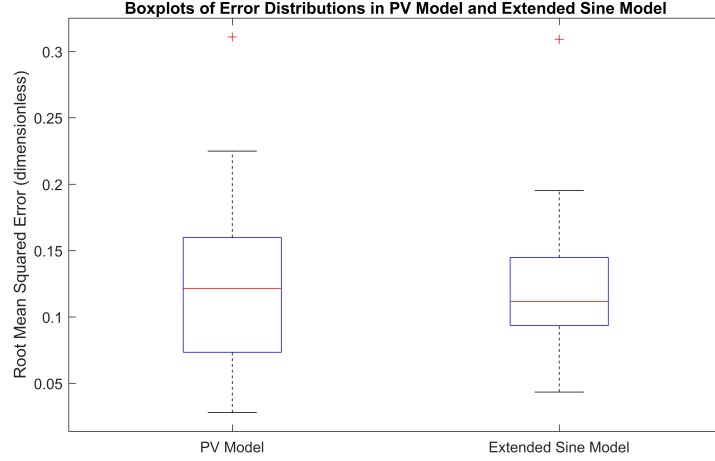
121

Figure 6.3: **Boxplots of Error Distributions in PV Model and Extended Sine Model.** Boxplots showing the distribution of the root mean squared error in activation times across PV recordings from 23 patients, with 3 channels reconstructed PV Model and by the Extended Sine Model. There was no statistically significant difference in the error distributions of the two models ($p = 0.3615$).

relation would imply that the quality of fit on the 7 active channels is a good predictor of the quality of fit across the entire recording.

In Figure 6.4 we present scatterplots of the error on the visible channels against the error across the whole recording for both the PV model and the Extended Sine Model. A weak positive correlation is present in both plots, with $r = 0.5115$ ($p = 0.0126$) for the PV model and $r = 0.4768$ ($p = 0.0214$) for the Extended Sine Model. The 95% confidence intervals for r were $[0.1258, 0.7628]$ and $[0.0805, 0.7430]$. While the PV model had a stronger and more significant correlation than the Extended Sine Model, there is significant overlap in the 95% confidence intervals.

6.3.3 Influence on Clinical Decision Making

This subsection analyses the influence that the described techniques have on the decision of a clinician. Decisions were recorded with reconstructed data from the PV Model, the Extended Sine Model, and with channels removed. Further, decisions were recorded twice on the original recording. To avoid sensitivity to which of the two 'original' decisions we use as our ground truth, we compare decision made with the mean of the decisions made when faced with the original recording.

(a) PV Model   (b) Extended Sine Model
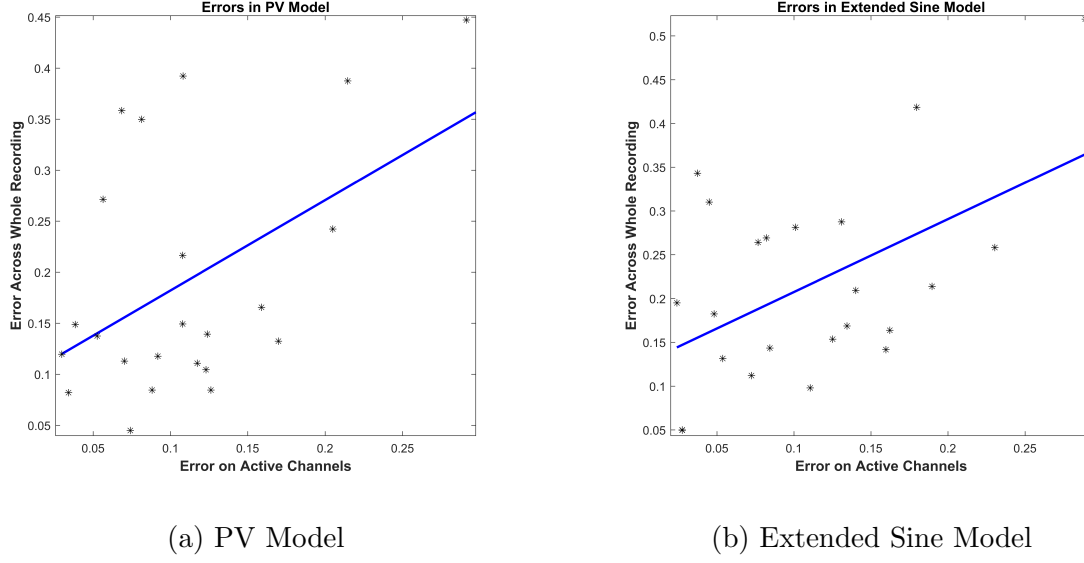
Figure 6.4: **Scatterplots showing Correlation between Error on Active Channels and Error across Whole Recording.** These scatterplots show the connection between how well the models fit to the active channels and how well the resulting fit is to the whole signal. a) results from the PV model ($r = 0.5115$). b) results from the Extended Sine Model ($r = 0.4768$). Correlation is not strong enough for the error across the whole recording to be reliably predicted from the error on the active channels for either model.

Figure 6.5 shows the error in clinical decision making using the signals with removed channels, channels reconstructed by the PV Model and channels reconstructed by the Extended Sine Model. Full results are provided in a table in Appendix C.

From the histograms it is clear that both models reduced the error in clinical decision making. The mean error with removed channels was 2.2065 channels (SD = 1.4512), compared to an error of 1.4239 (SD = 1.0804) with the PV model and an error of 1.5543 (SD = 1.3734) with the extended sine model. Using the extended sine model resulted in the highest frequency of perfect decisions, but also a large number of severe errors, resulting in the high SD reported. Error in decision-making is shown in the histograms in Figure 6.5. For 15/23 (65%) of patients, the clinician's decision was consistent when presented with the same recording twice, giving a mean error of 0.9348 (SD = 1.4640). As this is the variation from testing the clinician against himself, this mean error represents the best that could be reasonably expected from our reconstruction efforts.

As each sample is performed on the same ectopic event with the same signals removed, and the data is clearly not normally distributed, the Wilcoxon signed-rank test was used to compare the medians. The assumption that the PV Model and Extended Sine Model

123
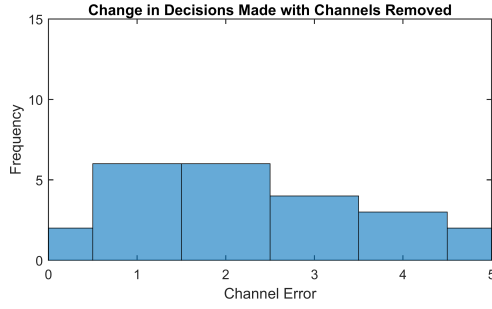
(a) Error in Decision Making with Channels Removed to simulate lost information
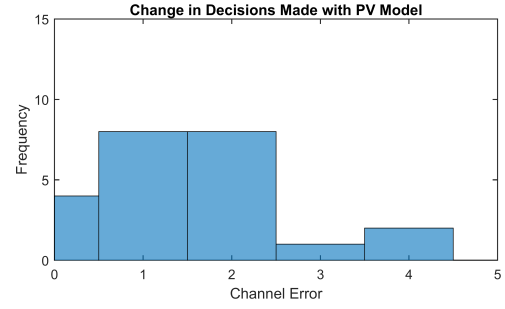
(b) Error in Decision Making with Channels Reconstructed by the PV Model
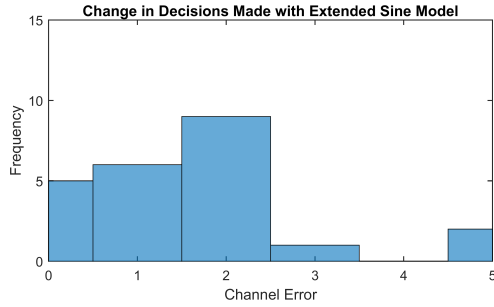
(c) Error in Decision Making with Channels Reconstructed by the Extended Sine Model
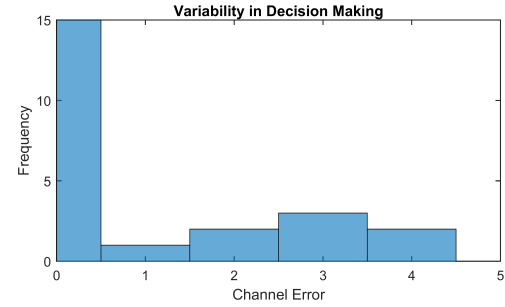
(d) Variability in Decision Making on the same clinical signal

Figure 6.5: **Histograms Showing Error in Clinical Decision Making.** Histograms presented show the error in clinical decision making with a) channels removed, b) reconstructed by a mathematical model of the elecrophysiology and c) by a data driven approach using an extended sine wave. d) shows the variability present in the decision process. The decisions made with the PV Model and with Extended Sine Model were both significantly better than the decisions made with the channels removed ($p = 0.0083$ and 0.0255 respectively).

reconstructions are paired is further justified by the correlation shown in Figure 6.2. The Mann-Whitney test was used to find whether the decision change from the reconstruction was significantly larger than the error inherent in the decision making process.

The PV model provided a significant improvement in decision making over the removed channels ($p = 0.0083$). The Extended Sine Model also provided a statistically significant improvement over having no information ($p = 0.0255$). The errors made when using the PV Model were indistinguishable from the errors made using the Extended Sine Model ($p = 0.7520$).

6.4 Discussion

This chapter used a larger dataset of 27 patients to compare the PV Model and the Extended Sine Model. Following extensive testing considering a variety of factors, we found both models to be equally effective.

When performing fits on complete recordings, a statistically significant result to the 5% confidence level indicated that the models fit to the same degree of accuracy. When using the same test to compare how errors increase when using the models to reconstruct data, the Extended Sine Model had a lower mean, but this was not significant. Interestingly, we found a strong correlation between quality of fit between PV Model and Extended Sine Model when comparing individual patients.

This implies that the models struggle to fit to the same patients, and it is not possible to predict which model will perform better for a given patient before the fit. The error in the active channels on the PV Model provided a slightly better correlation coefficient with which the error on reconstructed signals could be predicted, but this was not significantly different from that of the Extended Sine Model, and too weak to make a reliable prediction anyway.

The similarity between the two models persists when investigating influence on clinical decision making. We find that both models offer a significant improvement over leaving the recording with missing channels, as is presently done in clinic. This is a very positive result, as it shows that over 23 patients, both of the models that we have presented in this thesis improve clinical decision making to the 5% confidence level.

From the point of view of implementation more concrete comparisons can be made

between the two methods with the knowledge that they are are effectively the same in providing decision support. The Extended Sine Model is much quicker to compute due to the avoidance of a reaction diffusion equation that needs to be time-stepped on a high-resolution domain. This speed-up in computation time, which as established in chapter 5 is between 8 and 9 orders of magnitude, is especially important when calibrating the model to fit a patient in real time. Using present technology and without the use of any high performance computing facilities, the information collected indicates reconstruction of missing signals by the Extended Sine Model may be the most appropriate in clinic.

However, the Extended Sine Model contains no biological detail and as a result is difficult to extend to adapt to new technology. There are many factors which we *theoretically* could account for in the PV model, but did not as they were not routinely collected in clinic, and unavailable to us. These include fibre orientation in the heart, areas of inhomogeneous conduction velocity, and the geometrical mesh of the heart. The PV model could potentially adapt to this information if it was recorded in clinic.

Chapter 7

Discussion

From diagnosis, to drug discovery, to signal processing, mathematical modelling is a valuable tool in the research of cardiac disease. Exploration of the parameter space of detailed biophysical models, such as the Courtemanche model, has helped to identify ionic current channel targets for drug development. Investigation of a mathematical model rather than a real cell allows for a greater amount of cell properties down to the individual ion channels to be investigated simply by changing parameters. Mathematical models have also been developed to diagnose diseases across the cardiac system from sinoatrial node dysfunction to ventricular fibrillation, often producing a simulation of the body-surface ECG taking into account the conductivity of the torso. In radiofrequency ablation of atrial fibrillation, various ablation strategies have been compared for their efficiency in eliminating spiral waves through mathematical simulations of the underlying dynamics.

7.1   Discussion of Results

In this thesis we have focused on developing phenomenological mathematical models which could potentially be computed in real time in the operating theatre to aid a cardiologist's decision-making process. In chapter 3 we demonstrated new techniques to investigate the parameter space of a cardiac model, and calculated the pathway through parameter space connecting healthy and diseased states as a front of Pareto optimal solutions used the NSGA-II method. Having characterised this, then the main focus of the remainder of the thesis was to explore translational potential. We developed a novel mathematical model the PV electrophysiology, focusing on recordings of the electrical signal recorded around the PV ostium used to guide ablation, for which no model previously existed. We then used the model to address information loss issues arising from poor electrode contact.

7.1.1 Parameter Optimisation

Chapter 3 explored parameter optimisation strategies applied to cardiac models with two main aims. The first was to investigate a novel, alternative cost function to increase the efficiency of fitting a travelling action potential to data. The second was to find a path through parameter space linking healthy and disease states, in order to identify the key parameters involved.

Our proposed alternate cost function was to maximise the cross-correlation rather than minimise the mean squared error between the two action potentials. However, while we demonstrated that there are regions of parameter space for which this cost function is more representative of the actual error, the cost function performed poorly when performing actual parameter fits, as the region of parameter space with a notable improvement was simply not explored by either the NMSS or the GA.

We then explored paths through parameter space from a healthy cell to a diseased cell using a Pareto Front. We found that using a Pareto Front allowed for a significant increase in accuracy across the transition, compared to fitting to the two states and interpolating. In addition, parameter change across the front can help us to identify which parameters are of most importance based on how much they change across the front.

The parameter change identified caused a reduction in the slow inwards channel, reducing the APD and size of the dome morphology. This change is consistent with what we know about the physiological changes underpinning electrical remodelling in AF, as the morphological changes are largely caused by a reduction in the slow inwards Calcium leak current.

Simplifying the front by reducing it down to the line of best fit through the most important parameter still provided an improvement on linear interpolation across all 20. This simultaneous reduction of dimensionality and increase in accuracy allows for a much simpler representation of the transition which could potentially be useful for further mathematical analysis, such as bifurcation theory, on the key parameter identified.

7.1.2 Pulmonary Vein Model

Chapter 4 presented the key result of the thesis: the development of a novel phenomenological model of the pulmonary veins during radiofrequency ablation therapy capable of reproducing key features of the clinical PV recordings. To my knowledge, these record-

ings, despite being commonly used across the world during pulmonary vein ablation, had never been studied using a mathematical model before. Using a simple geometrical domain and a phenomenological reaction diffusion equation, we were able to reproduce the phenomenology of the recording catheter.

Due to the translational nature of this thesis, we investigated the use of the model in clinic by focusing on a common problem seen in the operating theatre: that some channels do not spike properly due to poor contact between electrode and tissue. We demonstrated that we could train the model to those channels that are spiking correctly, and simulate the model to reproduce those that are not. The RMS error in activation times was not significantly increased for up to three signals reconstructed, indicating that in clinic, we would be able to reconstruct up to three signals lost to poor contact.

We further investigated the potential applicability of the model in clinic by running a study using historic data, in which original signals were modified to reproduce the effect of information loss due to poor contact, and asking a cardiologist trained in the ablation procedure to identify where he would ablate. The study showed two key results: firstly that the loss of information does change the clinical cardiologist's decision on where to ablate, and secondly, that using the model reduces the impact of the information loss on the decision.

7.1.3 Data-Driven Method

In chapter 5 we introduced an alternative method for reconstructing clinical signals, by directly modelling the activation pattern without recourse to modelling the electrophysiology of the pulmonary vein. We build on existing work which fit a simple sine wave to the activation pattern of the lasso catheter for the purpose of estimating conduction velocity and fibre orientation in the atrium. We adapted this model to make it suitable to reproduce the activation time pattern when the lasso catheter is positioned around the pulmonary vein ostium by adding two extra parameters and demonstrated the improvement this development offers over the existing model.

Using a sine wave to model the activation pattern offers significant speed-up over using a reaction diffusion equation, however, this increase in computational efficiency comes with a decrease in realism, by only modelling the activation times we do not generate a synthetic signal. We show that using the simplified sine wave model, we can still reconstruct missing channels by taking averages of the channels of those which are spiking, and shifting the signals such that the activation time is in accordance with model predictions.

The methods presented in this chapter are much simpler than in chapter 4 but are not built on any electrophysiological principles. If such a method would be sufficient for providing an improvement in the operating theatre, it would be simpler and quicker to implement.

7.1.4 Clinical Testing

In chapter 6 we compare the methods introduced in chapters 4 and 5 using a larger dataset from Bristol Heart Institute with 27 patients. We compared the models numerically and in terms of the efficacy of a decision support system by repeating the clinical trial.

In terms of the effectiveness of the model to both fit to complete PV recordings, reconstruct data, and direct clinical decision making, there was very little difference between the PV Model and the Extended Sine Model. All statistical tests either returned an insignificant p value or returned a strongly significant result suggesting the models were identical. We also found that both the PV Model and the Extended Sine Model were strongly correlated in terms of which patients they gave the best fits for.

As both models were indistinguishable statistically, the most appropriate tool for the guidance of clinical decision is the one that can be computed the quickest: the Extended Sine Model, for which parameters can be calibrated in under a second. In the future, should an improvement in clinical data collection enable factors such as fibre orientation to be recorded, these can be easily included in the PV Model by adaptation of the numerical methods. In short, we conclude that the Extended Sine Model is more appropriate under the current state of the art, but the PV Model is adaptable to future advances in clinical monitoring.

7.2 Future Research

7.2.1 Paths Through Parameter Space

The result that following a Pareto Front through parameter space provides an improvement over interpolating is an interesting result and has broader implications outside of the scope of cardiac modelling. The result that a Pareto Front can pick up the nonlinear parameter changes in the BOCF model necessary to replicate the linear change in the Courtemanche model parameters could potentially be explored in future work.

More validation, using different combinations of models and even experimental validation, would be necessary before we can conclusively say that the technique is applicable to other problems. Subsequently, this technique could potentially be useful in any scientific problem where two states are known, but a simulation is required of the intermediate states.

The most significant potential application of our use of the Pareto Front comes from the ability to identify key parameters across the transition between states. Applied to other problems where parameters have a more well defined physical meaning (such as a biophysical cardiac model) it could potentially be possible to learn more about physiological changes at the subcellular level by observing how biophysical parameters change across the front.

7.2.2 Conduction Gap Detection

This thesis has focused primarily on building a mathematical model reconstruct of missing signals in the operating theatre, providing the cardiologist with more reliable information to make the decision on where to ablate. However, such an implementation still relies on the intuition of the clinician once the reconstructed signal is simulated. The most obvious development on this would be to extend the model to the degree of realism to which the optimal ablation location could be directly inferred. Such a technique could revolutionise the way the optimal ablation zone is determined by allowing a mathematical model built on the underlying biophysics to determine the most likely conduction gap location, rather than relying on intuition.

A number of additional steps would need to be taken to realise this idea. The assumption of isotropy, while sufficient for reconstructing signals, would alter the optimised location of the conduction gap, and as such, the accuracy of which the conduction gap could be estimated would be dependent on the accuracy of the diffusion tensor. The geometry of the heart and regions of tissue expansion between the ablation line and the recording catheter would also become more relevant when we are trying to work from the catheter back to the conduction gap location.

In order for such a technique to be implemented, we would ideally require the fibre orientation to infer the eigenvectors of the diffusion tensor, coupled with a 3D mesh model of the patient's pulmonary vein ostium to perform finite element simulations. While the 3D mesh is recorded within the Carto software commonplace in the operating theatre, dominant conduction direction is not recorded in standard clinical practice. As a result,

any integration of a model requiring these properties into a therapeutic decision support system would require the introduction of additional recording technology, which is outside the scope of this thesis.

7.2.3 Integration into Clinical Practice

The model presented is sufficient to reconstruct missing recordings. However, the procedure requires parameter optimisation (the location and size of conduction gaps) to train the model to the signals that aren't spiking, in order to simulate the others. The vast majority of the computation time is spent training the model so that the missing signals can be simulated. The computation time is exacerbated by the inefficiency of general purpose optimisers such as the GA or NMSS. As the parameters being optimised are integers within a certain range, there are only a finite number of parameter choices, and current implementations of general purpose optimisation techniques tend to repeat the same calculations.

It is likely the most efficient optimisation technique will come from a bespoke algorithm developed specifically for the purpose, rather than a general method such as the GA or the NMSS. If such an optimisation scheme is developed, the model would be ready for clinical use, and future work should be directed towards this aim to make the system as easy and intuitive as possible for the clinical cardiologist to integrate into existing practice.

This would involve the further pursuit of our patent application which outlines and protects the IP on clinically relevant techniques [195]. While the clinical cardiologists involved in the work at Bristol Heart Institute and the University Hospital of Bordeaux expressed interest in the tools developed in the thesis, further investigation would need to be undertaken to assess the global interest in our proposed decision support system among the clinical community. From there, the system would need to be developed on the technical side, either integrated as a feature in existing software (such as Boston-Scientific's LabSystem Pro currently used to analyse signals) or as a standalone software package. Next, a large scale, formal clinical trial would be necessary to test the system during the live procedure, rather than retrospectively on past cases, before it is ready for widespread adoption by the clinical community.

Appendix A

Courtemanche Model Equations

$$\dot{V} = -(i_{Na} + i_{K1} + i_{to} + i_{Kur} + i_{Kr} + i_{Ks} + i_{B_{Na}} + i_{B_{Ca}} + i_{NaK} + i_{Ca_P} + i_{NaCa} + i_{Ca_L} + i_{st})/Cm$$

$$i_{Na} = Cm \cdot g_{Na} \cdot m^3 \cdot h \cdot j(V - E_{Na})$$

$$E_{Na} = (R \cdot T/F)\ln(Na_o/Na_i)$$

$$\alpha_m = \begin{cases} V = -47.13 & 3.2 \\ \text{else} & 0.32(V + 47.13)/(1 - \exp(-0.1(V + 47.13))) \end{cases}$$

$$\beta_m = 0.08\exp(-V/11)$$

$$m_\infty = \alpha_m/(\alpha_m + \beta_m)$$

$$\tau_m = 1/(\alpha_m + \beta_m)$$

$$\dot{m} = (m_\infty - m)/\tau_m$$

$$\alpha_h = \begin{cases} V < -40 & 0.135\exp(-(V + 80)/6.8) \\ \text{else} & 0 \end{cases}$$

$$\beta_h = \begin{cases} V < -40 & 3.56\exp(0.079V) + 3.1 \times 10^5\exp(0.35 * V) \\ \text{else} & 1/(0.13(1 + \exp(-(V + 10.66)/11.1))) \end{cases}$$

$$h_\infty = \alpha_h/(\alpha_h + \beta_h)$$

$$\tau_h = 1/(\alpha_h + \beta_h)$$

$$\dot{h} = (h_\infty - h)/\tau_h$$

$$\alpha_j = \begin{cases} V < -40 & \frac{(-1.2714 \times 10^5\exp(0.2444V) - 3.474 \times 10^{-5}\exp(-0.04391V))(V + 37.78)}{(1 + \exp(0.311(V + 79.23)))} \\ \text{else} & 0 \end{cases}$$

$$\beta_j = \begin{cases} V < -40 & \frac{0.1212 * \exp(-0.01052V)}{(1 + \exp(-0.1378(V + 40.14)))} \\ \text{else} & \frac{0.3 * \exp(-2.535 \times 10^{-7} * V)}{(1 + \exp(-0.1(V + 32)))} \end{cases}$$

$$\tag{A.1}$$

$$j_\infty = \alpha_j/(\alpha_j + \beta_j)$$

$$\tau_j = 1/(\alpha_j + \beta_j)$$

$$\dot{j} = (j_\infty - j)/\tau_j$$

$$E_K = (R \cdot T/F)\ln(K_o/K_i)$$

$$i_{K1} = \frac{Cm \cdot g_{K1}(V - E_K)}{(1 + \exp(0.07 * (V + 80)))}$$

$$i_{to} = Cm \cdot g_{to} \cdot oa^3 \cdot oi(V - E_K)$$

$$\alpha_{oi} = (18.53 + \exp((V + 113.7)/10.95))^{-1}$$

$$\beta_{oi} = (35.56 + \exp(-(V + 1.26)/7.44))^{-1}$$

$$\tau_{oi} = (\alpha_{oi} + \beta_{oi})^{-1}/K_Q 10$$

$$oi_\infty = (1 + \exp((V + 43.1)/5.3))^{-1}$$

$$\dot{oi} = (oi_\infty - oi)/\tau_{oi}$$

$$g_{Kur} = 0.005 + 0.05/(1 + \exp((15 - V)/13))$$

$$i_{Kur} = Cm \cdot g_{Kur} \cdot ua^3 \cdot ui \cdot (V - E_K)$$

$$\alpha_{ua} = 0.65(\exp(-(V + 10)/8.5) + \exp((30 - V)/59))^{-1}$$

$$\beta_{ua} = 0.65(2.5 + \exp((V + 82)/17))^{-1}$$

$$\tau_{ua} = (\alpha_{ua} + \beta_{ua})^{-1}/K_Q 10 \tag{A.2}$$

$$ua_\infty = (1 + \exp(-(V + 30.3)/9.6))^{-1}$$

$$\dot{ia} = (ua_\infty - ua)/\tau_{ua}$$

$$\alpha_{ui} = (21 + \exp((185 - V)/28))^{-1}$$

$$\beta_{ui} = 1/\exp((158 - V)/16)$$

$$\tau_{ui} = (\alpha_{ui} + \beta_{ui})^{-1}/K_Q 10$$

$$ui_\infty = (1 + \exp((V - 99.45)/27.48))^{-1}$$

$$\dot{ui} = (ui_\infty - ui)/\tau_{ui}$$

$$i_{Kr} = \frac{Cm \cdot g_{Kr} \cdot xr(V - E_K)}{1 + \exp((V + 15)/22.4)}$$

$$\alpha_{xr} = \begin{cases} \text{abs}(V + 14.1) < 10^{-10} & 0.0015 \\ \text{else} & \frac{0.0003(V+14.1)}{1-\exp(-(V+14.1)/5)} \end{cases}$$

$$\beta_{xr} = \begin{cases} \text{abs}(V - 3.3328) < 10^{-10} & 3.7836118 \times 10^{-4} \\ \text{else} & \frac{7.3898\times10^{-5}(V-3.3328)}{\exp((V-3.3328)/5.1237)-1} \end{cases}$$

$$\tau_{xr} = (\alpha_{xr} + \beta_{xr})^{-1}$$

$$xr_\infty = (1 + \exp(-(V + 14.1)/6.5))^{-1}$$

$$\dot{xr} = (xr_\infty - xr)/\tau_{xr}$$

$$i_{Ks} = Cm \cdot g_{Ks} \cdot xs^2(V - E_K)$$

$$\alpha_{xs} = \begin{cases} \text{abs}(V - 19.9) < 1 \times 10^{-10} & 6.8 \times 10^{-4} \\ \text{else} & \frac{4 \times 10^{-5}(V-19.9)}{(1-\exp((19.9-V)/17))} \end{cases}$$

$$\beta_{xs} = \begin{cases} \text{abs}(V - 19.9) < 1 \times 10^{-10} & 3.15 \times 10^{-4} \\ \text{else} & \frac{3.5 \times 10^{-4}(V-19.9)}{(\exp((V-19.9)/9)-1)} \end{cases}$$

$$\tau_{xs} = 0.5(\alpha_{xs} + \beta_{xs})^{-1}$$

$$xs_\infty = \left(\frac{1 + \exp((19.9 - V))}{12.7} \right)^{-0.5}$$

$$\dot{xs} = (xs_\infty - xs)/\tau_{xs}$$

$$i_{Ca_L} = Cm \cdot g_{Ca_L} \cdot d \cdot f \cdot f_{Ca}(V - 65)$$

$$d_\infty = (1 + \exp(-(V + 10)/8))^{-1}$$

$$\tau_d = \begin{cases} \text{abs}(V + 10) < 1 \times 10^{-10} & \frac{4.579}{1+\exp(-(V+10)/6.24)} \\ \text{else} & \frac{1-\exp((V+10)/-(6.24))}{0.035*(V+10)*(1+\exp(-(V+10)/6.24))} \end{cases}$$

$$\dot{d} = (d_\infty - d)/\tau_d$$

$$f_\infty = \frac{\exp(-((V + 28))/6.9)}{1 + \exp(-(V + 28)/6.9)}$$

$$\tau_f = 9(0.0197 \exp(-((0.0337)^2)(V + 10)^2) + 0.02)^{-1}$$

$$\dot{f} = (f_\infty - f)/\tau_f$$

$$f_{Ca_\infty} = (1 + Ca_i/0.00035)^{-1}$$

$$\dot{f_{Ca}} = (f_{Ca_\infty} - f_{Ca})/\tau_{f_{Ca}}$$

$$\sigma = (\exp(Na_o/67.3) - 1)/7$$

$$f_{NaK} = \left(1 + 0.1245 \exp\left(\frac{-0.1 \cdot F \cdot V}{R \cdot T} \right) + 0.0365\sigma \cdot \exp\left(\frac{-F \cdot V}{R \cdot T} \right) \right)^{-1}$$

$$i_{NaK} = \frac{Cm \cdot i_{NaK_{max}} \cdot f_{NaK}}{(1 + (Km_{Na_i}/Na_i)^{1.5})} K_o/(K_o + Km_{K_o})$$

$$E_{Ca} = R \cdot T/2F \ln(Ca_o/Ca_i)$$

$$i_{B_{Na}} = Cm \cdot g_{B_{Na}}(V - E_{Na})$$

$$i_{B_{Ca}} = Cm \cdot g_{B_{Ca}}(V - E_{Ca})$$

$$i_{B_K} = Cm \cdot g_{B_K}(V - E_K)$$

$$i_{NaCa} = Cm \cdot I_{NaCa_{max}} \frac{\left(\exp\left(\frac{\gamma \cdot F \cdot V}{R \cdot T} \right) * Na_i^3 \cdot Ca_o - \exp\left(\frac{(\gamma-1)F \cdot V}{R \cdot T} \right) Na_o^3 \cdot Ca_i \right)}{(K_m Na^3 + Na_o^3)(K_m Ca + Ca_o)\left(1 + K_{sat} * \exp\left(\frac{(\gamma-1)V \cdot F}{R \cdot T} \right) \right)}$$
$$\text{(A.3)}$$

$$i_{Ca}P = Cm \cdot i_{Ca} \cdot P_{max} \cdot Ca_i/(0.0005 + Ca_i)$$

$$Fn = 10^3 \left(10^{-15} V_{rel} \cdot i_{rel} - \frac{10^{-15}}{2F}(0.5 i_{Ca_L} - 0.2 i_{NaCa}) \right)$$

$$i_{rel} = K_{rel} \cdot u^2 \cdot v \cdot w(Ca_{rel} - Ca_i)$$

$$u_\infty = \left(1 + \exp\left(\frac{-(Fn - 3.4175 \times 10^{-13})}{13.67 \times 10^{-16}} \right) \right)^{-1}$$

$$\dot{u} = (u_\infty - u)/\tau_u$$

$$\tau_v = 1.91 + 2.09 \left(1 + \exp\left(\frac{-(Fn - 3.4175 \times 10^{-13})}{13.67 \times 10^{-16}} \right) \right)^{-1}$$

$$v_\infty = 1 - \left(1 + \exp\left(\frac{-(Fn - 6.835 \times 10^{-14})}{13.67 \times 10^{-16}} \right) \right)^{-1}$$

$$\dot{v} = (v_\infty - v)/\tau_v$$

$$\tau_w = \begin{cases} \text{abs}(V - 7.9) < 10^{-10} & 6 \times 0.2/1.3 \\ \text{else} & 6\frac{1-\exp(-(V-7.9)/5)}{(1+0.3\exp(-(V-7.9)/5))(V-7.9)} \end{cases}$$

$$w_\infty = 1 - (1 + \exp(-(V - 40)/17))^{-1}$$

$$\dot{w} = (w_\infty - w)/\tau_w$$

$$i_t r = (Ca_{up} - Ca_{rel})/\tau_t r$$

$$i_{up} = I_{up_{max}}/(1 + K_{up}/Ca_i) \tag{A.4}$$

$$i_{up_{leak}} = I_{up_{max}} * Ca_{up}/Ca_{up_{max}}$$

$$Ca_{CMDN} = CMDN_{max} \cdot Ca_i/(Ca_i + Km_{CMDN})$$

$$Ca_{TRPN} = TRPN_{max} \cdot Ca_i/(Ca_i + Km_{TRPN})$$

$$Ca_{CSQN} = CSQN_{max} \cdot Ca_{rel}/(Ca_{rel} + Km_{CSQN})$$

$$V_i = V_{cell} \cdot 0.68$$

$$V_{rel} = 0.0048 V_{cell}$$

$$V_{up} = 0.0552 V_{cell}$$

$$\dot{Na}_i = (-3 i_{NaK} - (3 i_{NaCa} + i_{B_{Na}} + i_{Na}))/(V_i \cdot F)$$

$$\dot{K}_i = (2 i_{NaK} - (i_{K1} + i_{to} + i_{Kur} + i_{Kr} + i_{Ks} + i_{B_K}))/(V_i \cdot F)$$

$$\dot{Ca}_i = B1/B2$$

$$B1 = \frac{2 i_{NaCa} - (i_{Ca}P + i_{Ca_L} + i_{BCa})}{2 V_i \cdot F} + \frac{V_{up}(i_{up_{leak}} - i_{up}) + i_{rel} \cdot V_{rel}}{V_i}$$

$$B2 = 1 + \frac{TRPN_{max} * Km_{TRPN}}{(Ca_i + Km_{TRPN})^2} + \frac{CMDN_{max} * Km_{CMDN}}{(Ca_i + Km_{CMDN})^2}$$

$$\dot{Ca}_{up} = i_{up} - (i_{up_{leak}} + i_{tr} \cdot V_{rel}/V_{up})$$

$$\dot{Ca}_{rel} = (i_{tr} - i_{rel}) \left(1 + \frac{CSQN_{max} \cdot Km_{CSQN}}{(Ca_{rel} + Km_{CSQN})^2} \right)^{-1}$$

Where any undefined symbols are constant parameters given in [4] or [11].

Appendix B

Derivation and Programming of the Asymmetric Finite Difference Stencil

This appendix describes the derivation of the 9 point finite difference stencil used in the calculation of anisotropic diffusion. The calculations are performed in 2 dimensions on a rectangular grid with spatial resolutions Δx and Δy, but could be scaled to any integer dimension ≥ 2. The stencil calculates an approximation for the diffusion term $\nabla \cdot (\tilde{D} \nabla u)$ in a generic reaction-diffusion equation where $\sum J_{\text{ion}}$ is the sum of all currents in the reaction part of the model (phenomenological or biophysical).

$$\frac{\partial u}{\partial t} = \nabla \cdot (\mathbf{D} \nabla u) + \sum J_{\text{ion}}, \tag{B.1}$$

where $\mathbf{D}$ is the diffusion tensor, which for isotropic diffusion can be treated as a constant. For anisotropic diffusion, we consider a unit direction vector $\mathbf{b} = (\cos \alpha, \sin \alpha)^{\mathrm{T}}$ to be pointing in the dominant direction of diffusion. Diffusion coefficients parallel and perpendicular to $\mathbf{b}$ are defined as $D_{\parallel}$ and $D_{\perp}$. The diffusion matrix $\mathbf{D} = (D_{\parallel} - D_{\perp})\mathbf{b}\mathbf{b}^{\mathrm{T}} + D_{\perp}\mathcal{I}$, such that

$$\mathbf{D} = \begin{pmatrix} D_{\parallel}b_1^2 + D_{\perp}b_2^2 & (D_{\parallel} - D_{\perp})b_1 b_2 \\ (D_{\parallel} - D_{\perp})b_1 b_2 & D_{\perp}b_1^2 + D_{\parallel}b_2^2 \end{pmatrix}. \tag{B.2}$$

To ensure no loss of generality, unless specifically mentioned, we assume that $D_{\parallel}$, $D_{\perp}$ and α are not constant. In theory, these quantities could be a function of time, of any of the state variables, of space, or even stochastic, so long as they can be numerically evaluated at any point on the domain for every time step.

As the finite difference stencil is independent of the reaction, it is sufficient to consider the heat equation

$$\frac{\partial u}{\partial t} = \nabla \cdot (\mathbf{D} \cdot \nabla u), \tag{B.3}$$

which we express as

$$\mathbf{q} = -\mathbf{D} \cdot \nabla u, \qquad \frac{\partial u}{\partial t} = -\nabla \cdot \mathbf{q}, \tag{B.4}$$

by expressing the bracketed term in (B.3) as $-\mathbf{q}$. From here, we use asymmetric finite differences to calculate the stencil used in our numerical methods. For these methods, the diffusion tensor is defined on the half indicies, i.e. for a generic point in the grid (i, j), the diffusion tensor $\mathbf{D}$ is defined on $(i \pm \frac{1}{2}, j)$ and $(i, j \pm \frac{1}{2})$. At any point (i, j), we calculate

$$\mathbf{q}_{i,j} = -\mathbf{D}_{i,j} \cdot \left(\left. \frac{\partial u}{\partial x} \right|_{i,j}, \left. \frac{\partial u}{\partial y} \right|_{i,j} \right). \tag{B.5}$$

However, as we define $\mathbf{D}$ on the half indices, we require $\mathbf{q}_{i \pm \frac{1}{2}, j}$ and $\mathbf{q}_{i, j \pm \frac{1}{2}}$, allowing us to use the central difference formula to calculate diffusion.

$$\nabla \cdot \mathbf{q} = \frac{(q_1)_{i+\frac{1}{2}, j} - (q_1)_{i-\frac{1}{2}, j}}{\Delta x} + \frac{(q_1)_{i, j+\frac{1}{2}} - (q_1)_{i, j-\frac{1}{2}}}{\Delta y} \tag{B.6}$$

Defining D on the half indicies is where the asymmetry comes from, as we must handle the x and y differentials differently on each point in the stencil. For $\mathbf{q}_{i+\frac{1}{2}, j}$, the x differential can be handled through the standard central difference formula:

$$\left. \frac{\partial u}{\partial x} \right|_{i+\frac{1}{2}, j} = \frac{u_{i+1,j} - u_{i,j}}{\Delta x}. \tag{B.7}$$

This, howver, does not apply to the y derivative as there is no change in y across these two grid points. To calculate $\left. \frac{\partial u}{\partial y} \right|_{i+\frac{1}{2}, j}$ we use a somewhat longer central difference formula, which calculates the average of the y derivative from $(i, j-1)$ to $(i, j+1)$ and $(i+1, j-1)$ to $(i+1, j+1)$ (a rectangle centred on $(i+\frac{1}{2}, j)$):

$$\left. \frac{\partial u}{\partial y} \right|_{i+\frac{1}{2}, j} = \frac{u_{i+1,j+1} + u_{i,j+1} - u_{i+1,j-1} - u_{i,j-1}}{4\Delta y}. \tag{B.8}$$

Applying equation (B.5) with spatial derivatives as in (B.7) and (B.8) at $(i + \frac{1}{2}, j)$ gives

$$\mathbf{q}_{i+\frac{1}{2},j} = -\begin{pmatrix} D_\parallel b_1^2 + D_\perp b_2^2 & (D_\parallel - D_\perp)b_1 b_2 \\ (D_\parallel - D_\perp)b_1 b_2 & D_\perp b_1^2 + D_\parallel b_2^2 \end{pmatrix}_{i+\frac{1}{2},j} \cdot \begin{pmatrix} \frac{u_{i+1,j}-u_{i,j}}{\Delta x} \\ \frac{u_{i+1,j+1}+u_{i,j+1}-u_{i+1,j-1}-u_{i,j-1}}{4\Delta y} \end{pmatrix} \quad \text{(B.9)}$$

which, defining the elements of $\mathbf{D}_{i+\frac{1}{2},j}$ as $D(1,1)_{i+\frac{1}{2},j}$, $D(1,2)_{i+\frac{1}{2},j}$, $D(2,1)_{i+\frac{1}{2},j}$, $D(2,2)_{i+\frac{1}{2},j}$, evaluates to

$$\mathbf{q}_{i+\frac{1}{2},j} = -\begin{pmatrix} D(1,1)_{i+\frac{1}{2},j}\frac{(u_{i+1,j}-u_{i,j})}{\Delta x} + D(1,2)_{i+\frac{1}{2},j}\frac{(u_{i+1,j+1}+u_{i,j+1}-u_{i+1,j-1}-u_{i,j-1})}{4\Delta y} \\ D(2,1)_{i+\frac{1}{2},j}\frac{(u_{i+1,j}-u_{i,j})}{\Delta x} + D(2,2)_{i+\frac{1}{2},j}\frac{(u_{i+1,j+1}+u_{i,j+1}-u_{i+1,j-1}-u_{i,j-1})}{4\Delta y} \end{pmatrix}. \quad \text{(B.10)}$$

Similar calculations can be performed on half-indices on the y axes to obtain

$$\mathbf{q}_{i,j+\frac{1}{2}} = -\begin{pmatrix} D(1,1)_{i,j+\frac{1}{2}}\frac{(u_{i+1,j+1}+u_{i+1,j}-u_{i-1,j+1}-u_{i-1,j})}{4\Delta x} + D(1,2)_{i,j+\frac{1}{2}}\frac{(u_{i+1,j}-u_{i,j})}{\Delta y} \\ D(2,1)_{i,j+\frac{1}{2}}\frac{(u_{i+1,j+1}+u_{i+1,j}-u_{i-1,j+1}-u_{i-1,j})}{4\Delta x} + D(2,2)_{i,j+\frac{1}{2}}\frac{(u_{i+1,j}-u_{i,j})}{\Delta y} \end{pmatrix}. \quad \text{(B.11)}$$

Diffusion can then be calculated by substituting equations (B.10) and (B.11) into (B.6). A number of simplifications can be made to simplify this large numerical scheme. Firstly, if the diffusion matrix $\mathbf{D}$ is constant across the domain, evaluation of (B.6) becomes much simpler. After some calculation we find

$$\nabla \cdot \mathbf{q} =$$
$$-\left(\frac{D(1,1)(u_{i+1,j}+u_{i-1,j}-2u_{i,j})}{\Delta x} + \frac{D(1,2)(u_{i+1,j+1}+u_{i-1,j-1}-(u_{i-1,j+1}+u_{i+1,j-1}))}{4\Delta y}\right)/\Delta x$$
$$-\left(\frac{D(2,1)(u_{i+1,j+1}+u_{i-1,j-1}-(u_{i-1,j+1}+u_{i+1,j-1}))}{4\Delta x} + \frac{D(2,2)(u_{i,j+1}+u_{i,j-1}-2u_{i,j})}{\Delta y}\right)/\Delta y$$
$$\text{(B.12)}$$

The terms with the leading diagonal of $\mathbf{D}$ as a coefficient are calculated through basic finite differences in the relevant direction. The backwards diagonal terms are given by the sum of the terms on opposite corners of the 9 points subtracted from the sum of the terms on the other corners. If $\Delta x = \Delta y = h$,

$$\nabla \cdot \mathbf{q} =$$

$$-\left(\frac{4D(1,1)(u_{i+1,j} + u_{i-1,j} - 2u_{i,j}) + D(1,2)(u_{i+1,j+1} + u_{i-1,j-1} - (u_{i-1,j+1} + u_{i+1,j-1}))}{4\Delta h^2} \right)$$

$$-\left(\frac{D(2,1)(u_{i+1,j+1} + u_{i-1,j-1} - (u_{i-1,j+1} + u_{i+1,j-1})) + 4D(2,2)(u_{i,j+1} + u_{i,j-1} - 2u_{i,j})}{\Delta 4 h^2} \right).$$

$$(B.13)$$

Further, if $\mathbf{D} = D\mathcal{I}$, equation (B.13) simplifies to the familiar formula for finite differences:

$$\nabla \cdot \mathbf{q} = -D \left(\frac{u_{i+1,j} + u_{i-1,j} + u_{i,j+1} + u_{i,j-1} - 4u_{i,j}}{h^2} \right). \qquad (B.14)$$

We calculate an efficient procedure for programming the computation of Equation (B.12) using an extended version of the technique given in the sample MATLAB scripts of [196], for which diffusion is isotropic, and the only boundary conditions considered are Neumann. We define vectors $\mathbf{N}$ and $\mathbf{S}$ which have the same length as Y, the number of nodes in the y axis. The elements of the vector $\mathbf{N}$ are defined as $N(i) = i + 1$, such that the elements of $\mathbf{N}$ point to the element above. $\mathbf{S}$ is defined similarly for points below. Boundary conditions are handled on $N(Y)$ and $S(1)$. Considering only diffusion in the y axis, using $N(Y) = Y$ as in [196] will give a scheme on the boundary of

$$\nabla \cdot \mathbf{q} = -D \left(\frac{u_{i,j-1} - u_{i,j}}{h^2} \right). \qquad (B.15)$$

on the upper boundary. Setting $N(Y) = 1$ will cause a periodic boundary condition. $\mathbf{N}$ and $\mathbf{S}$ stand for North and South. Similar vectors $\mathbf{E}$ and $\mathbf{W}$ can be defined for East and West. For isotropic diffusion we use the code from [196]:

```
E=[1 1:(size1-1)];
W=[2:size1 size1];
N=[1 1:(size2-1)];
S=[2:size2 size2];
spat=D.*(u(N,:)+u(S,:)+u(:,E)+u(:,W)-4*u)/(dx*dx).
```

For anisotropic diffusion with a tensor as defined in (B.2), we use the following:

```
spat=(D(1,1)*(u(N,:)+u(S,:)-2*u)+...
      D(2,2)*(u(:,E)+u(:,W)-2*u)+...
      D(1,2)*(u(N,E)+u(S,W)-u(S,E)-u(N,W))/4+...
      D(2,1)*(u(N,E)+u(S,W)-u(S,E)-u(N,W))/4);
```

Appendix C

Results of Large Clinical Test

This appendix chapter contains the full results of the clinical test used in chapter 6 to compare the ability of both the PV model and the data-driven sine model to reconstruct pulmonary vein recordings with missing signals for the purposes of aiding clinical decision making. Recordings for all 27 patients were collected at Bristol Heart Institute from routine clinical procedure and analysed by a cardiologist trained in the ablation procedure (who would have treated some of the patients in the first place). Signals were presented to the clinician in a random order to avoid any associations being made and subconsciously influencing the decision.

Patient	Original	Original 2	Removed	PV Model	Sine Model
1	PV 15-16	PV 9-10	PV 9-10	PV 13-14	PV 11-12
2	PV 15-16	FF	PV 15-16	FF	FF
3	PV 3-4	PV 15-16	PV 17-18	PV 17-18	PV 15-16
4	PV 5-6	PV 17-18	PV 17-18	PV 5-6	PV 17-18
5	PV 1-2	PV 1-2	PV 15-16	PV 17-18	PV 17-18
6	PV 11-12	PV 11-12	PV 13-14	PV 11-12	PV 11-12
7	PV 9-10	PV 10-11	PV 7-8	PV 9-10	PV 11-12
8	PV 15-16	PV 15-16	PV 7-8	PV 3-4	PV 19-20
9	PV 13-14	PV 13-14	PV 11-12	PV 13-14	PV 3-4
10	PV 3-4	PV 3-4	PV 1-2	PV 5-6	PV 5-6
11	PV 9-10	PV 13-14	PV 1-2	PV 11-12	PV 11-12
12	PV 7-8	PV 11-12	FF	PV 7-8	PV 3-4
13	PV 1-2	PV 15-16	PV 3-4	PV 15-16	PV 1-2
14	PV 11-12	PV 11-12	PV 1-2	PV 15-16	PV 1-2
15	PV 9-10	PV 9-10	PV 15-16	PV 11-12	PV 11-12
16	PV 15-16	PV 15-16	PV 15-16	PV 13-14	PV 13-14
17	PV 9-10	PV 9-10	PV 15-16	PV 11-12 / 13-14	PV 13-14
18	PV 3-4	PV 17-18	PV 19-20	PV 5-6	PV 17-18
19	PV 11-12	PV 11-12	PV 13-14	PV 15-16	PV 11-12
20	PV 7-8	PV 7-8	PV 19-20	PV 19-20	PV 7-8
21	PV 9-10	PV 9-10	PV 5-6	PV 11-12	PV 5-6
22	FF	FF	FF	FF	FF
23	PV 3-4	PV 3-4	PV 3-4	PV 3-4	PV 3-4
24	PV 11-12	FF	FF	FF	FF
25	FF	PV 15-16	FF	FF	FF
26	PV 11-12	PV 11-12	PV 13-14	PV 13-14	PV 13-14
27	PV 9-10	PV 9-10	PV 5-6	PV 7-8/9-10	PV 9-10

Table C.1: **Clinical Decision making with Doctored PV Recordings.** This table shows the full results of the clinical trial using past cases and recording a trained cardiologist's decision on optimal ablation location. 'Missing' shows the choice of ablation target when some channels were removed, simulating the effect of poor contact. 'EP Model' and 'Sine Model' are the choice of ablation target chosen when the removed channels are reconstructed by the methods described in chapters 4 and 5 respectively. 'Original' is the unedited signal with all channels spiking, showing the decision which would be made with all information present.

Bibliography

[1] Michael R Guevara and Leon Glass. Phase locking, period doubling bifurcations and chaos in a mathematical model of a periodically driven oscillator: a theory for the entrainment of biological oscillators and the generation of cardiac dysrhythmias. *Journal of mathematical biology*, 14(1):1–23, 1982.

[2] Krzysztof Grudziński and Jan J Żebrowski. Modeling cardiac pacemakers with relaxation oscillators. *Physica A: Statistical Mechanics and its Applications*, 336(1):153–162, 2004.

[3] WA Seed, MI Noble, P Oldershaw, RB Wanless, AJ Drake-Holland, D Redwood, S Pugh, and C Mills. Relation of human cardiac action potential duration to the interval between beats: implications for the validity of rate corrected qt interval (qtc). *British heart journal*, 57(1):32–37, 1987.

[4] Marc Courtemanche, Rafael J Ramirez, and Stanley Nattel. Ionic mechanisms underlying human atrial action potential properties: insights from a mathematical model. *American Journal of Physiology-Heart and Circulatory Physiology*, 275(1):H301–H321, 1998.

[5] Augustus O Grant. Cardiac ion channels. *Circulation: Arrhythmia and Electrophysiology*, 2(2):185–194, 2009.

[6] Luis F Santana, Edward P Cheng, and W Jonathan Lederer. How does the shape of the cardiac action potential control calcium signaling and contraction in the heart? *Journal of molecular and cellular cardiology*, 49(6):901, 2010.

[7] David E Euler. Cardiac alternans: mechanisms and pathophysiological significance. *Cardiovascular research*, 42(3):583–590, 1999.

[8] Colleen C Mitchell and David G Schaeffer. A two-current model for the dynamics of cardiac membrane. *Bulletin of mathematical biology*, 65(5):767–793, 2003.

[9] Cecilia W Lo. Role of gap junctions in cardiac conduction and development, 2000.

[10] Minki Hwang, Soon-Sung Kwon, Jin Wi, Mijin Park, Hyun-Seung Lee, Jin-Seo Park, Young-Seon Lee, Eun Bo Shim, and Hui-Nam Pak. Virtual ablation for atrial fibrillation in personalized in-silico three-dimensional left atrial modeling: Comparison with clinical catheter ablation. *Progress in biophysics and molecular biology*, 116(1):40–47, 2014.

[11] Marc Courtemanche, Rafael J Ramirez, and Stanley Nattel. Ionic targets for drug therapy and atrial fibrillation-induced electrical remodeling: insights from a mathematical model. *Cardiovascular research*, 42(2):477–489, 1999.

[12] Guanrong Chen. *Controlling chaos and bifurcations in engineering systems*. CRC press, 1999.

[13] Martin Lagerholm, Carsten Peterson, Guido Braccini, Lars Edenbrandt, and Leif Sornmo. Clustering ecg complexes using hermite functions and self-organizing maps. *IEEE Transactions on Biomedical Engineering*, 47(7):838–848, 2000.

[14] Richard FitzHugh. Impulses and physiological states in theoretical models of nerve membrane. *Biophysical journal*, 1(6):445, 1961.

[15] RH Clayton, Olivier Bernus, EM Cherry, Hans Dierckx, FH Fenton, L Mirabella, AV Panfilov, FB Sachse, G Seemann, and H Zhang. Models of cardiac tissue electrophysiology: progress, challenges and open questions. *Progress in biophysics and molecular biology*, 104(1):22–48, 2011.

[16] Balth Van der Pol. Lxxxviii. on "relaxation-oscillations". *The London, Edinburgh, and Dublin Philosophical Magazine and Journal of Science*, 2(11):978–992, 1926.

[17] Patrick E McSharry, Gari D Clifford, Lionel Tarassenko, and Leonard A Smith. A dynamical model for generating synthetic electrocardiogram signals. *IEEE Transactions on Biomedical Engineering*, 50(3):289–294, 2003.

[18] Muriel Boulakia, Serge Cazeau, Miguel A Fernández, Jean-Frédéric Gerbeau, and Nejib Zemzemi. Mathematical modeling of electrocardiograms: a numerical study. *Annals of biomedical engineering*, 38(3):1071–1097, 2010.

[19] Christopher JL Murray and Alan D Lopez. Mortality by cause for eight regions of the world: Global burden of disease study. *The Lancet*, 349(9061):1269–1276, 1997.

[20] William B Kannel, Philip A Wolf, Emelia J Benjamin, and Daniel Levy. Prevalence, incidence, prognosis, and predisposing conditions for atrial fibrillation: population-based estimates. *The American journal of cardiology*, 82(7):2N–9N, 1998.

[21] Jia Chen, Yubi Lin, Lifang Chen, Jian Yu, Zuoyi Du, Shushu Li, Zhenzhen Yang, Chuqian Zeng, Xiaoshu Lai, Qiji Lu, et al. A decade of complex fractionated electrograms catheter-based ablation for atrial fibrillation: Literature analysis, meta-analysis and systematic review. *IJC Heart & Vessels*, 4:63–72, 2014.

[22] A John Camm, Gregory YH Lip, Raffaele De Caterina, Irene Savelieva, Dan Atar, Stefan H Hohnloser, Gerhard Hindricks, Paulus Kirchhof, Jeroen J Bax, Helmut Baumgartner, et al. 2012 focused update of the esc guidelines for the management of atrial fibrillation. *European heart journal*, 33(21):2719–2747, 2012.

[23] Philip A Wolf, Robert D Abbott, and William B Kannel. Atrial fibrillation: a major contributor to stroke in the elderly: the framingham study. *Archives of internal medicine*, 147(9):1561–1564, 1987.

[24] Carmine Marini, Federica De Santis, Simona Sacco, Tommasina Russo, Luigi Olivieri, Rocco Totaro, and Antonio Carolei. Contribution of atrial fibrillation to incidence and outcome of ischemic stroke results from a population-based study. *Stroke*, 36(6):1115–1119, 2005.

[25] Stéphane Garrigue, Kent A Mowrey, Gerard Fahy, Patrick J Tchou, and Todor N Mazgalev. Atrioventricular nodal conduction during atrial fibrillation role of atrial input modification. *Circulation*, 99(17):2323–2333, 1999.

[26] Todor Mazgalev, Leonard S Dreifus, John Bianchi, and Eric L Michelson. Atrioventricular nodal conduction during atrial fibrillation in rabbit heart. *American Journal of Physiology-Heart and Circulatory Physiology*, 243(5):H754–H760, 1982.

[27] Emelia J Benjamin, Philip A Wolf, Ralph B D'Agostino, Halit Silbershatz, William B Kannel, and Daniel Levy. Impact of atrial fibrillation on the risk of death the framingham heart study. *Circulation*, 98(10):946–952, 1998.

[28] Donald M Lloyd-Jones, Thomas J Wang, Eric P Leip, Martin G Larson, Daniel Levy, Ramachandran S Vasan, Ralph B D'Agostino, Joseph M Massaro, Alexa Beiser, Philip A Wolf, et al. Lifetime risk for development of atrial fibrillation the framingham heart study. *Circulation*, 110(9):1042–1046, 2004.

[29] The Office of Health Economics. Estimating the direct costs of atrial fibrillation to the nhs in the constituent countries of the uk and at sha level in england, 2008. 2009.

[30] Niamh F Murphy, Colin R Simpson, Pardeep S Jhund, Simon Stewart, Michelle Kirkpatrick, Jim Chalmers, Kate MacIntyre, and John JV McMurray. A national

survey of the prevalence, incidence, primary care burden and treatment of atrial fibrillation in scotland. *Heart*, 93(5):606–612, 2007.

[31] Alan S Go, Elaine M Hylek, Kathleen A Phillips, YuChiao Chang, Lori E Henault, Joe V Selby, and Daniel E Singer. Prevalence of diagnosed atrial fibrillation in adults: national implications for rhythm management and stroke prevention: the anticoagulation and risk factors in atrial fibrillation (atria) study. *Jama*, 285(18):2370–2375, 2001.

[32] Valentin Fuster, Lars E Rydén, David S Cannom, Harry J Crijns, Anne B Curtis, Kenneth A Ellenbogen, Jonathan L Halperin, Jean-Yves Le Heuzey, G Neal Kay, James E Lowe, et al. Acc/aha/esc 2006 guidelines for the management of patients with atrial fibrillation: A report of the american college of cardiology/american heart association task force on practice guidelines and the european society of cardiology committee for practice guidelines (writing committee to revise the 2001 guidelines for the management of patients with atrial fibrillation) developed in collaboration with the european heart rhythm association and the heart rhythm society. *Journal of the American College of Cardiology*, 48(4):e149–e246, 2006.

[33] Paulus Kirchhof, Angelo Auricchio, Jeroen Bax, Harry Crijns, John Camm, Hans-Christoph Diener, Andreas Goette, Gerd Hindricks, Stefan Hohnloser, Lukas Kappenberger, et al. Outcome parameters for trials in atrial fibrillation. *Europace*, 2007.

[34] AF AWARE. Af aware cardiology groups call for greater awareness and better education on atrial fibrillation. press release 2009, 2011.

[35] Johan E.P. Waktare. Cardiology patient page atrial fibrillation. *Circulation*, 106:14–16, 2002.

[36] Stanley Nattel. New ideas about atrial fibrillation 50 years on. *Nature*, 415(6868):219–226, 2002.

[37] Caleb Ferguson, Sally C Inglis, Phillip J Newton, Sandy Middleton, Peter S Macdonald, and Patricia M Davidson. Atrial fibrillation: Stroke prevention in focus. *Australian Critical Care*, 27(2):92–98, 2014.

[38] David E Krummen, Gregory K Feld, and Sanjiv M Narayan. Diagnostic accuracy of irregularly irregular rr intervals in separating atrial fibrillation from atrial flutter. *The American journal of cardiology*, 98(2):209–214, 2006.

147

[39] Danina M Muntean, Zsófia Kohajda, Tamás Fazekas, and Norbert Jost. Atrial remodeling in permanent atrial fibrillation: Mechanisms and pharmacological implications. *Journal of Clinical and Experimental Cardiology*, 4(11):1, 2013.

[40] Michel Haissaguerre, Pierre Jaïs, Dipen C Shah, Atsushi Takahashi, Mélèze Hocini, Gilles Quiniou, Stéphane Garrigue, Alain Le Mouroux, Philippe Le Métayer, and Jacques Clémenty. Spontaneous initiation of atrial fibrillation by ectopic beats originating in the pulmonary veins. *New England Journal of Medicine*, 339(10):659–666, 1998.

[41] Shih-Ann Chen, Ming-Hsiung Hsieh, Ching-Tai Tai, Chin-Feng Tsai, VS Prakash, Wen-Chung Yu, Tsui-Lieh Hsu, Yu-An Ding, and Mau-Song Chang. Initiation of atrial fibrillation by ectopic beats originating from the pulmonary veins electrophysiological characteristics, pharmacological responses, and effects of radiofrequency ablation. *Circulation*, 100(18):1879–1886, 1999.

[42] Joachim R Ehrlich, Tae-Joon Cha, Liming Zhang, Denis Chartier, Peter Melnyk, Stefan H Hohnloser, and Stanley Nattel. Cellular electrophysiology of canine pulmonary vein cardiomyocytes: action potential and ionic current properties. *The Journal of physiology*, 551(3):801–813, 2003.

[43] Jose Jalife. Rotors and spiral waves in atrial fibrillation. *Journal of cardiovascular electrophysiology*, 14(7):776–780, 2003.

[44] Constanze Schmidt, Felix Wiedmann, Niels Voigt, Xiao-Bo Zhou, Jordi Heijman, Siegfried Lang, Virginia Albert, Stefan Kallenberger, Arjang Ruhparwar, Gábor Szabó, et al. Upregulation of k2p3. 1 k+ current causes action potential shortening in patients with chronic atrial fibrillation. *Circulation*, 114:88–98, 2015.

[45] Stanley Nattel, Ange Maguy, Sabrina Le Bouter, and Yung-Hsin Yeh. Arrhythmogenic ion-channel remodeling in the heart: heart failure, myocardial infarction, and atrial fibrillation. *Physiological reviews*, 87(2):425–456, 2007.

[46] Stanley Nattel, Brett Burstein, and Dobromir Dobrev. Atrial remodeling and atrial fibrillation mechanisms and implications. *Circulation: Arrhythmia and Electrophysiology*, 1(1):62–73, 2008.

[47] Oussama M Wazni, Nassir F Marrouche, David O Martin, Atul Verma, Mandeep Bhargava, Walid Saliba, Dianna Bash, Robert Schweikert, Johannes Brachmann, Jens Gunther, et al. Radiofrequency ablation vs antiarrhythmic drugs as

first-line treatment of symptomatic atrial fibrillation: a randomized trial. *Jama*, 293(21):2634–2640, 2005.

[48] James T Milnes, David J Madge, and John W Ford. New pharmacological approaches to atrial fibrillation. *Drug discovery today*, 17(13):654–659, 2012.

[49] Dobromir Dobrev, Leif Carlsson, and Stanley Nattel. Novel molecular targets for atrial fibrillation therapy. *Nature Reviews Drug Discovery*, 11(4):275–291, 2012.

[50] Peter Zimetbaum. Antiarrhythmic drug therapy for atrial fibrillation. *Circulation*, 125(2):381–389, 2012.

[51] Douglas P Zipes. Proarrhythmic effects of antiarrhythmic drugs. *The American journal of cardiology*, 59(11):26–31, 1987.

[52] Nick Freemantle, Carmelo Lafuente-Lafuente, Stephen Mitchell, Laurent Eckert, and Matthew Reynolds. Mixed treatment comparison of dronedarone, amiodarone, sotalol, flecainide, and propafenone, for the management of atrial fibrillation. *Europace*, 13(3):329–345, 2011.

[53] Hakan Oral, Bradley P Knight, Hiroshi Tada, Mehmet Özaydın, Aman Chugh, Sohail Hassan, Christoph Scharf, Steve WK Lai, Radmira Greenstein, Frank Pelosi, et al. Pulmonary vein isolation for paroxysmal and persistent atrial fibrillation. *Circulation*, 105(9):1077–1081, 2002.

[54] Navinder Sawhney, Ramtin Anousheh, Wei Chen, and Gregory K Feld. Circumferential pulmonary vein ablation with additional linear ablation results in an increased incidence of left atrial flutter compared with segmental pulmonary vein isolation as an initial approach to ablation of paroxysmal atrial fibrillation. *Circulation: Arrhythmia and Electrophysiology*, 3(3):243–248, 2010.

[55] Jürgen Vogt, Johannes Heintze, Klaus J Gutleben, Bogdan Muntean, Dieter Horstkotte, and Georg Nölker. Long-term outcomes after cryoballoon pulmonary vein isolation: results from a prospective study in 605 patients. *Journal of the American College of Cardiology*, 61(16):1707–1712, 2013.

[56] Sven Knecht, Christian Sticherling, Stefanie von Felten, David Conen, Beat Schaer, Peter Ammann, David Altmann, Stefan Osswald, and Michael Kühne. Long-term comparison of cryoballoon and radiofrequency ablation of paroxysmal atrial fibrillation: A propensity score matched analysis. *International journal of cardiology*, 176(3):645–650, 2014.

[57] Vivek Y Reddy, Christopher Houghtaling, Jay Fallon, Gwen Fischer, Norm Farr, Jamie Clarke, Jon Mcintyre, Ed Sinofsky, Jeremy N Ruskin, and David Keane. Use of a diode laser balloon ablation catheter to generate circumferential pulmonary venous lesions in an open-thoracotomy caprine model. *Pacing and clinical electrophysiology*, 27(1):52–57, 2004.

[58] Paul J Wang. Overview of balloon approaches to af ablation. *Journal of the American College of Cardiology*, 68(25):2758, 2016.

[59] Mélèze Hocini, Pierre Jaïs, Prashanthan Sanders, Yoshihide Takahashi, Martin Rotter, Thomas Rostock, Li-Fern Hsu, Frédéric Sacher, Sylvain Reuter, Jacques Clémenty, et al. Techniques, evaluation, and consequences of linear block at the left atrial roof in paroxysmal atrial fibrillation a prospective randomized study. *Circulation*, 112(24):3688–3696, 2005.

[60] Rakesh Latchamsetty and Fred Morady. Complex fractionated atrial electrograms a worthwhile target for ablation of atrial fibrillation? *Circulation: Arrhythmia and Electrophysiology*, 4(2):117–118, 2011.

[61] KHWJ Ten Tusscher and AV Panfilov. Influence of nonexcitable cells on spiral breakup in two-dimensional and three-dimensional excitable media. *Physical Review E*, 68(6):062902, 2003.

[62] Martin R Karch, Bernhard Zrenner, Isabel Deisenhofer, Jürgen Schreieck, Gjin Ndrepepa, Jun Dong, Katrin Lamprecht, Petra Barthel, Etienne Luciani, Albert Schömig, et al. Freedom from atrial tachyarrhythmias after catheter ablation of atrial fibrillation a randomized comparison between 2 current ablation strategies. *Circulation*, 111(22):2875–2880, 2005.

[63] Claude S Elayi, Atul Verma, Luigi Di Biase, Chi Keong Ching, Dimpi Patel, Conor Barrett, David Martin, Bai Rong, Tamer S Fahmy, Yaariv Khaykin, et al. Ablation for longstanding permanent atrial fibrillation: results from a randomized study comparing three different strategies. *Heart Rhythm*, 5(12):1658–1664, 2008.

[64] Wei-ju Li, Yong-yi Bai, Hong-yin Zhang, Ri-bo Tang, Cheng-long Miao, Cai-hua Sang, Xian-dong Yin, Jian-zeng Dong, and Chang-sheng Ma. Additional ablation of complex fractionated atrial electrograms after pulmonary vein isolation in patients with atrial fibrillation a meta-analysis. *Circulation: Arrhythmia and Electrophysiology*, 4(2):143–148, 2011.

[65] Koichiro Kumagai. Catheter ablation of atrial fibrillation-state of the art. *Circulation Journal*, 75(10):2305–2311, 2011.

[66] Ravi Ranjan, Ritsushi Kato, Menekhem M Zviman, Timm M Dickfeld, Ariel Roguin, Ronald D Berger, Gordon F Tomaselli, and Henry R Halperin. Gaps in the ablation line as a potential cause of recovery from electrical isolation and their visualization using mri. *Circulation: Arrhythmia and Electrophysiology*, 4(3):279–286, 2011.

[67] Dietmar Bänsch, Jenny Bittkau, Ralph Schneider, Cindy Schneider, Imke Wendig, Ibrahim Akin, and Christoph A Nienaber. Circumferential pulmonary vein isolation: wait or stop early after initial successful pulmonary vein isolation? *Europace*, 15(2):183–188, 2013.

[68] Stephan Zellerhoff, Matthew Daly, Han S Lim, Arnaud Denis, Yuki Komatsu, Laurence Jesel, Nicolas Derval, Frédéric Sacher, Hubert Cochet, Sébastien Knecht, et al. Pulmonary vein isolation using a circular, open irrigated mapping and ablation catheter (nmarq): a report on feasibility and efficacy. *Europace*, 16(9):1296–1303, 2014.

[69] Michel Haïssaguerre, Dipen C Shah, Pierre Jaïs, Mélèze Hocini, Teiichi Yamane, Isabel Deisenhofer, Michel Chauvin, Stéphane Garrigue, and Jacques Clémenty. Electrophysiological breakthroughs from the left atrium to the pulmonary veins. *Circulation*, 102(20):2463–2465, 2000.

[70] Koji Miyamoto, Takeshi Tsuchiya, Takanori Yamaguchi, Yasutsugu Nagamoto, Shin-ichi Ando, Kenji Sadamatsu, Yoshito Tanioka, and Naohiko Takahashi. A new method of a pulmonary vein map to identify a conduction gap on the pulmonary vein antrum ablation line. *Circ J*, 75(10):2363–71, 2011.

[71] Ivan M Robbins, Edward V Colvin, Thomas P Doyle, W Evans Kemp, James E Loyd, William S McMahon, and G Neal Kay. Pulmonary vein stenosis after catheter ablation of atrial fibrillation. *Circulation*, 98(17):1769–1775, 1998.

[72] Jeffrey E Saffitz, H Lee Kanter, Karen G Green, Timothy K Tolley, and Eric C Beyer. Tissue-specific determinants of anisotropic conduction velocity in canine atrial and ventricular myocardium. *Circulation Research*, 74(6):1065–1070, 1994.

[73] MH Draper and M Mya-Tu. A comparison of the conduction velocity in cardiac tissues of various mammals. *Quarterly journal of experimental physiology and cognate medical sciences*, 44(1):91–109, 1959.

[74] Takahiro Koura, Motoki Hara, Susumu Takeuchi, Kenichi Ota, Yasumasa Okada, Shunichiro Miyoshi, Atsushi Watanabe, Kazumi Shiraiwa, Hideo Mitamura, Itsuo Kodama, et al. Anisotropic conduction properties in canine atria analyzed by high-resolution optical mapping preferential direction of conduction block changes from longitudinal to transverse with increasing age. *Circulation*, 105(17):2092–2098, 2002.

[75] A Hansson, M Holm, P Blomström, R Johansson, Carsten Lührs, Johan Brandt, and SB Olsson. Right atrial free wall conduction velocity and degree of anisotropy in patients with stable sinus rhythm studied during open heart surgery. *European Heart Journal*, 19(2):293–300, 1998.

[76] Sanjay R Kharche, Irina V Biktasheva, Henggui Zhang, and Vadim N Biktashev. Simulating the role of anisotropy in human atrial cardioversion. In *2013 35th Annual International Conference of the IEEE Engineering in Medicine and Biology Society (EMBC)*, pages 6838–6841. IEEE, 2013.

[77] Frank M Weber, Armin Luik, Christopher Schilling, Gunnar Seemann, Martin W Krueger, Cristian Lorenz, Claus Schmitt, and Olaf Dossel. Conduction velocity restitution of the human atrium—an efficient measurement protocol for clinical electrophysiological studies. *IEEE Transactions on Biomedical Engineering*, 58(9):2648–2655, 2011.

[78] Flavio Fenton and Alain Karma. Vortex dynamics in three-dimensional continuous myocardium with fiber rotation: filament instability and fibrillation. *Chaos: An Interdisciplinary Journal of Nonlinear Science*, 8(1):20–47, 1998.

[79] Simon Labarthe, Jason Bayer, Yves Coudière, Jacques Henry, Hubert Cochet, Pierre Jaïs, and Edward Vigmond. A bilayer model of human atria: mathematical background, construction, and assessment. *Europace*, 16(suppl 4):iv21–iv29, 2014.

[80] Ali Gharaviri, Sander Verheule, Jens Eckstein, Mark Potse, Nico HL Kuijpers, and Ulrich Schotten. A computer model of endo-epicardial electrical dissociation and transmural conduction during atrial fibrillation. *Europace*, 14(suppl 5):v10–v16, 2012.

[81] Bram van Es, Barry Koren, and Hugo J de Blank. Finite-difference schemes for anisotropic diffusion. *Journal of Computational Physics*, 272:526–549, 2014.

[82] Arkady M Pertsov, Jorge M Davidenko, Remy Salomonsz, William T Baxter, and Jose Jalife. Spiral waves of excitation underlie reentrant activity in isolated cardiac muscle. *Circulation Research*, 72(3):631–650, 1993.

[83] Jacques Beaumont, Nicolas Davidenko, Jorge M Davidenko, and José Jalife. Spiral waves in two-dimensional models of ventricular muscle: formation of a stationary core. *Biophysical Journal*, 75(1):1–14, 1998.

[84] William H Sulis and Irina Nikolaevna Trofimova. *Nonlinear dynamics in the life and social sciences*, volume 320. IOS press, 2001.

[85] Carlos Vilas, Eva Balsa-Canto, Maria-Sonia G García, Julio R Banga, and Antonio A Alonso. Dynamic optimization of distributed biological systems using robust and efficient numerical techniques. *BMC systems biology*, 6(1):1, 2012.

[86] P Podziemski and JJ Żebrowski. Liénard-type models for the simulation of the action potential of cardiac nodal cells. *Physica D: Nonlinear Phenomena*, 261:52–61, 2013.

[87] Balth Van der Pol and Jan Van der Mark. Lxxii. the heartbeat considered as a relaxation oscillation, and an electrical model of the heart. *The London, Edinburgh, and Dublin Philosophical Magazine and Journal of Science*, 6(38):763–775, 1928.

[88] ML Cartwright. Forced oscillations in nonlinear systems. *Journal of Research of the National Bureau of Standards*, 45(6):514–518, 1950.

[89] T. Kanamaru. Van der Pol oscillator. *Scholarpedia*, 2(1):2202, 2007.

[90] Nina Byers and Gary Williams. *Out of the Shadows: Contributions of Twentieth-Century Women to Physics*. Cambridge University Press, 2006.

[91] Edward N Lorenz. Deterministic nonperiodic flow. *Journal of the atmospheric sciences*, 20(2):130–141, 1963.

[92] CR Katholi, F Urthaler, J Macy, and TN James. A mathematical model of automaticity in the sinus node and av junction based on weakly coupled relaxation oscillators. *Computers and Biomedical Research*, 10(6):529–543, 1977.

[93] Agnessa Babloyantz and Alain Destexhe. Is the normal heart a periodic oscillator? *Biological cybernetics*, 58(3):203–211, 1988.

[94] William M Lewis Jr. Phase locking, period-doubling bifurcations, and irregular dynamics in periodically stimulated cardiac cells. *Oecologia (Berlin)*, 19:75, 1975.

[95] Alan L Hodgkin and Andrew F Huxley. A quantitative description of membrane current and its application to conduction and excitation in nerve. *The Journal of physiology*, 117(4):500–544, 1952.

[96] Denis Noble, Alan Garny, and Penelope J Noble. How the hodgkin–huxley equations inspired the cardiac physiome project. *The Journal of physiology*, 590(11):2613–2628, 2012.

[97] Alexander V Panfilov and James P Keener. Re-entry in three-dimensional fitzhugh-nagumo medium with rotational anisotropy. *Physica D: Nonlinear Phenomena*, 84(3):545–552, 1995.

[98] Piotr Podziemski and Jan J Żebrowski. A simple model of the right atrium of the human heart with the sinoatrial and atrioventricular nodes included. *Journal of clinical monitoring and computing*, 27(4):481–498, 2013.

[99] H Zhang and AV Holden. Chaotic meander of spiral waves in the fitzhugh-nagumo system. *Chaos, Solitons & Fractals*, 5(3):661–670, 1995.

[100] Rubin R Aliev and Alexander V Panfilov. A simple two-variable model of cardiac excitation. *Chaos, Solitons & Fractals*, 7(3):293–301, 1996.

[101] KHWJ Ten Tusscher and Alexander V Panfilov. Reentry in heterogeneous cardiac tissue described by the luo-rudy ventricular action potential model. *American Journal of Physiology-Heart and Circulatory Physiology*, 284(2):H542–H548, 2003.

[102] Georg Duffing. *Erzwungene Schwingungen bei veränderlicher Eigenfrequenz und ihre technische Bedeutung.* Number 41-42. R, Vieweg & Sohn, 1918.

[103] JJ Żebrowski, K Grudziński, T Buchner, P Kuklik, J Gac, G Gielerak, P Sanders, and R Baranowski. Nonlinear oscillator model reproducing various phenomena in the dynamics of the conduction system of the heart. *Chaos: An Interdisciplinary Journal of Nonlinear Science*, 17(1):015121, 2007.

[104] Dmitry Postnov, Seung Kee Han, and Hyungtae Kook. Synchronization of diffusively coupled oscillators near the homoclinic bifurcation. *Physical Review E*, 60(3):2799, 1999.

[105] Catherine Morris and Harold Lecar. Voltage oscillations in the barnacle giant muscle fiber. *Biophysical journal*, 35(1):193–213, 1981.

[106] Yasutaka Kurata, Ichiro Hisatome, Sunao Imanishi, and Toshishige Shibamoto. Dynamical description of sinoatrial node pacemaking: improved mathematical model for primary pacemaker cell. *American Journal of Physiology-Heart and Circulatory Physiology*, 283(5):H2074–H2101, 2002.

[107] Nobuaki Sarai, Satoshi Matsuoka, Shinobu Kuratomi, Kyoichi Ono, and Akinori Noma. Role of individual ionic current systems in the sa node hypothesized by a model study. *The Japanese journal of physiology*, 53(2):125–134, 2003.

[108] RH Clayton and AV Panfilov. A guide to modelling cardiac electrical activity in anatomically detailed ventricles. *Progress in biophysics and molecular biology*, 96(1):19–43, 2008.

[109] A Rusakov, AB Medvinsky, and AV Panfilov. Scroll waves meandering in a model of an excitable medium. *Physical Review E*, 72(2):022902, 2005.

[110] AV Panfilov, Stefan C Müller, Vladimir S Zykov, and James P Keener. Elimination of spiral waves in cardiac tissue by multiple electrical shocks. *Physical Review E*, 61(4):4644, 2000.

[111] Hidetsugu Sakaguchi and Takefumi Fujimoto. Elimination of spiral chaos by periodic force for the aliev-panfilov model. *Physical Review E*, 67(6):067202, 2003.

[112] AV Panfilov. Spiral breakup in an array of coupled cells: the role of the intercellular conductance. *Physical review letters*, 88(11):118101, 2002.

[113] Denis Noble. A modification of the hodgkin—huxley equations applicable to purkinje fibre action and pacemaker potentials. *The Journal of Physiology*, 160(2):317–352, 1962.

[114] Ching-hsing Luo and Yoram Rudy. A dynamic model of the cardiac ventricular action potential. i. simulations of ionic currents and concentration changes. *Circulation research*, 74(6):1071–1096, 1994.

[115] K Yanagihara, A Noma, and H Irisawa. Reconstruction of sino-atrial node pacemaker potential based on the voltage clamp experiments. *The Japanese journal of physiology*, 30(6):841–857, 1979.

[116] D Noble and SJ Noble. A model of sino-atrial node electrical activity based on a modification of the difrancesco–noble (1984) equations. *Proceedings of the Royal Society of London B: Biological Sciences*, 222(1228):295–304, 1984.

[117] Victor A Maltsev and Edward G Lakatta. Synergism of coupled subsarcolemmal ca2+ clocks and sarcolemmal voltage clocks confers robust and flexible pacemaker function in a novel pacemaker cell model. *American Journal of Physiology-Heart and Circulatory Physiology*, 296(3):H594–H615, 2009.

[118] S Inada, JC Hancox, H Zhang, and MR Boyett. One-dimensional mathematical model of the atrioventricular node including atrio-nodal, nodal, and nodal-his cells. *Biophysical journal*, 97(8):2117–2127, 2009.

[119] Alfonso Bueno-Orovio, Elizabeth M Cherry, and Flavio H Fenton. Minimal model for human ventricular action potentials in tissue. *Journal of theoretical biology*, 253(3):544–560, 2008.

[120] Go W Beeler and H Reuter. Reconstruction of the action potential of ventricular myocardial fibres. *The Journal of physiology*, 268(1):177–210, 1977.

[121] Bernhard FAS Sakmann, Anthony J Spindler, Simon M Bryant, Klaus W Linz, and Denis Noble. Distribution of a persistent sodium current across the ventricular wall in guinea pigs. *Circulation Research*, 87(10):910–914, 2000.

[122] Satoshi Matsuoka, Nobuaki Sarai, Shinobu Kuratomi, Kyoichi Ono, and Akinori Noma. Role of individual ionic current systems in ventricular cells hypothesized by a model study. *The Japanese journal of physiology*, 53(2):105–123, 2003.

[123] Kirsten Hendrika Wilhelmina Johanna ten Tusscher. *Spiral wave dynamics and ventricular arrhythmias*. 2004.

[124] Anushka Michailova, Jeffrey Saucerman, Mary Ellen Belik, and Andrew D McCulloch. Modeling regulation of cardiac k atp and l-type ca 2+ currents by atp, adp, and mg 2+. *Biophysical journal*, 88(3):2234–2249, 2005.

[125] Kirsten HWJ ten Tusscher and Alexander V Panfilov. Alternans and spiral breakup in a human ventricular tissue model. *American Journal of Physiology-Heart and Circulatory Physiology*, 291(3):H1088–H1100, 2006.

[126] Leonid M Livshitz and Yoram Rudy. Regulation of ca2+ and electrical alternans in cardiac myocytes: role of camkii and repolarizing currents. *American Journal of Physiology-Heart and Circulatory Physiology*, 292(6):H2854–H2866, 2007.

[127] Aman Mahajan, Yohannes Shiferaw, Daisuke Sato, Ali Baher, Riccardo Olcese, Lai-Hua Xie, Ming-Jim Yang, Peng-Sheng Chen, Juan G Restrepo, Alain Karma, et al. A rabbit ventricular action potential model replicating cardiac dynamics at rapid heart rates. *Biophysical journal*, 94(2):392–410, 2008.

[128] Philip Stewart, Oleg V Aslanidi, Denis Noble, Penelope J Noble, Mark R Boyett, and Henggui Zhang. Mathematical models of the electrical action potential of

purkinje fibre cells. *Philosophical Transactions of the Royal Society of London A: Mathematical, Physical and Engineering Sciences*, 367(1896):2225–2255, 2009.

[129] DS Lindblad, CR Murphey, JW Clark, and WR Giles. A model of the action potential and underlying membrane currents in a rabbit atrial cell. *American Journal of Physiology*, 271:H1666–H1696, 1996.

[130] A Nygren, C Fiset, L Firek, JW Clark, DS Lindblad, RB Clark, and WR Giles. Mathematical model of an adult human atrial cell the role of k+ currents in repolarization. *Circulation Research*, 82(1):63–81, 1998.

[131] Catherine M Lloyd, James R Lawson, Peter J Hunter, and Poul F Nielsen. The cellml model repository. *Bioinformatics*, 24(18):2122–2123, 2008.

[132] Ching-Hsing Luo and Yoram Rudy. A dynamic model of the cardiac ventricular action potential. ii. afterdepolarizations, triggered activity, and potentiation. *Circulation Research*, 74(6):1097–1113, 1994.

[133] Denis Noble and Yoram Rudy. Models of cardiac ventricular action potentials: iterative interaction between experiment and simulation. *Philosophical Transactions of the Royal Society of London A: Mathematical, Physical and Engineering Sciences*, 359(1783):1127–1142, 2001.

[134] Robert Dumaine, Jeffrey A Towbin, Pedro Brugada, Matteo Vatta, Dmitri V Nesterenko, Vladislav V Nesterenko, Josep Brugada, Ramon Brugada, and Charles Antzelevitch. Ionic mechanisms responsible for the electrocardiographic phenotype of the brugada syndrome are temperature dependent. *Circulation research*, 85(9):803–809, 1999.

[135] KHWJ Ten Tusscher, D Noble, PJ Noble, and AV Panfilov. A model for human ventricular tissue. *American Journal of Physiology-Heart and Circulatory Physiology*, 286(4):H1573–H1589, 2004.

[136] Steven Niederer, Lawrence Mitchell, Nicolas Smith, and Gernot Plank. Simulating human cardiac electrophysiology on clinical time-scales. *Front Physiol*, 2:14, 2011.

[137] Venkata Krishna Nimmagadda, Ali Akoglu, Salim Hariri, and Talal Moukabary. Cardiac simulation on multi-gpu platform. *The Journal of Supercomputing*, 59(3):1360–1378, 2012.

[138] JUN-ICHI OKADA, Teruyoshi Sasaki, Takumi Washio, Hiroshi Yamashita, Taro Kariya, Yasushi Imai, Machiko Nakagawa, Yoshimasa Kadooka, Ryozo Nagai,

Toshiaki Hisada, et al. Patient specific simulation of body surface ecg using the finite element method. *Pacing and Clinical Electrophysiology*, 36(3):309–321, 2013.

[139] Kristopher M Kahlig, Sunita N Misra, and Alfred L George. Impaired inactivation gate stabilization predicts increased persistent current for an epilepsy-associated scn1a mutation. *The Journal of neuroscience*, 26(43):10958–10966, 2006.

[140] M. Fink and D. Noble. Noble model. *Scholarpedia*, 3(2):1803, 2008.

[141] Freeman Dyson. A meeting with enrico fermi. *Nature*, 427(6972):297–297, 2004.

[142] Jürgen Mayer, Khaled Khairy, and Jonathon Howard. Drawing an elephant with four complex parameters. *American Journal of Physics*, 78(6):648–649, 2010.

[143] SA Niederer, M Fink, D Noble, and NP Smith. A meta-analysis of cardiac electrophysiology computational models. *Experimental physiology*, 94(5):486–495, 2009.

[144] Flavio H Fenton, Elizabeth M Cherry, Harold M Hastings, and Steven J Evans. Multiple mechanisms of spiral wave breakup in a model of cardiac electrical activity. *Chaos: An Interdisciplinary Journal of Nonlinear Science*, 12(3):852–892, 2002.

[145] Wouter-Jan Rappel, Flavio Fenton, and Alain Karma. Spatiotemporal control of wave instabilities in cardiac tissue. *Physical review letters*, 83(2):456, 1999.

[146] Jatin Relan, Maxime Sermesant, Hervé Delingette, Mihaela Pop, Graham A Wright, and Nicholas Ayache. Quantitative comparison of two cardiac electrophysiology models using personalisation to optical and mr data. In *Biomedical Imaging: From Nano to Macro, 2009. ISBI'09. IEEE International Symposium on*, pages 1027–1030. IEEE, 2009.

[147] Muriel Boulakia, Miguel A Fernández, Jean-Frédéric Gerbeau, and Nejib Zemzemi. Towards the numerical simulation of electrocardiograms. In *Functional Imaging and Modeling of the Heart*, pages 240–249. Springer, 2007.

[148] Gary R Mirams, Mark R Davies, Yi Cui, Peter Kohl, and Denis Noble. Application of cardiac electrophysiology simulations to pro-arrhythmic safety testing. *British journal of pharmacology*, 167(5):932–945, 2012.

[149] Leo Priebe and Dirk J Beuckelmann. Simulation study of cellular electric properties in heart failure. *Circulation research*, 82(11):1206–1223, 1998.

[150] Vivek Iyer, Reza Mazhari, and Raimond L Winslow. A computational model of the human left-ventricular epicardial myocyte. *Biophysical journal*, 87(3):1507–1525, 2004.

[151] Ezio Bartocci, Elizabeth M Cherry, James Glimm, Radu Grosu, Scott A Smolka, and Flavio H Fenton. Toward real-time simulation of cardiac dynamics. In *Proceedings of the 9th International Conference on Computational Methods in Systems Biology*, pages 103–112. ACM, 2011.

[152] Flavio H Fenton and Elizabeth M Cherry. Models of cardiac cell. *Scholarpedia*, 3(8):1868, 2008.

[153] Simon Labarthe. *Modélisation de l'activité électrique des oreillettes et des veines pulmonaires*. PhD thesis, Université Victor Segalen-Bordeaux II, 2013.

[154] John A Nelder and Roger Mead. A simplex method for function minimization. *The computer journal*, 7(4):308–313, 1965.

[155] Russ C Eberhart, James Kennedy, et al. A new optimizer using particle swarm theory. In *Proceedings of the sixth international symposium on micro machine and human science*, volume 1, pages 39–43. New York, NY, 1995.

[156] Yuhui Shi and Russell C Eberhart. Empirical study of particle swarm optimization. In *Evolutionary Computation, 1999. CEC 99. Proceedings of the 1999 Congress on*, volume 3. IEEE, 1999.

[157] Fawang Liu, John Walmsley, and Kevin Burrage. Parameter estimation for a phenomenological model of the cardiac action potential. *ANZIAM Journal*, 52:482–499, 2011.

[158] Kalyanmoy Deb, Amrit Pratap, Sameer Agarwal, and TAMT Meyarivan. A fast and elitist multiobjective genetic algorithm: Nsga-ii. *IEEE transactions on evolutionary computation*, 6(2):182–197, 2002.

[159] Eleftherios Avramidis and Ozgur E Akman. Optimisation of an exemplar oculomotor model using multi-objective genetic algorithms executed on a gpu-cpu combination. *BMC systems biology*, 11(1):40, 2017.

[160] Jaemin Shim, Boyoung Joung, Jae Hyung Park, Jae-Sun Uhm, Moon-Hyoung Lee, and Hui-Nam Pak. Long duration of radiofrequency energy delivery is an independent predictor of clinical recurrence after catheter ablation of atrial fibrillation: over 500 cases experience. *International journal of cardiology*, 167(6):2667–2672, 2013.

[161] Kathleen S McDowell, Fijoy Vadakkumpadan, Robert Blake, Joshua Blauer, Gernot Plank, Rob S MacLeod, and Natalia A Trayanova. Mechanistic inquiry into the

role of tissue remodeling in fibrotic lesions in human atrial fibrillation. *Biophysical journal*, 104(12):2764–2773, 2013.

[162] Sohail Zahid, Hubert Cochet, Patrick M Boyle, Erica L Schwarz, Kaitlyn N Whyte, Edward J Vigmond, Rémi Dubois, Mélèze Hocini, Michel Haïssaguerre, Pierre Jaïs, et al. Patient-derived models link re-entrant driver localization in atrial fibrillation to fibrosis spatial pattern. *Cardiovascular research*, 110(3):443–454, 2016.

[163] Kathleen S McDowell, Fijoy Vadakkumpadan, Robert Blake, Joshua Blauer, Gernot Plank, Rob S MacLeod, and Natalia A Trayanova. Methodology for patient-specific modeling of atrial fibrosis as a substrate for atrial fibrillation. *Journal of electrocardiology*, 45(6):640–645, 2012.

[164] Jonathan Chrispin, Esra Gucuk Ipek, Sohail Zahid, Adityo Prakosa, Mohammadali Habibi, David Spragg, Joseph E Marine, Hiroshi Ashikaga, John Rickard, Natalia A Trayanova, et al. Lack of regional association between atrial late gadolinium enhancement on cardiac magnetic resonance and atrial fibrillation rotors. *Heart Rhythm*, 13(3):654–660, 2016.

[165] L Dang, N Virag, Z Ihara, V Jacquemet, J-M Vesin, J Schlaepfer, P Ruchat, and L Kappenberger. Evaluation of ablation patterns using a biophysical model of atrial fibrillation. *Annals of biomedical engineering*, 33(4):465–474, 2005.

[166] Matthias Reumann, Julia Bohnert, Gunnar Seemann, Brigitte Osswald, and Olaf Dössel. Preventive ablation strategies in a biophysical model of atrial fibrillation based on realistic anatomical data. *Biomedical Engineering, IEEE Transactions on*, 55(2):399–406, 2008.

[167] C Tobon, C Ruiz, JF Rodriguez, F Hornero, JM Ferrero Jr, and J Saiz. Vulnerability for reentry in a three dimensional model of human atria: a simulation study. In *Engineering in Medicine and Biology Society (EMBC), 2010 Annual International Conference of the IEEE*, pages 224–227. IEEE, 2010.

[168] Yonghyeon Yun, Minki Hwang, Jae Hyung Park, Hangsik Shin, Eun Bo Shim, and Hui-Nam Pak. The relationship among complex fractionated electrograms, wavebreak, phase singularity, and local dominant frequency in fibrillation wave-dynamics: a modeling comparison study. *Journal of Korean medical science*, 29(3):370–377, 2014.

[169] Riski Imaniastuti, Hyun Seung Lee, Nari Kim, Jae Boum Youm, Eun Bo Shim, and Ki Moo Lim. Computational prediction of proarrhythmogenic effect of the v241f

kcnq1 mutation in human atrium. *Progress in biophysics and molecular biology*, 116(1):70–75, 2014.

[170] Fei Xie and Christian W Zemlin. Effect of twisted fiber anisotropy in cardiac tissue on ablation with pulsed electric fields. *PloS one*, 11(4):e0152262, 2016.

[171] Jadranka Stojanovska and Paul Cronin. Computed tomography imaging of left atrium and pulmonary veins for radiofrequency ablation of atrial fibrillation. In *Seminars in roentgenology*, volume 43, pages 154–166. Elsevier, 2008.

[172] Paul Cronin, Aine Marie Kelly, Benoit Desjardins, Smita Patel, Barry H Gross, Ella A Kazerooni, Fred Morady, Hakan Oral, and Ruth C Carlos. Normative analysis of pulmonary vein drainage patterns on multidetector ct with measurements of pulmonary vein ostial diameter and distance to first bifurcation. *Academic radiology*, 14(2):178–188, 2007.

[173] José Angel Cabrera, Damián Sánchez-Quintana, Jerónimo Farré, Felipe Navarro, José Manuel Rubio, Fernando Cabestrero, Robert H Anderson, and Siew Yen Ho. Ultrasonic characterization of the pulmonary venous wall echographic and histological correlation. *Circulation*, 106(8):968–973, 2002.

[174] Yun-Hyeon Kim, Edith M Marom, James E Herndon, and H Page McAdams. Pulmonary vein diameter, cross-sectional area, and shape: Ct analysis 1. *Radiology*, 235(1):43–49, 2005.

[175] Enrique J Berjano. Theoretical modeling for radiofrequency ablation: state-of-the-art and challenges for the future. *Biomedical engineering online*, 5(1):24, 2006.

[176] Ana González Suárez, Fernando Hornero, and Enrique J Berjano. Mathematical modeling of epicardial rf ablation of atrial tissue with overlying epicardial fat. *The open biomedical engineering journal*, 4(1), 2010.

[177] Kazutaka Gima and Yoram Rudy. Ionic current basis of electrocardiographic waveforms a model study. *Circulation Research*, 90(8):889–896, 2002.

[178] Saagar Mahida, Frederic Sacher, Nicolas Derval, Benjamin Berte, Seigo Yamashita, Darren Hooks, Arnaud Denis, Sana Amraoui, Meleze Hocini, Michel Haissaguerre, et al. Science linking pulmonary veins and atrial fibrillation. *Arrhythmia & electrophysiology review*, 4(1):40, 2015.

[179] Edsger W Dijkstra. A note on two problems in connexion with graphs. *Numerische mathematik*, 1(1):269–271, 1959.

[180] Mikael Wallman, Nicolas P Smith, and Blanca Rodriguez. A comparative study of graph-based, eikonal, and monodomain simulations for the estimation of cardiac activation times. *IEEE Transactions on Biomedical Engineering*, 59(6):1739–1748, 2012.

[181] Peter E Hart, Nils J Nilsson, and Bertram Raphael. A formal basis for the heuristic determination of minimum cost paths. *IEEE transactions on Systems Science and Cybernetics*, 4(2):100–107, 1968.

[182] Frank M Weber, Christopher Schilling, Gunnar Seemann, Armin Luik, Claus Schmitt, Cristian Lorenz, and Olaf Dossel. Wave-direction and conduction-velocity analysis from intracardiac electrograms–a single-shot technique. *IEEE transactions on biomedical engineering*, 57(10):2394–2401, 2010.

[183] Markus Lang, Haitao Guo, Jan E Odegard, C Sidney Burrus, and Raymond O Wells. Noise reduction using an undecimated discrete wavelet transform. *IEEE Signal Processing Letters*, 3(1):10–12, 1996.

[184] Gerald Kaiser. *A friendly guide to wavelets*. Springer Science & Business Media, 2010.

[185] Ingrid Daubechies. Orthonormal bases of compactly supported wavelets. *Communications on pure and applied mathematics*, 41(7):909–996, 1988.

[186] C Sidney Burrus, Ramesh A Gopinath, and Haitao Guo. Introduction to wavelets and wavelet transforms: a primer. 1997.

[187] EGT Swee and S Elangovan. Applications of symlets for denoising and load forecasting. In *Higher-Order Statistics, 1999. Proceedings of the IEEE Signal Processing Workshop on*, pages 165–169. IEEE, 1999.

[188] Mahesh S Chavan, Nikos Mastorakis, Manjusha N Chavan, MS Gaikwad, et al. Implementation of symlet wavelets to removal of gaussian additive noise from speech signal. In *Proceedings of Recent Researches in Communications, Automation, Signal Processing, Nanotechnology, Astronomy and Nuclear Physics: 10th WSEAS International Conference on Electronics, Hardware, Wireless and Optical Communications (EHAC'11), Cambridge*, page 37, 2011.

[189] Akshay Sharma, Gyanendra Sheoran, ZA Jaffery, et al. Improvement of signal-to-noise ratio in digital holography using wavelet transform. *Optics and lasers in engineering*, 46(1):42–47, 2008.

[190] James F Kaiser. On a simple algorithm to calculate the'energy'of a signal. In *Acoustics, Speech, and Signal Processing, 1990. ICASSP-90., 1990 International Conference on*, pages 381–384. IEEE, 1990.

[191] Rajeev Agarwal and Jean Gotman. Adaptive segmentation of electroencephalographic data using a nonlinear energy operator. In *Circuits and Systems, 1999. ISCAS'99. Proceedings of the 1999 IEEE International Symposium on*, volume 4, pages 199–202. IEEE, 1999.

[192] C Schilling, MP Nguyen, A Luik, C Schmitt, and O Dössel. Non-linear energy operator for the analysis of intracardial electrograms. In *World Congress on Medical Physics and Biomedical Engineering, September 7-12, 2009, Munich, Germany*, pages 872–875. Springer, 2009.

[193] MP Nguyen, C Schilling, and O Dössel. A new approach for automated location of active segments in intracardiac electrograms. In *World Congress on Medical Physics and Biomedical Engineering, September 7-12, 2009, Munich, Germany*, pages 763–766. Springer, 2010.

[194] Fredric J Harris. On the use of windows for harmonic analysis with the discrete fourier transform. *Proceedings of the IEEE*, 66(1):51–83, 1978.

[195] J. Terry and H. Green. Detection of conduction gaps in a pulmonary vein, May 11 2017. WO Patent App. PCT/GB2016/053,421.

[196] Sitabhra Sinha and S Sridhar. *Patterns in Excitable Media*. CRC Press, 2015.